Measurement of the cross section for associated production of a W boson and two b quarks with the CMS detector at the Large Hadron Collider

Luetić, Jelena

University of Zagreb

FACULTY OF SCIENCE

Jelena Luetić

Measurement of the cross section for associated production of a W boson and two b quarks with the CMS detector at the Large Hadron Collider

DOCTORAL THESIS

Zagreb, 2015.

University of Zagreb

FACULTY OF SCIENCE

Jelena Luetić

Measurement of the cross section for associated production of a W boson and two b quarks with the CMS detector at the Large Hadron Collider

DOCTORAL THESIS

Supervisor:

Professor Vuko Brigljević, PhD

Zagreb, 2015

Sveučilište u Zagrebu

PRIRODOSLOVNO MATEMATIČKI FAKULTET

Jelena Luetić

Mjerenje udarnog presjeka zajedničke tvorbe W bozona i para b kvarkova detektorom CMS na Velikom hadronskom sudarivaču

DOKTORSKI RAD

Mentor:

Prof. dr. sc. Vuko Brigljević

Zagreb, 2015.

Doktorski rad izrađen je na Sveučilištu u Zagrebu, Prirodoslovno-matematičkom fakultetu

Mentor: prof. dr. sc. Vuko Brigljević

Doktorski rad ima: 130 stranica

Doktorski rad br.: ______

*"Each time new experiments are observed to agree with the predictions, the theory survives and our confidence in it is increased; but if ever a new observation is found to disagree, we have to abandon or modify the theory.
At least that is what it is supposed to happen, but you can always question the competence of the person who carried out the observation."*

Stephan Hawking

Abstract

The goal of this thesis is a measurement of the cross section of the $pp \rightarrow W + bb + X$ process using the data collected during 2012 at $\sqrt{s} = 8$ TeV. The data is provided by the Large Hadron Collider (LHC) accelerator at CERN, Geneva and collected by the Compact Muon Solenoid (CMS). The production of a W boson in association with a pair of b quarks (Wbb) in proton collisions has been the topic of many theoretical calculations and simulations. It is however still not well described due to divergences which arise in theoretical calculations, in cases where b quarks are collinear or there is a low energy massless particle irradiated. A precise measurement of Wbb production will allow to further constrain theoretical predictions in the framework of perturbative quantum chromodynamics (pQCD). On the other hand, Wbb is a background in the measurements of different standard model processes as well as in several searches for physics beyond standard model.

The presence of a W boson is identified through the detection of an energetic, isolated lepton (muon or electron) and a significant amount of missing energy, which indicates the presence of a neutrino. Jets in the detector are identified as collimated sprays of particles. Selected jets are required to be tagged as jets originating from b quarks.

The cross section measurement was performed in the fiducial region defined by a presence of a lepton and exactly two 2 b-tagged jets. The result is quoted separately in the muon and electron channel. The measured values in the two channels are compatible, as predicted by the standard model. The theoretical cross section was derived using MCFM. The measured values are around one standard deviation higher than the predicted theoretical values. The uncertainty on the measured values is dominated by the systematic effects. The largest uncertainties are associated with the b tagging procedure, jet energy scale and jet energy resolution. Reducing these uncertainties in the future, would allow for more sensitive test of perturbative QCD calculation at next-to-leading order.

Keywords: LHC, CMS, Standard model, Wbb, cross section

Acknowledgements

I would like to thank all the people who helped make this thesis see the light of day. Thanks to the colegues from University of Wisconsin-Madison, University of Trieste and CERN, specially to Tom , Andrea and others for all their effort and help during past year. Big thanks to Michele for his guidance, patience and precious comments.

I would like to thank to all the CMS group from Ruđer Bošković Institute. Thanks to Lucija for being a good friend and listener when I needed one. Thanks to Tanja for all her help and hard work and fruitful discussions, without you this would be nearly half as fun. Thanks to Srećko, Senka, Darko, Saša and Benjamin for all the help and interesting discussions over the past few years. Special thanks to my supervisor Vuko Brigljević for helping me and believing in me over the past few years.

Thanks to the Pixel group, specially to Danek, Viktor, Gino, Janos, Urs, Annapaola and others for giving me a chance to work on something new and exciting.

Special thanks to my family for all their support and patience. Without you none of this would be possible.

Goran, thank you for being there for me and making me happy.

Contents

List of Figures

List of Tables

Abbreviations

SM	Standard Model
CERN	European Organization for Nuclear Research
LHC	Large Hadron Collider
CMS	Compact Muon Solenoid
CP	Charge-parity
CKM	Cabibbo-Kobayashi-Maskawa matrix
QCD	Quantum chromodynamics
LO	Leading order
NLO	Next-to-leading order
DPS	Double Parton Scattering
ECAL	Electromagnetic Calorimeter
HCAL	Hadronic Calorimeter
CSC	Cathode Strip Chamber
RPC	Resistive Plate Chambers
DT	Drift Tubes
L1	Level 1 Trigger
HLT	High Level Trigger
PF	Particle Flow
GSF	Gaussian Sum Filter
CSV	Combined Secondary Vertex

Chapter 1

Introduction

The standard model of particle physics tries to give an answer to the questions what is matter made of and how does it interact. The predictions of the standard model have been thoroughly tested through various precision measurements at different experiments. Every time the standard model predictions were confirmed. The only missing link, the long sought Higgs boson, was found in 2012, and its properties were measured in the following years, thus completing the picture of elementary particles. However, the standard model still leaves some unexplained phenomena, e.g. neutrino oscillations, matter-antimatter asymmetry, the existence of dark matter and dark energy, motivating the searches for physics beyond standard model. The sensitivity to such processes in high energy physics experiments strongly depends on the precise measurements of known processes. In such measurements, poorly known yields and kinematics of known processes would lead to high uncertainties, and thus reducing the sensitivity of the experiment.

The production of a W boson in association with a pair of b quarks (Wbb) in proton collisions has been the topic of many theoretical calculations and simulations. It is however still not well described due to divergences which arise in theoretical calculations, in cases where b quarks are collinear or there is a low energy massless particle irradiated. Several theoretical approaches, implemented in different simulation packages, have been used to describe the Wbb production mechanism. A precise measurement of Wbb production will allow to further constrain theoretical predictions in the framework of perturbative quantum chromodynamics (pQCD) and to test the validity of different theoretical models used in simulations. On the other hand, Wbb is a background in the measurements of different standard model processes as well as in several searches for physics beyond standard model. It is one of the main backgrounds in top quark and Higgs boson measurements. When Higgs boson is produced in association with a W boson and decays to a pair of b quarks, this shows the same signature in the detector as the Wbb.

The goal of this thesis is a measurement of the cross section of the $pp \to W + bb + X$ process using the data collected during 2012 at $\sqrt{s} = 8$ TeV. The data is provided by the Large Hadron Collider (LHC) accelerator at CERN, Geneva and collected by the Compact Muon Solenoid (CMS). W boson used in the analysis is decaying either to an electron or muon, and a corresponding neutrino. The presence of a W boson is identified through the detection of an energetic, isolated lepton, i.e. a lepton with low additional activity in some predefined cone around it, and a significant amount of missing energy, which indicates the presence of a neutrino. Jets in the detector are identified as collimated sprays of particles. Selected jets are required to be tagged as jets originating from b quarks. This procedure is called b-tagging and it exploits the unique properties of b quark to derive a single discriminator value to distinguish between b jets and jets from lighter quarks, or gluons.

The thesis is organized as follows. Chapter 2 gives a brief introduction to the standard model, including the discovery and the role of W boson and b quarks within the standard model. An overview of the phenomenology of proton collisions at hadron colliders is shown. All the steps for the theoretical calculation of the $pp \to W + bb + X$ process are given for both, single parton scattering and double parton scattering production mechanisms. The end of the chapter summarizes all previous measurements of W boson and b quarks in the final state. Chapters 3 and 4 are focused on the description of the LHC and the CMS respectively. All CMS subsystems are described and their role is explained. Chapter 5 describes the procedure for the reconstruction of various physics objects, including electrons, muons and jets, and the estimation of missing energy. Chapter 6 lists all data and Monte Carlo samples used. The criteria for the signal selection are described and all major backgrounds are identified. Chapter 7 describes all steps in the cross section determination, including the fitting procedure used to extract the final yields, and the acceptance and efficiency estimation. In the end, the results are presented, together with the comparison to theoretical predictions. Chapter 8 briefly summarizes the results, and shows the prospects for the future research on this topic.

Chapter 2

Theoretical overview and previous measurements

The standard model (SM) of elementary particles is a theory which emerged in the 1960s and 1970s, which describes all of the known elementary particles and interactions except gravity. The final formulation of the SM incorporates several theories: quantum electrodynamics, Glashow-Weinberg-Salam theory of electroweak processes and quantum chromodynamics. The first steps towards a formulation of SM occurred in 1961. when Sheldon Glashow unified electromagnetic and weak interactions [1]. The difference in strength between the weak and electromagnetic forces was puzzling for physicists at that time, and Glashow proposed that it can be accounted for if the weak force were mediated by massive bosons. However, he was not able to explain the origin of the mass for such mediators. The explanation came in 1967 when Steven Weinberg and Abdul Salam used the Higgs mechanism in the electroweak theory [2, 3], which suggested the existence of an additional particle called Higgs boson. After the discovery of neutral currents, which arise from the exchange of the neutral Z boson, the electroweak theory became generally accepted. The W and Z bosons were discovered in 1983 at CERN [4, 5], and their masses were in agreement with the SM prediction. The theory describing strong interactions got its final form in 1974 when it was shown that hadrons consist of quarks. The final missing link in the SM, the Higgs boson, was discovered in 2012 at CERN [6, 7]. However, there are several unexplained phenomena which suggest the existence of physics beyond SM, but so far its predictions were confirmed every time through numerous experimental tests. In this chapter a brief overview of the SM particles and interactions will be shown with the emphasis on the W boson and b quarks, which are the most relevant for this thesis. An introduction to cross section determination at hadron colliders is given. In the last part of the chapter an historical overview of the development of W+b-jets theoretical calculations is described together with the existing experimental results.

2.1 Standard model overview

Elementary particle physics is described within the framework of the SM. We usually imagine particles as point like objects which are subject to some forces between them. These particles are fermions, leptons or quarks of spin $s = 1/2$. There are three charged leptons, electron, muon and tau whose properties are the same except for their mass. Each of the leptons has a corresponding neutrally charged neutrino with a very small mass. There are six different types of quarks with charge either $Q = 2/3$ of $Q = -1/3$ as seen in figure 2.1. They also carry one additional quantum number, which is color charge. All objects observed in nature are colorless giving rise to the concept of quark confinement, which will be explained later. Colorless composite objects are classified into two categories. Baryons are fermions made out of three quarks, protons and neutrons. The other category is composed of mesons, which are made of quark and antiquark, like pions. Quarks are divided into three generations with all identical properties except for the masses of the particles.

The SM is based on a gauge symmetry $SU(3)_C \times SU(2)_L \times U(1)_Y$. Strong interaction symmetries are described by $SU(3)_C$ group, while the electroweak sector is described by $SU(2)_L \times U(1)_Y$. All interactions within the SM are mediated by elementary particles which are a spin 1 bosons. In the case of electromagnetic interactions, the mediator is a massless photon. Thus the range of electromagnetic interaction is infinite. For the weak force the mediators are the three massive bosons $W^{\pm}$ and Z and its range is very small (10^{-16} m). These four bosons are the gauge bosons of the $SU(2)_L \times U(1)_Y$ group. The interaction between electroweak bosons is allowed in the SM as long as charge conservation principle remains valid. The strong force is mediated by the exchange of 8 massless gauge bosons for $SU(3)_C$ called gluons. Although gluons are massless, the range of the strong force is not infinite. Due to the effect of confinement, the range of the strong force is approximately the size of the lightest hadrons ($10^{-13}cm$).

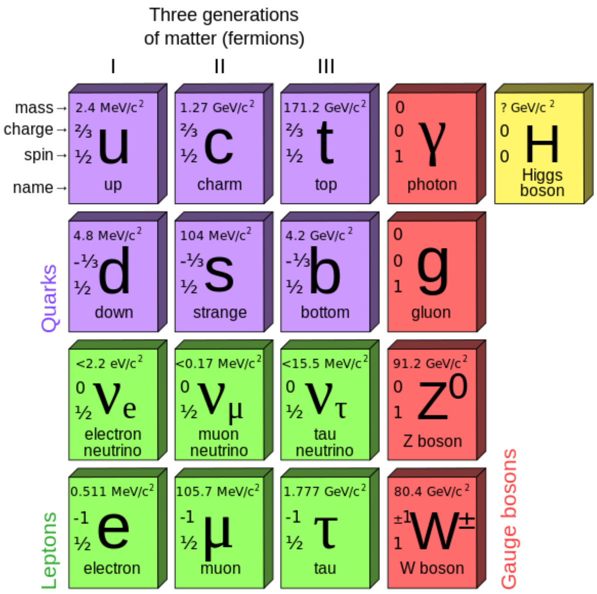

FIGURE 2.1: List of the SM elementary particles.

The fact that weak gauge bosons are massive indicates that $SU(2)_L \times U(1)_Y$ is not a good symmetry of the vacuum. Photons, on the other hand, are massless, $U(1)_{em}$ is thus a good symmetry of the vacuum. This means that the $SU(2)_L \times U(1)_Y$ electroweak symmetry is somehow spontaneously broken to $U(1)_{em}$ of electromagnetism. Spontaneous symmetry breaking is implemented through the Higgs mechanism, which gives masses to fermions, $W^{\pm}$ and Z boson and leaves the photon massless. Details of the mechanism can be found elsewhere, e.g. [8] but the main point is that it also predicts a new scalar and electrically neutral particle which is called Higgs boson. The search for the Higgs boson lasted few decades before finally in 2012, a new particle was discovered with a mass of 125

GeV [6, 7]. In the last three years, properties of this new particle have been measured. At this point, all measurements agree within the experimental and theoretical uncertainties with SM predictions for the Higgs boson.

2.1.1 The bottom quark

The history of the bottom quark begins in 1973, when Makoto Kobayashi and Toshihide Maskawa first introduced the third generation of quarks to explain the charge-parity (CP) violation observed in neutral K mesons [9]. CP violation is introduced as a small phase factor δ in the Cabibbo-Kobayashi-Maskawa (CKM) matrix provided there are at least three generations of quarks. This prediction was done even before the discovery of c quark. Kobayashi and Maskawa received the 2008 Nobel Prize in Physics for their explanation of CP-violation after several experiments confirmed that the predicted behavior is not exclusive for K mesons, but can be seen also in B mesons [10, 11].

The name "bottom" was introduced in 1975 by Haim Harari. The bottom quark was discovered in 1977 by the Fermilab E288 experiment team led by Leon M. Lederman through the observation of the Υ resonance, which is formed from a bottom quark and its antiparticle [12].

At the LHC, the main production mechanism for b quarks is through strong interaction (any diagram involving $g \to bb$). Other important contribution for this analysis is also from top quark decay ($t \to Wb$). Every b quark, after production, goes through the process of hadronization, forming one of the color neutral B hadrons. Excited B hadrons decay strongly or electromagnetically, while ground state B hadrons decay weakly, resulting in relatively long lifetime of ~1.5 ps. Bottom quark can decay either to c quark or u quark. Both of these decays are suppressed by the CKM matrix 2.1.

$$\begin{pmatrix} V_{ud} & V_{us} & V_{ub} \\ V_{cd} & V_{cs} & V_{cb} \\ V_{td} & V_{ts} & V_{tb} \end{pmatrix} = \begin{pmatrix} 0.974 & 0.225 & 0.003 \\ 0.225 & 0.973 & 0.041 \\ 0.009 & 0.040 & 0.999 \end{pmatrix} \tag{2.1}$$

B mesons traverse a substantial distance inside the detector before decaying due to their long lifetime. The displacement of the decay vertex is of the order of few millimetres, which is well above the precision of CMS Pixel detector. This fact is used in the creation of various b-tagging algorithms which are taking into account tracks originating from displaced vertices, discussed in Section 5.4.4.

2.1.2 W boson

The W boson is one of the massive mediators of the weak interaction. It has with a mass of $m_W = 80.1$ GeV. The discovery of W and Z bosons in proton-antiproton collisions at UA1 and UA2 experiments was one of the major successes of the CERN experimental facility. The Super Proton Synchrotron was the first accelerator powerful enough to produce W and Z bosons. Both collaborations reported their findings in 1983 [13, 14]. The W boson at the LHC is primarily produced through quark-antiquark annihilation. In the majority of the cases, the W boson decays to quark-antiquark pair (66% of all W boson decays). Other decay channels include creation of a lepton and its corresponding neutrino ($\sim 10\%$ per lepton generation). This decay channel was the most important for the W boson discovery and it is still essential for W boson detection at hadron colliders despite the large hadronic backgrounds because it includes easily identifiable isolated lepton and significant missing energy.

The detailed study of W boson production in association with jets at hadron colliders started in the 1980s motivated by the top quark searches. Additional jets come from radiation of additional quarks or gluons. Because they carry color charge, quarks and gluons undergo the process of parton shower and hadronization forming jets in the detector. *Parton shower* is a process in which a high energy colored particle emits a low energy colored particles, while *hadronization* is a process in which colored particles combine to form color neutral particles. Parton shower and hadronization cannot be computed analytically. They have to be modelled using Monte Carlo simulations. As a result of these processes, the number of jets in the final state doesn't necessarily correspond to the number of partons outgoing from the hard process. Many theoretical issues arise when trying to compute cross sections for W+jets processes. Divergences while calculating amplitudes come from emission of low energy particles or collinear jets. These problems are solved by introducing a cut-off called factorization scale. Other divergences come from integrating higher-order loops. Usually this type of divergence is than included into renormalized coupling constant. This procedure, however introduces a certain scale dependence into the result which will be further discussed in Section 2.2.1.

2.2 W + b jets at hadron colliders

First theoretical computations of W boson production in association with b jets were published in 1993 [15]. However only recently enough luminosity has been collected at hadron colliders to allow cross section measurements. This process was first interesting as a background to top quark searches and measurements where top quark decays to W boson and a b quark. In the past few years, with the Higgs boson discovery, an important open question is whether this new particle also couples to fermions, and in particular to bottom quarks. SM Higgs boson (m_H = 125 GeV) branching ratio for decays into a bottom quark-antiquark pair ($b\bar{b}$) is $\approx$ 58%. The study of this decay channel is therefore essential in determining the nature of the newly discovered boson. The measurement of the H $\rightarrow b\bar{b}$ decay will be the first direct test the observed boson interaction with the quark sector. Direct measurement of this coupling requires a measurement of the corresponding Higgs boson decay. The result of the study of Higgs decay to bottom quarks was recently reported by the CMS experiment in [16, 17] which shows Standard model Higgs boson coupling with the significance of 2.1 standard deviations. Higgs coupling to the top quark is measured in the gluon-gluon fusion production channel. In the SM this process is dominated by the virtual top quark loop. Measurement for the top-quark couplings show agreement with the SM prediction [18]. There are also searches for beyond SM physics where contributions from W+b jets process is substantial, among others supersymmetry searches with lepton, b jets and missing energy in the final state [19].

The complexity of the proton collisions is arising from the composite nature of protons. Although protons are mainly composed of valence *uud* quarks, other quarks, called sea quarks, can be excited as well. In principle, all these partons have a probability to participate in the collision. The accurate description of the collision events heavily relies on the combination of theoretical calculations and experimental findings. Usually this description is divided into separate stages, which occur at different energy scales. Going from higher energy scales and smaller distances, processes which describe particle are added depending on the available phase space ending in the stable particles detected in the detector. This evolution can be summarized as follows:

- **Hard process** - resulting in the production of heavy or highly energetic particles and subsequent decay of a heavy particle, all of which is described through matrix elements.
- **Parton shower** - the process of radiating lighter particles, e.g photons or gluons, which tend to be collinear with the originating particle
- **Hadronization** - quarks and gluons form hadrons, which are usually unstable and eventually decay into long lived particles detected in the detector.

All these stages are represented in figure 2.2 in an event where top quark pair is produced in association with a Higgs boson.

2.2.1 Cross sections at hadron colliders

Determining cross sections for processes at hadron collides is not an easy task. The proton is a composite object consisting of partons, thus it is necessary to include its internal structure as well as the diagrams for the hard scattering process of interest. Quarks and

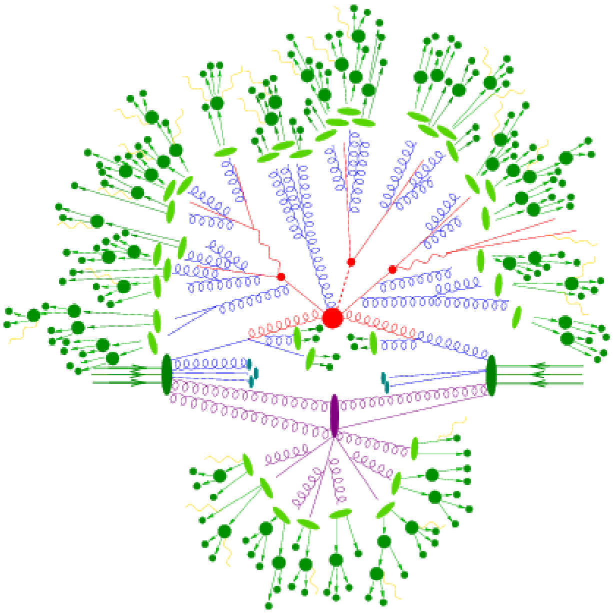

FIGURE 2.2: Drawing represents a proton-proton collision production a ttH event. The hard interaction, represented with big red circle, is followed by the decay of both top quarks and the Higgs boson. Additional hard QCD radiation and a secondary interaction, shown in red and purple, take place before the final-state partons hadronise (light green) and hadrons decay (dark green). Photon radiation is shown in yellow and it can occur at any stage [20].

gluons within the proton interact through strong force and are described using quantum chromodynamics. Calculations within QCD are possible thanks to *asymptotic freedom* and *factorization theorem*. Since the strong force coupling constant α_s depends on the scale of the process, for high momentum transfers ($Q >> \Lambda_{QCD} \approx 200$ MeV) it becomes sufficiently small to make perturbative expansion in α_s possible. This feature is called *asymptotic freedom* and it is used to determine the hard process cross section. Figure 2.3 shows the results of the α_s measurements which is in complete agreement with the QCD predictions of asymptotic freedom.

The *factorization theorem* is introduced to separate the two contributions in the cross section calculation, the contribution from the hard process calculated using perturbative QCD and the contribution from the internal structure of the proton. This means that hard scattering between partons is independent from the proton internal structure. The factorization scale is introduced as a cut-off below which perturbative QCD calculation

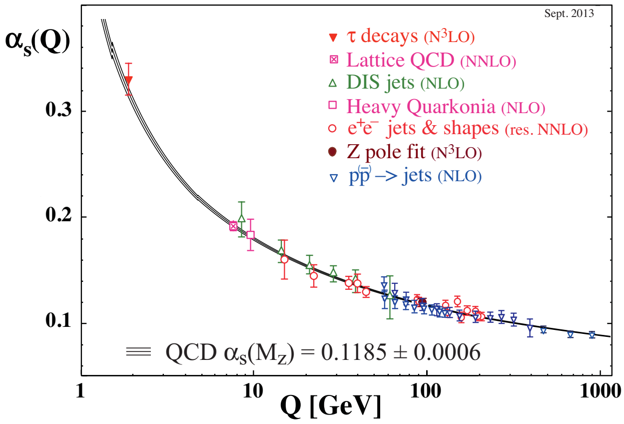

FIGURE 2.3: Summary of measurement of strong coupling constant α_s as a function of momentum transfer[21].

cannot be performed. The facorization is possible because hard and soft parts of the process happen at different time scales. The cross section calculation for a process with

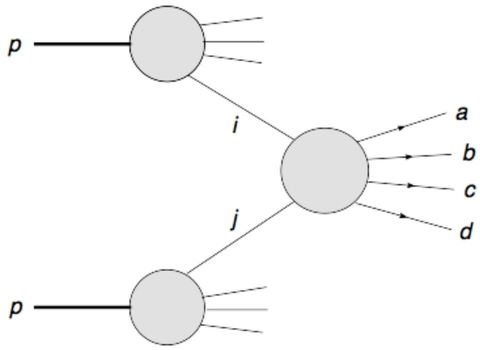

FIGURE 2.4: Drawing of a proton-proton collision.

two protons in the initial state and some interesting final state which we call X requires the following steps (as described in [22]):

1. Identify the leading order (LO) partonic processes that contribute to X
2. Calculate the corresponding hard scattering cross section
3. Determine the appropriate PDFs for initial state partons
4. Make a specific choices for factorization(μ_F) and renormalization(μ_R) scales

5. Perform integration over the fraction of momentum available for a given parton(x)

The cross section at hadron collides is thus a convolution of the hard scattering perturbative cross section and two incoming parton distribution functions.

$$\sigma_{AB} = \sum_{n=1}^{\infty} \alpha_s^n(\mu_R^2) \sum_{i,j} \int dx_1 dx_2 f_{i/A}(x_1, \mu_F^2) f_{j/B}(x_2, \mu_F^2) \sigma_{ij \to X}^{(n)}(x_1 x_2 s, \mu_R^2, \mu_F^2) \qquad (2.2)$$

Equation 2.2 shows cross section perturbation series in α_s, n denotes the order of the series where $n = 1$ is LO, $n = 2$ is NLO, etc. Hard process cross section between two partons $\sigma_{ij \to X}^{(n)}$ is computed in the framework of perturbative QCD and depends on s which is the squared center of mass energy. Two functions denoted with $f_{i/A}$ and $f_{j/B}$ correspond to the probability density that parton $i(j)$ with proton momentum fraction $x_1(x_2)$ will be found inside a proton. and are called parton distribution functions (PDFs). These functions cannot be computed using perturbative QCD because momentum transfer values are small and the coupling constant becomes large. This phenomenon is called *confinement* and it requires different treatment for the quarks inside the proton. The internal structure of a proton is described using parton distribution functions(PDF) which are determined through deep inelastic scattering experiments. The sum over all combinations of partons has to be computed. The integral over available phase space for proton fraction momentum dx is usually carried out numerically. Here μ_F represents the *factorization scale* and μ_R is the *renormalization scale* for running coupling constant. They are arbitrary cut-offs used to remove nonperturbative effects and be able to make perturbative calculations. If the cross section is computed in full series, μ_F and μ_R should cancel out, and the scale dependence should disappear. However, since fewer orders are used and some residual scale dependence is still present, this dependency can be used to estimate the contribution of the missing orders in the series.

The factorization scale controls soft and collinear emissions that can spoil the perturbative calculation. These emissions are then absorbed into the PDF for transverse momenta below μ_F. Using DGLAP equations, PDFs can be evolved to any momentum transfer value which is described in detail in [22], and make the factorization cut-off possible. PDF evolutions are shown figure 2.5 for one specific PDF function (MSTW) at momentum transfer values of $Q^2 = 10$ GeV^2 and $Q^2 = 10^4$ GeV^2 which corresponds to the typical momentum transfers for W boson production. At high momentum transfer values, sea quarks and gluons carry a much larger portion of the proton momentum and b quark distributions become relevant. The renormalization scale is another cut-off used to

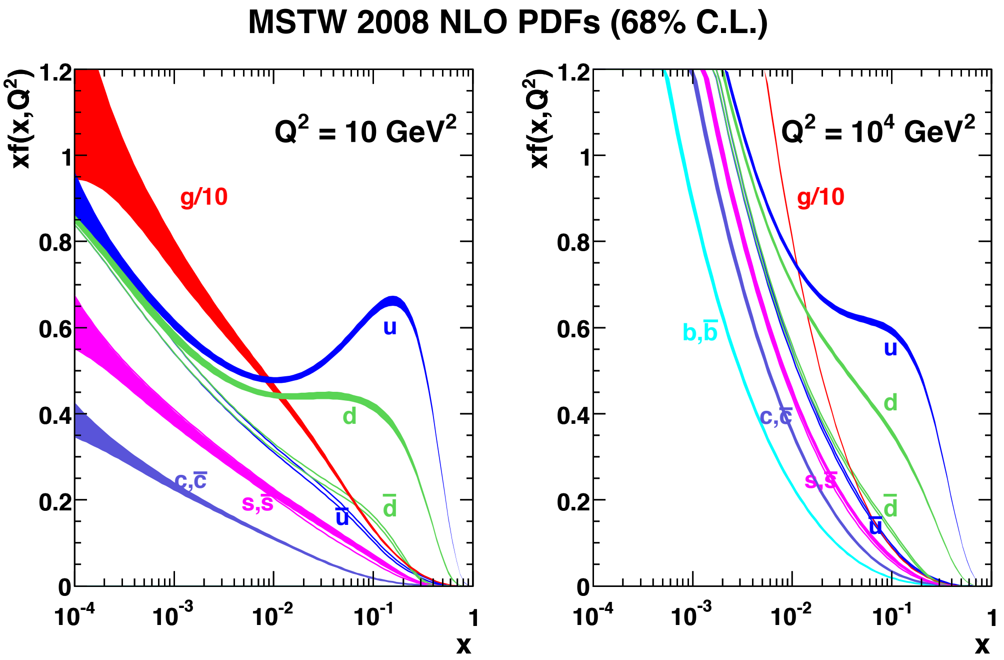

FIGURE 2.5: Parton distribution functions calculated by the MSTW group for $Q^2 = 10$ GeV^2 (*left*) and $Q^2 = 10^4$ GeV^2 (*right*) [23]

control divergences from the integration of high momentum loops in parton cross sections. If the momenta are larger than μ_R, the divergences are absorbed in a redefined coupling constant α_s and the cross section calculation becomes finite. This approach is common in renormalizable field theories. However, such result depends on the renormalization scale and the resulting dependency can be calculated using renormalization group equation (RGE) [24].

Usually the factorization and renormalization scales are chosen to be identical and close to the scale of the process in question ($\mu_F = \mu_R = \mu_0 \approx Q$). The choice of the scale in the case of W boson production is usually around the mass of the W boson. Taking into account specific kinematical properties of each event, a dynamic scale can be defined, for example $\mu_0^2 = m_w^2 + p_{T,W}^2$. In case of W boson and b jets production, adding the b quark mass or transverse momentum to the scale is also a viable option.

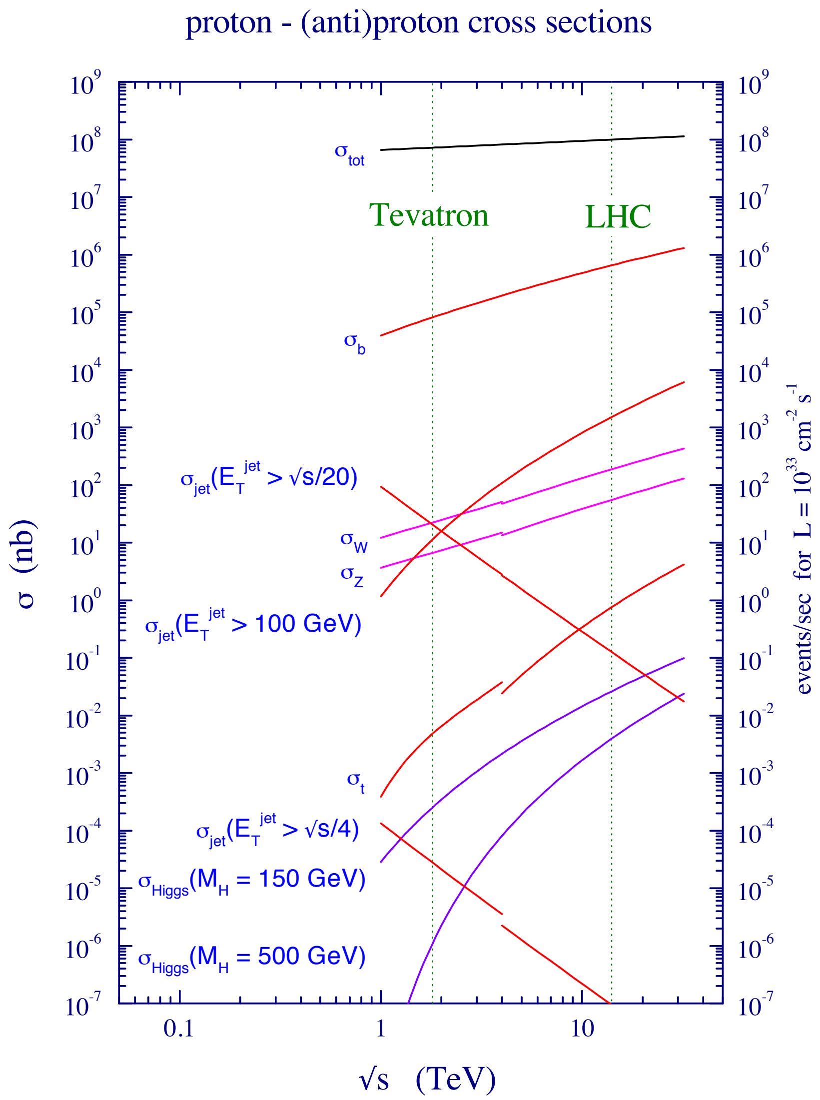

FIGURE 2.6: SM cross sections as a function of center of mass energy.[22]

Figure 2.6 shows some interesting SM cross sections in proton-proton and proton-antiproton collisions as a function of a the center of mass energy. All cross sections have been computed to the NLO order in QCD using the above described procedure.

2.2.2 Theoretical contributions to Wbb cross section

From the theoretical point of view, calculations of W+b jets processes can be divided into two categories:

- only light quarks in the initial state as shown in figure 2.7 - four flavour scheme (4FS)
- b quark in the initial state as shown in Figure 2.8 - five flavor scheme (5FS)

An additional contribution to Wbb production at hadron colliders comes from double parton interactions where a W boson and a pair of b quarks is produced in different hard process inside the same collision as shown in Figure 2.11. This contribution will be discussed in Section 2.2.2.1.

The rationale behind using 4FS or 5FS is discussed in detail in [25]. The four flavor scheme approach assumes that bottom quarks are heavy and can only be created as pairs in collisions with high momentum transfer or as a decay product of t quark. Heavy quarks are not included in the initial state and their parton distribution function is set to zero, which means an effective theory is created where heavy quarks do not enter the computation of running coupling and the evolution of PDFs. If it happens that the scale of the process is much higher than the mass of the b quark, for example in the production of massive bosons, large logarithms of the type $log(Q^2/m_b^2)$ appear and can spoil the convergence of a fixed order perturbative expansion and introduce a large scale dependence into the final result. In the five flavor scheme calculations include b quark in the initial state allowing for some new and simpler processes to become available. These calculations allow resummation of possibly large logarithms of type $log(Q^2/m_b^2)$ into the b quark parton distributions function possibly transforming some higher order calculations into much simpler LO calculations. The result in [25] shows that at the LHC 4-flavor calculations are well behaved and two schemes are in good agreement. The typical size of the possibly problematic logarithms in four flavor scheme at hadron colliders is not large enough to spoil convergence. On the other hand, five flavor scheme is less dependent on the scale of the process and show smaller uncertainties which is in general very good for predictions of inclusive observables like the total cross section.

First LO calculations for associated production of a W boson and heavy quarks at hadron colliders were presented in 1993 [15]. Feynmann diagram for LO W + 2 b jets production is shown in figure 2.7. Exact LO matrix element has been computed and higher order corrections were estimated using Monte Carlo. Their results are summarized in the Figure 2.9 where the differential cross section for W+2 b jets as a function of the leading b jet p_T is shown. Two scale choices have been studied, the first one with $\mu_0 = M_{bb}$, which is the invariant mass of the dijet system and is represented with a solid line. The second choice is $\mu_0 = m_W + p_T^W$ and is represented with the dotted line. Looking at the normalizations of two diagrams, the difference is clearly visible which indicates a strong dependence of the total cross section scale. However, the shape of the differential cross section shows the same behavior in both cases, which means that the scale only affects the total cross section.

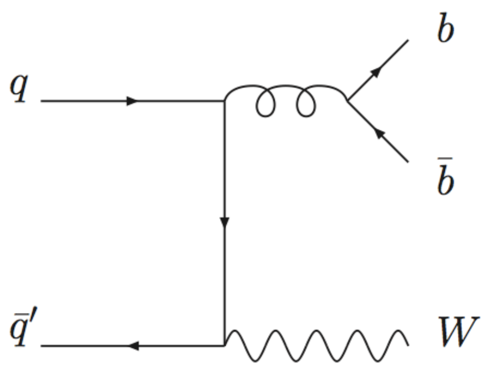

FIGURE 2.7: LO Wbb Feynmann diagram. The pair of b quarks is created from a gluon through a process called gluon splitting.

Later development of theoretical calculations was strongly motivated by reducing the scale dependence of the result and it included adding additional partons to the final state. This was a first step towards the full NLO calculation. The only thing missing

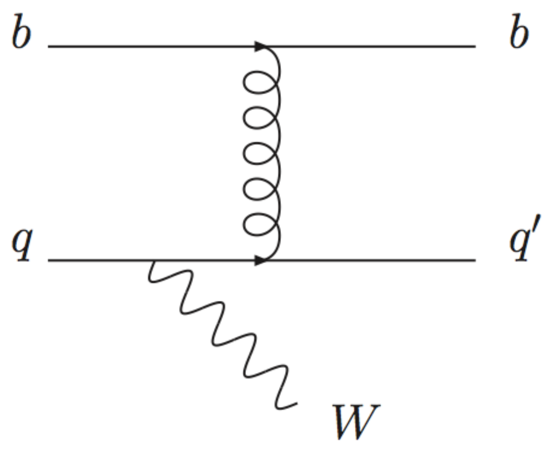

FIGURE 2.8: Wbb production within 5 flavor scheme

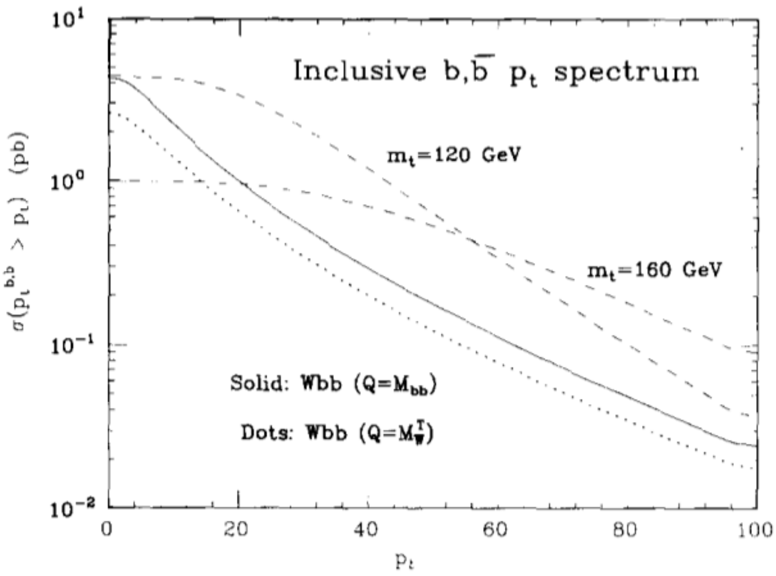

FIGURE 2.9: Scale dependence of Wbb cross section [15].

was to take into account the loop effects. This approach made it possible to access some previously inaccessible kinematics, however at the expense of introducing additional scale dependence. The list of new final states is simple and it includes $Wb\bar{b}q$, $Wb\bar{b}q\bar{q}$, $Wb\bar{b}\bar{q}q'\bar{q}'$... For the measurements at the LHC in particular, calculations for new initial states qg and gg were of great importance. First results for W+2 jets were published in [26]. Additional calculations were shown in [27] for up to six additional jets in the final state. Although these processes are suppressed by an additional α_s factor, the gluon PDF inside a proton is much larger than anti-quark. This production mechanism is therefore significant at the LHC energies.

First full NLO calculations were published in 2006 [28]. Events with b jet pair in the final state were selected, with momentum of the dijet system p_T >15 GeV and a pseudorapidity less than 2. Results were shown for two categories, inclusive and exclusive, depending on the treatment of extra jets. In the inclusive case events with additional jets were included, while in the exclusive case exactly two jets were required. Figure 2.10 shows the overall scale dependence of LO, NLO inclusive and NLO exclusive total cross-sections, when both renormalization scale and factorization scale are varied independently between $\mu_0/2$ and $4\mu_0$ (with $\mu_0 = m_b + M_W/2$), including full bottom-quark mass effects. NLO cross sections have a reduced scale dependence over most of the range of scales shown, and the exclusive NLO cross-section is more stable than the inclusive one especially at low scales. The effect of the b quark mass has been shown to affect the total NLO cross section on the order of approximately 8%. This is expected to be small when considering well separated jets.

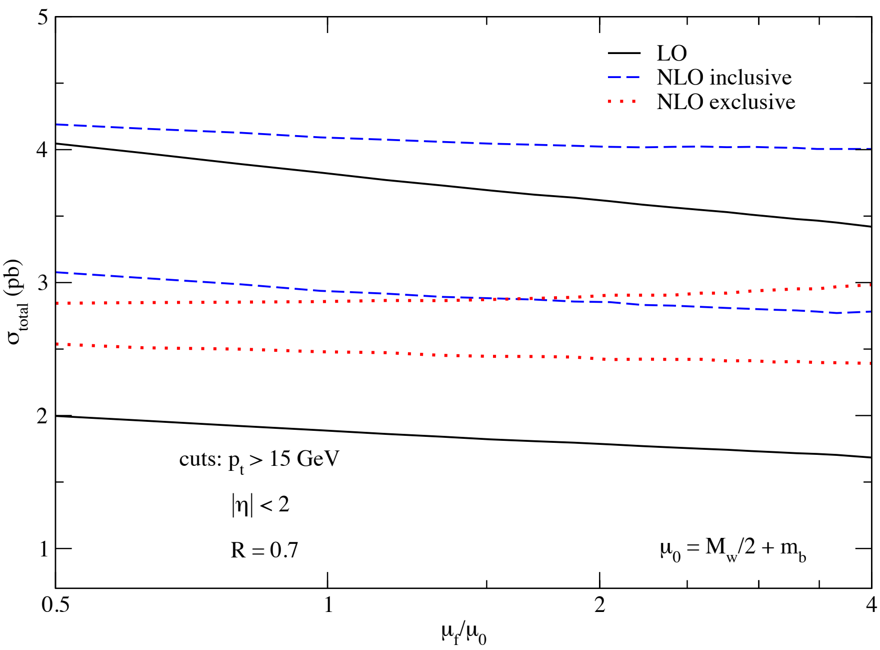

FIGURE 2.10: Wbb NLO scale dependence[28]

New results published in 2007 explored in particular NLO corrections for events with W boson and two jets where at least one is b-tagged. It was shown that for LHC the correction factor is ≈ 1.9. This paper was interesting in particular for its study of soft and collinear topologies, where two b quarks merge into one. Additionally, b quarks in the initial state were considered, giving rise to processes like $bq \rightarrow Wbq'$ shown in figure 2.8. The parton distribution function for b quark needed to be determined perturbatively using DGLAP equations. Another approach is to consider a gluon in the initial state, which then splits to $b\bar{b}$.

2.2.2.1 Double parton scattering

Multiple parton interactions happen due to the composite nature of the proton. Usually it is assumed that only one hard scattering occurs per bunch crossing. The probability of single parton interaction in hadron collisions is very small thus having two or more interactions is highly suppressed. However, sometimes it can happen that two such partons exist which results in two hard scatterings in the same collision. This phenomenon is called Double Parton Scattering (DPS) and is shown in Figure 2.11. In the framework of this thesis, two partons are responsible for the creation of a W boson and other two for creation of a pair of b jets.

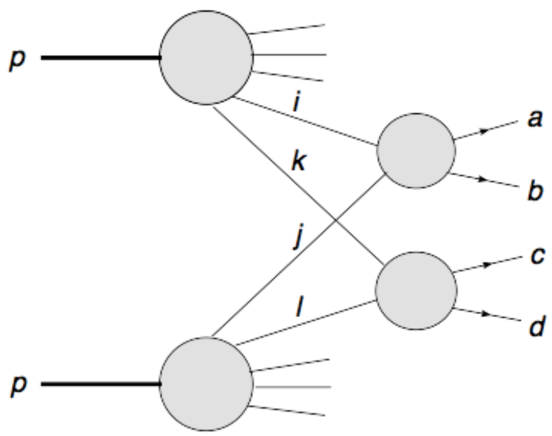

FIGURE 2.11: Double parton scattering

Double parton scattering cannot be modeled in the framework of preturbative QCD, but it is approximated using simulations. The phenomenology of DPS starts from the assumption that factorization between the two hard processes is possible, as well as factorization between hard processes and proton kinematics. Cross sections for hard scatterings are computed separately for each pair of partons. However, instead of using regular parton distribution functions, a new set of distribution functions has been defined which are called Double Parton Distribution Functions (dPDFs). Factorized cross section for two hard processes A and B to happen in proton-proton scattering can be written as:

$$\sigma^{DPS}_{(A,B)} \sim \sum_{i,j,k,l} \int dx_1 dx_2 dx_1' dx_2' d^2 b \Gamma_{ij}(x_1, x_2, b; Q_1, Q_2) \sigma^A_{ik}(x_1, x_1') \\ \sigma^B_{jl}(x_2, x_2') \Gamma_{kl}(x_1', x_2', b; Q_1, Q_2) \tag{2.3}$$

Parton level cross sections are denoted with σ_{ik}, for hard process between partons i and k, and σ_{jl} for hard process between partons j and l. These are the same as for single parton scattering and are known for most of the processes of interest today. The quantity $\Gamma_{ij}(x_1, x_2, b; t_1, t_2)$ represents the double parton distribution function, which describes the probability of finding a parton i with momentum fraction x_1 at scale Q_1 inside a proton together with a parton j with momentum fraction x_2 at scale Q_2. Another parameter in this distribution function is b, which describes the transverse distance between two partons. The scales Q_1 and Q_2 and correspond to characteristic scales of hard processes A and B. For example in the framework of this thesis the W boson production would correspond to process A and production of two b jets would correspond to process B. This study is described in detail in [29]. Usually, it is assumed that $\Gamma_{ij}(x_1, x_2, b; t_1, t_2)$ can be decomposed into two components, longitudinal and transversal in the following way:

$$\Gamma_{ij}(x_1, x_2, b; t_1, t_2) = D^{ij}_h(x_1, x_2; t_1, t_2) F^i_j(b) \tag{2.4}$$

The interpretation of the function $D^{ij}_h(x_1, x_2; t_1, t_2)$ within QCD is the probability of finding parton i with scale Q_1 and parton j with scale Q_2. These functions cannot be determined using perturbative QCD. To make an accurate cross section predictions it is essential to have good modelling and to correctly take into account the correlations between longitudinal momenta and transverse position.

More details on how to determine dPDFs can be found in [30]. In the simplest case $D_h^{ij}(x_1, x_2; t_1, t_2)$ can be taken as a product of single parton distribution functions taking into account effects like $x_1 + x_2 < 1$. Since $F_j^i(b)$ is the only part of $\sigma_{(A,B)}^{DPS}$ that depends only on b, integration over b can be performed giving an effective cross section σ_{eff} which is related to the size of the proton and can be seen as an effective area of the interaction. This approach yields a simplified expression for the double parton scattering cross section:

$$\sigma_{(A,B)}^{DPS} \sim \frac{1}{\sigma_{eff}} \sigma_{(A)}^{SPS} \sigma_{(B)}^{SPS} \tag{2.5}$$

Here $\sigma_{(A)}^{SPS}$ and $\sigma_{(B)}^{SPS}$ are single parton scattering cross section which can be obtained using equation 2.2.

However, this factorized approach does not take into account some simple correlations, e.g. between the probability to find a quark of some flavor and to find find another quark with the same flavor. While for some simple cases with low parton momentum fractions this factorized approach may give accurate results, for more complicated cases like calculating fiducial cross sections, acceptance cuts can spoil the equation. Thus, a simulation of the full kinematical effects is necessary.

A first measurement of σ_{eff} has been performed by the AFS collaboration at the ISR (CERN) which obtained $\sigma_{eff} \sim 5$ mb at 63GeV. Both CDF and D0 collaborations at Tevatron, Fermilab (IL, USA) reported $\sigma_{eff} \sim 15$ mb which is roughly 20% of the total $p\bar{p}$ cross section at Tevatron energies. Their data also show no sign of dependence on x in measured σ_{eff} in the accessible x ranges. Later measurements performed by ATLAS ans CMS collaborations are in reasonable agreement with previous results. All results are summarized in Figure 2.12.

Double parton scattering measurement at CMS is performed by selecting events with

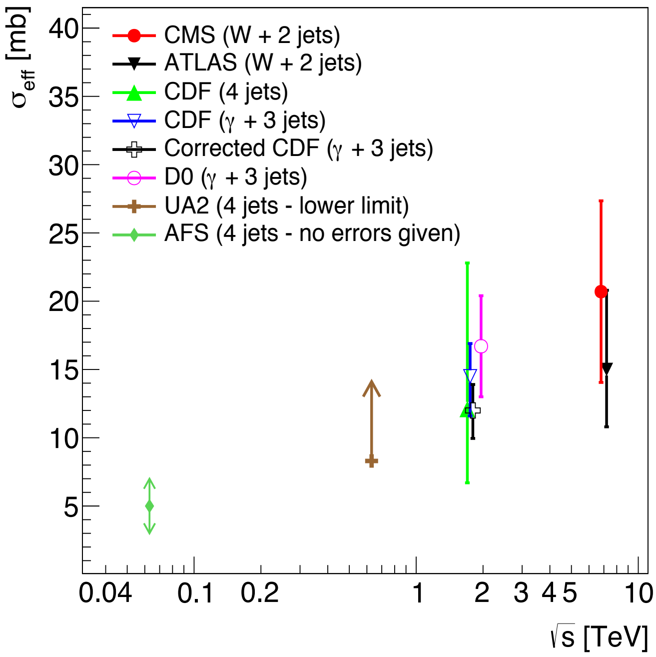

FIGURE 2.12: Center of mass energy dependence of σ_{eff} as reported from different collaborations. All these measurements use different approaches to estimate σ_{eff}. [31]

a W + 2-jet final state where one hard interaction produces a W boson and another produces a dijet [32]. The W + 2-jet process is attractive because the muonic decay of the W provides a clean tag and the large dijet production cross section increases the probability of observing DPS. Events containing a W + 2-jet final state originating from single parton scattering (SPS) constitute an irreducible background. Results were obtained by performing a template fit to two uncorrelated variables: the relative p_T balance between two jets (Δp_T) and the angle between W boson and a dijet system. Obtained results again show that the contribution of DPS to the total cross section is $\sim 20\%$ which is in good agreement with previous Tevatron results. The DPS contribution in the case od W + 2 b jets is estimated to be $\sim 15\%$. [33]

2.3 The previous measurements

Previous measurements of a W boson produced in association with b quarks have been performed on different experiments. However, the final states and phase space used in these measurements were different, which means that the results cannot be directly compared. They can nevertheless be compared with theoretical predictions. This process was measured for the first time at Tevatron with D0 and CDF experiments at $\sqrt{s} = 1.96$ TeV. The CDF collaboration published its result in 2009 and the cross-section measured is that of jets from b-quarks produced with a W boson [34]. The event selection is based on reconstructing a leptonically decaying W boson, and one or two jets where at least one has to be b-tagged. Events with jets from light quarks are vetoed with a cut on the secondary vertex mass. Contribution of other background events containing a b quark in the final state (e.g. events with top quark) is estimated using Monte Carlo simulations. The measured cross section is 2.8 standard deviations higher than the corresponding theoretical prediction.

The D0 collaboration published their result in 2012. with a somewhat different phase space definition [35]. The difference with respect to the CDF measurement consists in the inclusion of events with 3 jets and reduced pseudorapidity range in which the measurement was performed. The measurement technique is similar to that of CDF, although b-tagging algorithms were slightly different. The measured cross section was in good agreement with the SM prediction.

First measurements at the LHC were published by the ATLAS collaboration based on 36 pb^{-1} of integrated luminosity at $\sqrt{s} = 7$ TeV. One year later they improved their measurement using $4.6\mathrm{fb}^{-1}$ [36]. Selected events contain one reconstructed electron or muon, significant amount of missing transverse energy and one or two jets where exactly one is b-tagged. The phase space is divided in two regions, depending on the number of jets. Events with exactly 2 b jets and events with more than 2 jets are vetoed in order to suppress background events from top quark decay. The results are shown in Figure 2.13. The cross section measurement in the one jet region shows an excess corresponding to 1.5 standard deviations. In the two jet region, the measured cross section is in good agreement with theoretical predictions. A differential cross section measurement as a function of leading b jet transverse momentum has been performed for the first time. The results are shown in figure 2.14. The cross section measurement in the one jet region is again higher than NLO predictions but within theoretical and experimental uncertainties. The cross section measured for the events with two jets is in good agreement with the theoretical prediction.

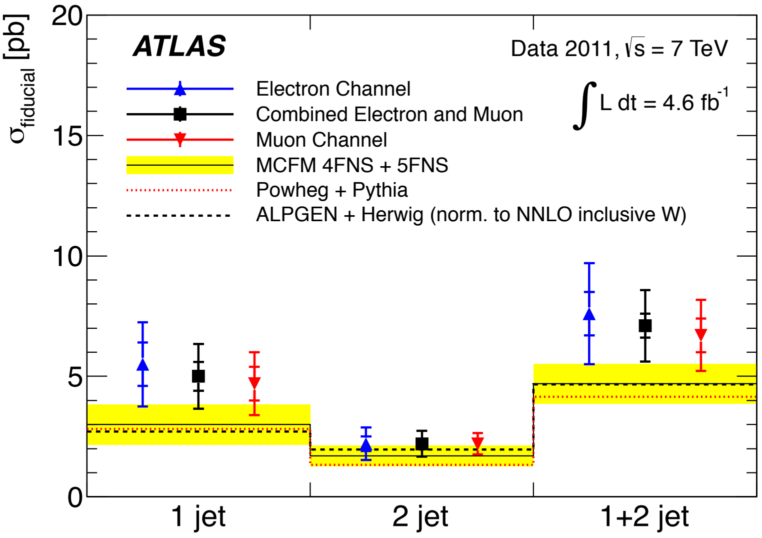

FIGURE 2.13: Measured fiducial cross-sections in the electron, muon, and combined electron and muon channels. The cross-sections are given in the 1-jet, 2-jet, and 1+2-jet fiducial regions. [36]

The CMS collaboration published so far a result analysing the data collected during 2011 at 7 TeV corresponding to 5 fb^{-1} of data. Selected events contained a muon and missing transverse energy in the final state, together with two b-tagged jets. All additional lepton and jet activity was vetoed to reduce the background contributions. Figure 2.15 shows the leading jet transverse momentum distribution used for signal extraction. The measured cross section is in excellent agreement with the SM prediction. [33]

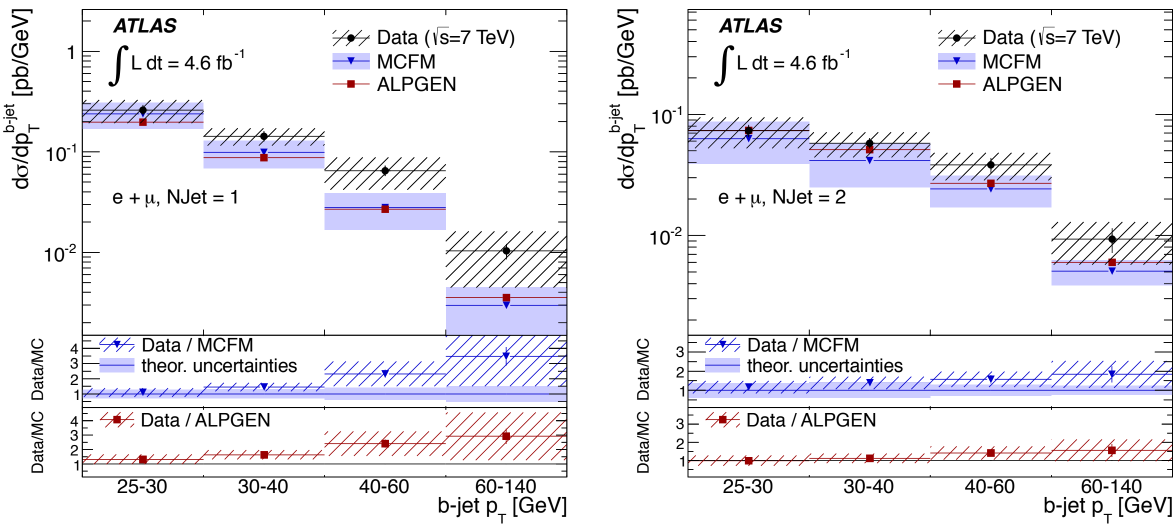

(A) (B)

FIGURE 2.14: Measured differential W+b-jets cross-sections as a function of leading b-jet p_T in the 1-jet (2.14a) and 2-jet (2.14b) fiducial regions, obtained by combining the muon and electron channel results. [36]

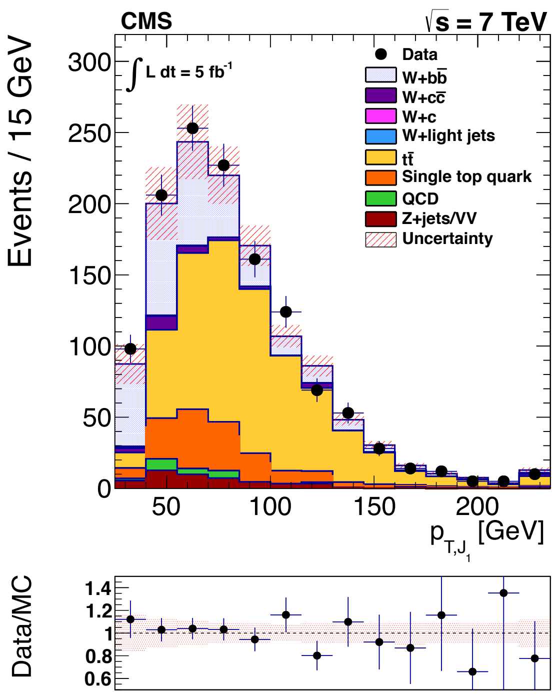

FIGURE 2.15: Leading jet transverse momentum distribution used for signal extraction in W+bb total cross section measurement with the CMS experiment. [33]

Chapter 3

The Large hadron collider

CERN is the largest particle physics laboratory in the world, located near the city of Genava, on the French-Swiss border. It was founded in 1953 by 12 countries and today it has 21 member states. Its main function is to provide particle accelerators and infrastructure for high energy physics experiments. Major physics results at CERN include the discovery of neutral currents, discovery of W and Z bosons, creation of antihydrogen atom and direct observation of CP violation among others.

Current accelerator complex is a chain of smaller accelerators with increasingly higher energies of which the largest one is Large Hadron Collider (LHC) (Figure 3.1). The LHC is a proton-proton collider which is also able to deliver lead-lead and proton-lead collisions. Protons are obtained by taking hydrogen atoms and stripping them of the orbiting electrons, and are accelerated by a small linear accelerator Linac2 to 50 MeV and injected to PS Booster. After reaching 1.4 GeV, protons are injected to Proton Synchrotron and accelerated to 25 GeV. The next accelerators in the are the Super Proton Synchrotron (SPS) with energy of 450 GeV, and the LHC with designed beam energy of 7 TeV.

In this chapter, we will briefly go through the motivation for the LHC design, building blocks of the accelerator together with its performance during the past few years.

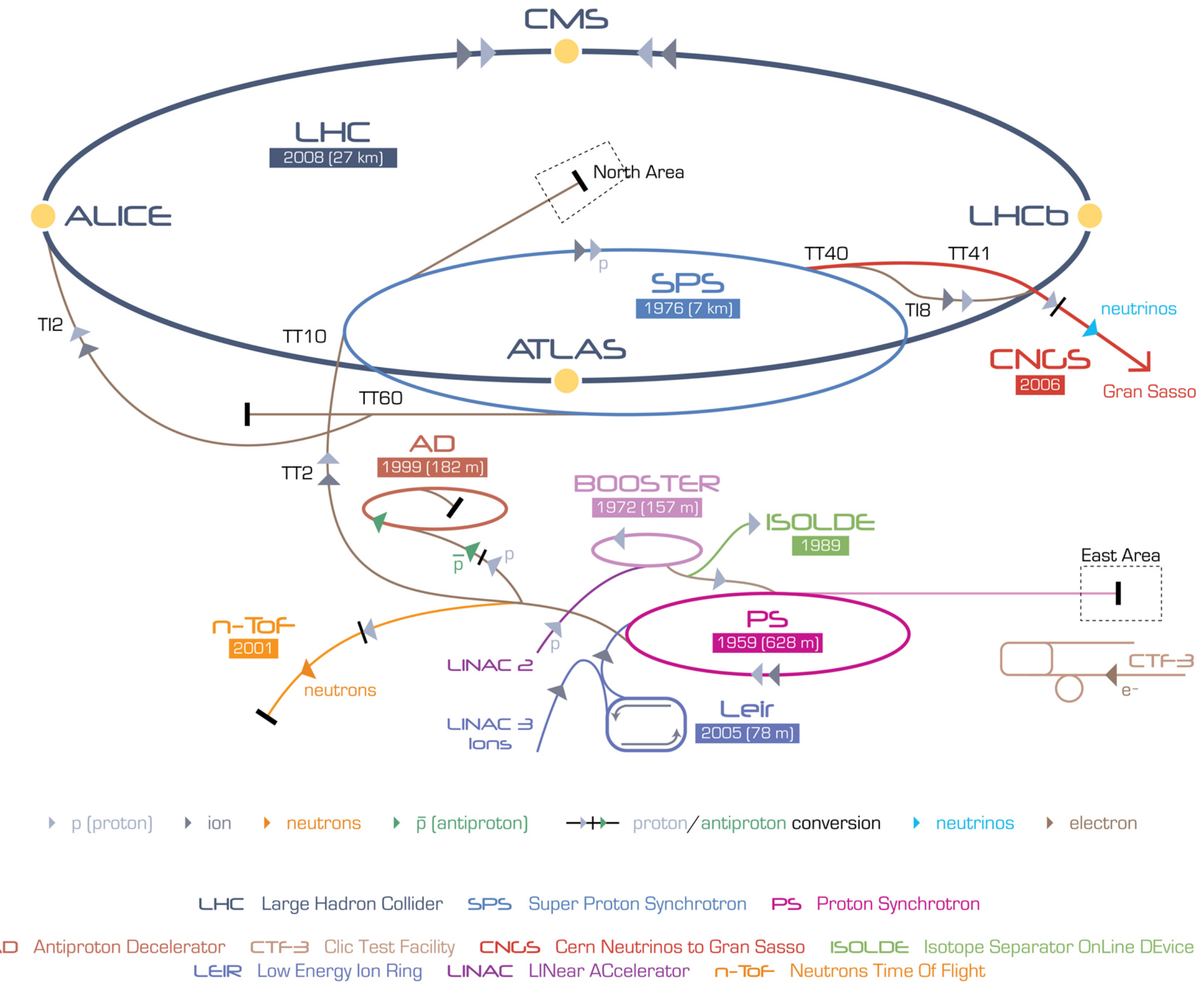

FIGURE 3.1: Schematics of Large Hadron Collider

3.1 Physics goals for the LHC

The SM of elementary particles describes nicely all known particles and interactions, however there are still some unanswered questions. One of the major open questions was the existence of Higgs boson which was recently answered with the discovery of a new boson at 125 GeV. In order to be able to claim such a discovery, all known SM processes have to be well measured and the behavior of the experimental device has to be well understood. These requirements lead to many precision measurements which determined precisely cross sections, couplings, masses and other parameters within the SM. Any deviation from predicted values can be an evidence for the existence of physics beyond SM. One of the questions that remain open is the unification of fundamental forces. One attempt to achieve this goal is the theory of supersymmetry which predicts that each particle has its heavier supersymmetric partner and at high energies could unify strong and electroweak forces. If the theory of supersymmetry is correct, lightest supersymmetic particles would be stable and could be detected at the LHC. Such particle would also be a great candidate for the dark matter considering it would interact only weakly and as such would fit nicely into the present dark matter theories. Another open problem is to quantify the matter-antimatter asymmetry. That would explain why the universe as we know is made of matter only. Other theories that involve extra dimensions, bound states of quarks and leptons and other exotic models can be tested as well. The LHC comprehends also a very vast heavy ion program: lead-lead and lead-proton collisions are produced during which a state called gluon plasma is searched, which would resemble the state of the early universe.

During the past few years, various models for new physics have been extensively tested, and having found so far no significant deviation from SM only processes, new exclusion limits have been set. After three years of data taking at 7 and 8 TeV, and a shutdown period of two years to upgrade the LHC and the detectors to an increase of energy, LHC is now almost ready to deliver collisions at record energies of 13 TeV which could hopefully show signs of new physics.

3.2 Design of the LHC

The LHC is located inside a 27 km tunnel, which lies between 45 m and 170 m below the ground surface and previously housed the LEP accelerator. Beams circulating inside the LHC, collide at four interaction points. At each of these points, a detector has been built to record the products of particle collisions. This thesis was done using data collected with the CMS (Compact Muon Solenoid) detector [37]. Another detector with the same purpose but different design is the ATLAS (A Toroidal LHC Apparatus) detector located at the opposite side of the LHC ring [38]. These two are so called multiple purpose particle detectors, which cover a wide range of physics topics, from searches for Higgs boson and supersymmetry to SM precision measurements. ALICE (A Large Ion Collider Experiment) is designed to study quark-gluon plasma by measuring mainly lead-lead collisions and in addition lead-proton and proton-proton collisions [39]. LHCb (LHC Beauty) is optimized for the detection of B-hadrons and hence study of B physics. [40]. Two other experiments TOTEM and LHCf are placed away from the interaction point to measure the collision products along the beam direction.

The LHC is made out of nearly 9600 different magnets, including dipoles, quadrupoles, sextupoles, octupoles, etc. The largest portion of the accelerator is made out of 1232 dipole magnets which which use superconductive niobium-titanium (NbTi) cables that undergo a phase transition to a supercondutive state at 9.2K. In order to achieve superconductivity and withstand very high currents (11850 A), the cables have to be cooled with superfluid helium to less than 2K. They create large magnetic fields, which can reach 8.2T which bend the proton beams around the ring. Other higher order magnets are used to focus and correct the beam.

Two proton beams are counter-circulating inside a single cryogenic structure which requires opposite magnetic field direction for each of the beams in order to be steared along the same circumference. One of the LHC dipole magnets is shown schematically in Figure 3.2 together with the drawing of the magnetic field inside the dipole.

Beams in the LHC are injected in series of bunches separated by a vacuum gaps, with each bunch having more than 10^{11} protons. Bunches are arranged in trains of 72 bunches with 25 ns spacing between them and 12 empty bunches between trains. Acceleration is provided by the radio frequency superconducting cavities (RF). It takes approximately 20 minutes for the beams to be accelerated from the injection at 450 GeV to the full beam energy. Moreover, RF chambers provide a small corrections of the order of $\sim$ 7 keV per turn to the beam due to the energy loss from synchrotron radiation. After the acceleration, beams are tuned at the interaction points to achieve intersection. Peak collision rate of 40 MHz is achieved when collisions happen at every bunch crossing. Beams are squeezed to

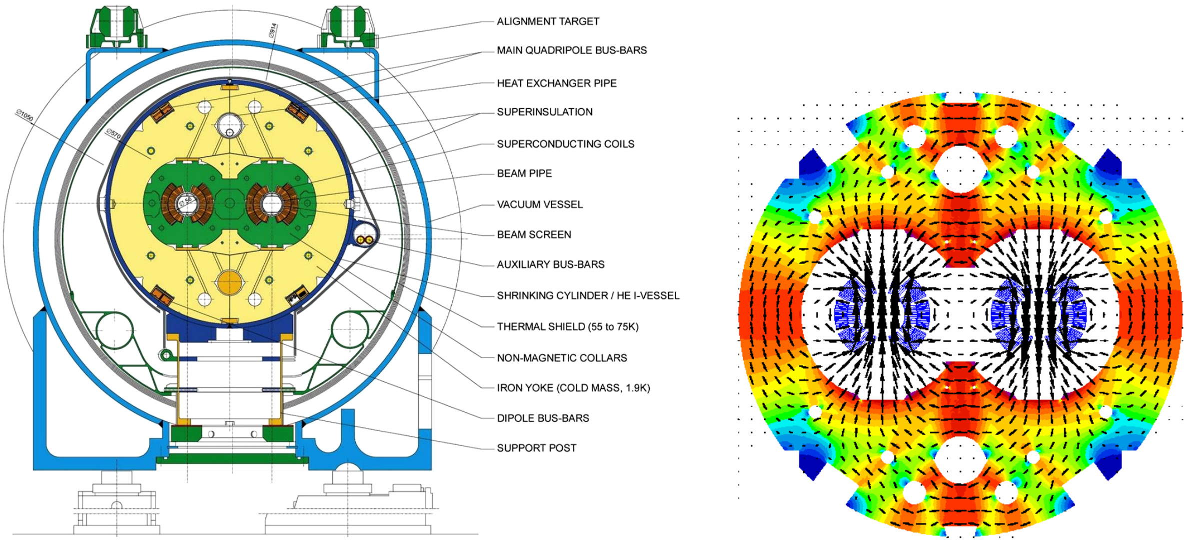

FIGURE 3.2: Schematics of Dipole magnets [41, 42]

a transverse size of $\sim 17\ \mu$m at the interaction point in order to maximize the probability of collision.

3.3 LHC performance

Since the start of the LHC in 2009, there were three years of machine operation, which yielded many physics results among which the discovery of a Higgs boson should be highlighted. The first year of operation, when LHC center of mass energy was 900 GeV, was devoted to commissioning and understanding the machine characteristics with the emphasis on safety and tests of the machine protection systems. In 2011 new energy of 7 TeV, breaking the record of 1.96 TeV previously set by Tevatron. This record was superseded once again in 2012 with center of mass energy going to 8 TeV.

High bunch intensity with 50 ns bunch spacing was used in order to get a good instantaneous luminosity performance. This came at a cost of high number of collisions in one bunch crossing (pile-up) which was around 12 collisions during 2011, and in some cases this number went as high as 20 interactions. With the increase of instantaneous luminosity in 2012, number of pile-up interactions was on the average around 30. Besides proton-proton collisions, LHC successfully delivered lead-lead ion runs in 2010 and 2011. primarily for the ALICE experiment, but also for CMS and ATLAS. On top of that, in the beginning of 2013 there was a successful proton-lead run performed for the first time. LHC design together with the 2012 operations parameters are shown in Table 3.1.

Table 3.1: LHC performance in 2012 together with design performance[41]

Parameter	Design value	Value in 2012
Beam energy [TeV]	7	4
Bunch spacing [ns]	25	50
Number of bunches	2808	1374
Protons per bunch	1.15×10^{11}	$1.6\text{-}1.7\times10^{11}$
Peak luminosity [$\text{cm}^{-2}\text{s}^{-1}$]	1×10^{34}	7.7×10^{33}
Max. number of events per bunch crossing	19	≈ 40
Stored beam energy [MJ]	362	≈ 140

Luminosity (L) indicates the number of collisions per unit of time over the interaction cross section σ:

$$L = \frac{1}{\sigma}\frac{dN}{dt} \tag{3.1}$$

Luminosity for collider experiments is connected to beam parameters:

$$L = \frac{n \cdot N^2 f}{A_{eff}} \tag{3.2}$$

where n is a number of bunches with N protons inside, that are colliding at the revolution frequency f and effective beam area A_{eff}. The amount of data collected in a certain period of time is called total integrated luminosity and is defined as:

$$\mathcal{L} = \int L dt \tag{3.3}$$

During the Run 1 data taking period, the LHC delivered around 24 fb^{-1} of data (figure 3.3) at the energy of 8 TeV with highest instantaneous luminosity of $8 \cdot 10^{33}$ $\text{cm}^{-2}\text{s}^{-1}$. Some of the LHC performance highlights are listed in table 3.2.

TABLE 3.2: LHC performance highlights

Max. luminosity delivered in one fill	237 pb^{-1}
Max. luminosity delivered in 7 days	1.35 fb^{-1}
Longest time in stable beams (2012)	22.8 hours
Longest time in stable beams over 7 days	91.8 hours (55%)

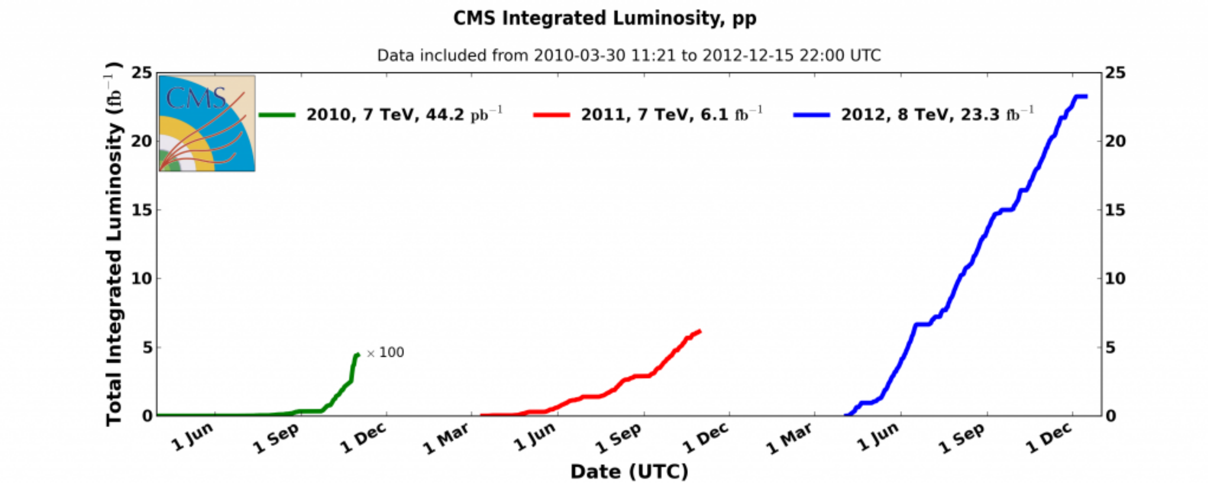

FIGURE 3.3: Luminosity delivered to the CMS experiment

Following a two year shutdown, LHC is anticipating operations at even higher energies of 13 TeV and later 14 TeV. The long term plan includes even higher peak luminosities, installation of the new injector complex and later the beginning of HL-LHC era. The timeline will, of course, be highly affected by the performance and results of the next run.

Chapter 4

The Compact muon solenoid

The Compact Muon Solenoid (CMS) is a general purpose detector designed to cover a wide range of physics topics at the LHC with a layered design approach and coverage of a large portion of the solid angle around the interaction point. The tracking system and calorimeters are placed inside a large soleonid in order to improve the resolution of the momentum and energy measurements. The detector outside the solenoid is aimed primarily to detection of muons. A drawing of the CMS detector is shown in Figure 4.1.

The motivation for the CMS design with respect to its purpose in the LHC program is a very good muon identification and good momentum resolution over wide range of phase space and unambiguous determination of muon charge. Very good inner tracking system allows for detection of charged particles and high efficiency offline b quark and τ tagging. Other important requirements, specially for Higgs searches, is diphoton mass resolution, and photon and electron identification and isolation at high energies. CMS detector with its design meets all these requirements as is shown in following sections of this chapter.

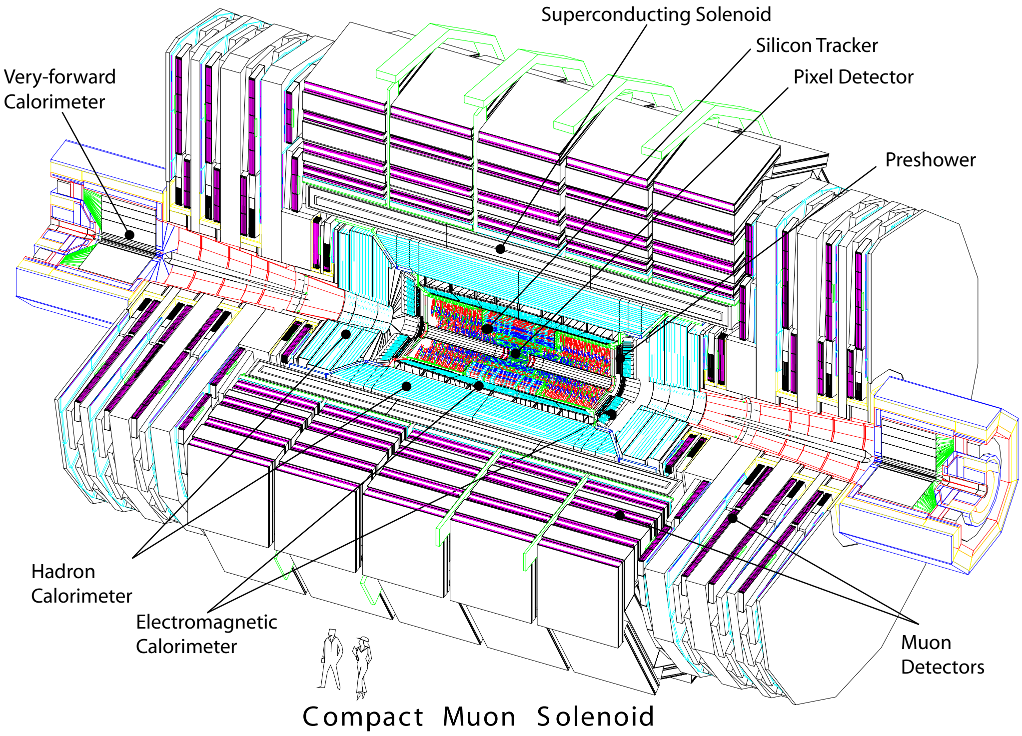

FIGURE 4.1: A drawing of the CMS detector. [37]

4.1 CMS coordinate system

CMS uses a right-handed coordinate system with the origin in the nominal interaction point. $z-$axis is pointing along the beam line. $x-$axis is pointing towards the center of the LHC ring while y-axis points upwards. Two angles are used to describe position inside the detector, azimuthal angle ϕ and polar angle θ. ϕ angle lies in $x-y$ plane with a range $[-\pi,\pi]$ and is defined as $\phi =$arctan(y/x). The other angle θ is usually not used in high-energy physics because differences in θ are not Lorentz invariant. The variable that is Lorentz invariant is rapidity:

$$y = \frac{1}{2} ln \left[\frac{E + p_z}{E - p_z} \right] \tag{4.1}$$

In high energy experiments in the relativistic limit where $E >> m$, a quantity called pseudorapidity is a good approximation of rapidity:

$$\eta = -ln\left[tan\frac{\theta}{2}\right] \tag{4.2}$$

The Lorentz invariance of pseudorapidity means that a measurement of $\Delta\eta$ between particles is not dependent on specifying a reference frame, such as the rest frame of a particle or the laboratory frame. The term "forward" direction refers to regions of the detector that are close to the beam axis, at high $|\eta|$. When the distinction between "forward" and "backward" is relevant, the former refers to the positive z-direction and the latter to the negative z-direction.

In proton-proton collisions, colliding objects are partons and gluons. Given the energy-momentum conservation and the fact that the proton momentum in the plane perpendicular to the beam axis is negligible, the momenta of the final state particles have to be balanced in the $x-y$ plane. This is why transverse momentum is often used in various analyses and is computed as $p_T = \sqrt{p_x^2 + p_y^2}$.

4.2 Solenoid magnet

The CMS solenoid magnet has the length of 12.9 m, an inner diameter of 5.9 m and provides a magnetic field of 3.8 T. The solenoid is large enough to contain inner tracking system and calorimeters which reduces the material budget before the energy measurement in the calorimeters. The strong magnetic field increases the curvature of the trajectories of the highly energetic particles created in the collision thus improving the momentum resolution.

Solenoid magnet is built of superconducting materials with the operational temperature of 4.6 K. It is composed of four layers of superconducting material inserted in aluminum. Muon detectors outside the solenoid operate in 2 T magnetic field enhanced by the 10 000 t iron yoke.

4.3 Inner tracker system

The role of inner tracking system is to provide a precise measurement of the trajectories of charged particles with $p_T > 1$ GeV and the pseudorapidity $|\eta| < 2.5$. Additionally, it allows for precise secondary vertex positions reconstruction and impact parameter determination which allows for example to b-tag a jet. The size of CMS inner tracker is 5.8 m in length with a diameter of 2.5 m. Large magnetic field of 3.8 T is provided by the surrounding solenoid and is homogeneous across the entire inner tracking system. With the design LHC luminosity, expected occupancy of inner tracking system amounts to more than 1000 particles from 20 primary interactions in each bunch crossing. This requires high granularity detectors with fast responses and low dead time. In addition the amount of material in the detector has to be kept at minimum and the radiation hardness must be taken into account which lead to the solution of building an all-silicon detector with high granularity. CMS inner tracking system has two separate parts, Pixel detector and Strip detector, both described below.

4.3.1 Pixel Detector

The pixel detector is the innermost part of the CMS, closest to the interaction point. The central part, called barrel pixel, consists of three layers located at radii of 4.4 cm, 7.3 cm and 11 cm. On each side of the barrel pixel, there are two discs at $z = 34.5$ cm and 46.5 cm. The detector covers pseudorapidity range $-2.5 < \eta < 2.5$ which is illustrated in figure 4.3. Its purpose is to provide precise three dimensional space points for charged particle tracking and vertex position determination.

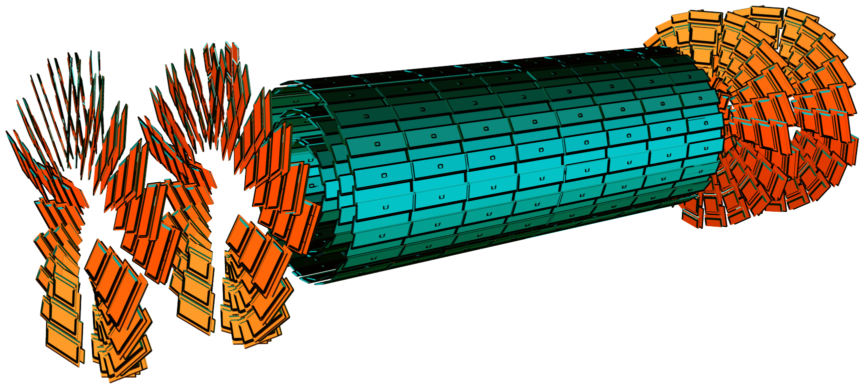

FIGURE 4.2: A drawing of the CMS pixel detector. [37]

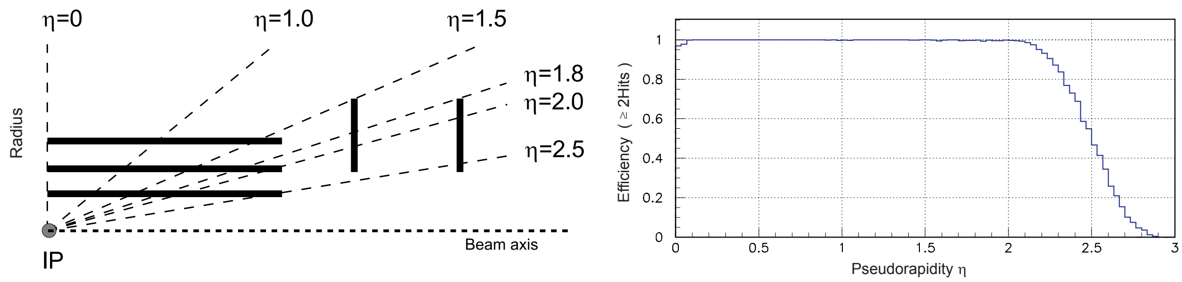

FIGURE 4.3: A sketch of CMS Pixel Detector psudorapidity range coverage(*left*) and hit efficiency as a function of pseudorapidity(*right*). [37]

Pixel detector is fully modular, consisting of rectangular modules in barrel part and quasi-triangular modules in the discs. Modules are arranged in a way to ensure measurements in at least three layers for each of the trajectories passing through the detector. Pixel size of 100×150 μm^2 results in similar resolution in z and $r - \phi$ directions. In the barrel part the resolution of $15 - 20$ μm is achieved due to charge sharing. Electrons inside the silicon shift under Lorentz force which is used in the reconstruction to determine the correct hit position. Detailed measurement of the Lorentz angle is described in the Appendix A. Pixel detector consists of 66 million pixels in total with 48 million being in the barrel pixel and 18 million in the forward. The closeness to the interaction point implies high track occupancy and necessity for radiation resistant materials.

The readout of the pixel detector goes through read-out chips (ROC) to which each pixel is bump bonded and read out individually. There are around 16000 ROCs in the detector. Each ROC consists of 52×80 pixels. Only pixels with signal above certain threshold are read out which can be tuned manually for each pixel. The average noise level in the detector is around 170 electrons at T= -10°C. The information for each event is stored in a temporary buffer awaiting the signal from the Level-1 trigger in order to be read-out. Data is read out serially, with packets containing all hits corresponding to a single trigger. Each pixel hit uses six values, five to encode pixel position, and sixth value is the analog signal charge. ROC header is added at the beginning of each ROC sequence in order to make ROC hit-association possible. Signal is than digitized and sent to central data acquisition for further processing. Various other systems are installed in order to monitor and adjust the temperature, humidity, voltages, etc.

With the design LHC luminosity, there are more than 1000 particles hitting the detector in every bunch-crossing. Very small pixel size results in the occupancy for each pixel of the order 10^{-4}. The Pixel detector has been operational for several years and shows very little drop in performance due to irradiation. The plan is to keep the present detector during the Run 2, until 2017, and than replace it with new, four-layer pixel detector which is currently being built.

4.3.2 Strip detector

The silicon strip tracker is built in layers around Pixel detector where track particle flux is lower and a lower granularity detector can be used instead. The detector is built of strips in which a passing charged particle induces current. This resulting current is than transferred to silicon detectors connected to the wires. The barrel section of the strip detector consists of four layers in the inner part (TIB) and 6 layer in the outer part

(TOB). In the forward regions there are three tracker inner discs (TID) on each side of the barrel and 9 layers in the tracker endcap (TEC).

Some strips are built in double layers tilted against each other by an angle of 100 mrad to precisely measure the position of both $r\phi$ and rz directions. The pitch size between strips varies from 80 μm in the TIB to 184 μm in TOB and TEC. With the increasing distance from the interaction point, both strip pitch and strip length increase and sensor thickness becomes larger hence affecting the resolution.

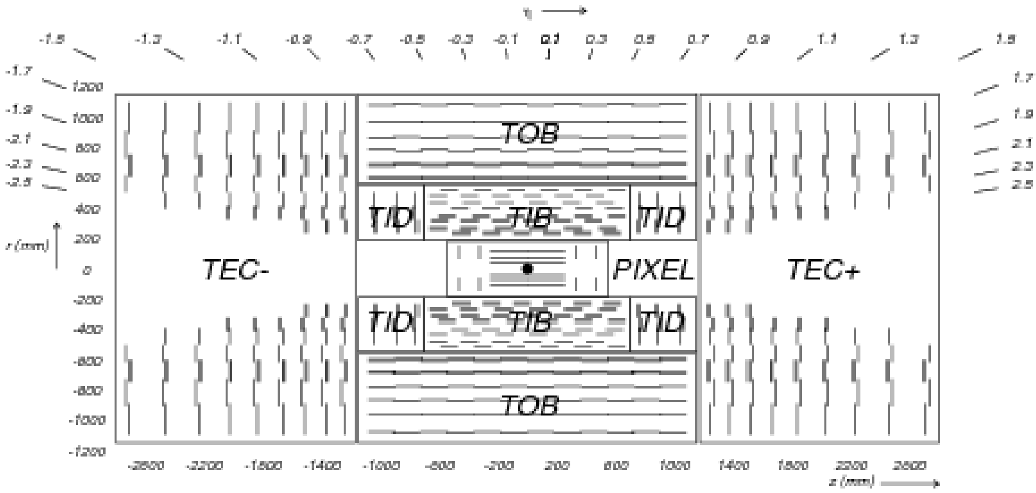

FIGURE 4.4: A drawing of the CMS strip detector. [37]

4.4 The electromagnetic calorimeter

The electromagnetic calorimeter (ECAL) has the role of precisely measuring electrons and photons. It is built from lead tungstate ($PbWO_4$), a material with very high density (8.28 g/cm^3) and a small Moliere radius (0.89 cm) which is a scale characteristic of transverse dimension of the fully contained electromagnetic showers. The scintillation light emitted within a single bunch crossing of 25 ns is about 80% of the total light which means the response time of the detector is very small that represents a large advantage of this material. The calorimeters is built of 61 200 crystals in the barrel region and 14 670 crystals in the endcaps. Each crystal has a size of 22×22 mm^2 in the front, 26×26 mm^2 at the back side and length on 23 cm in the barrel region. In the endcaps, the size of the crystals varies from 28.62 × 28.62 in the front to 30 × 30 mm^2 in the back with a length of 22 cm. The whole systems covers the range $|\eta| < 3$.

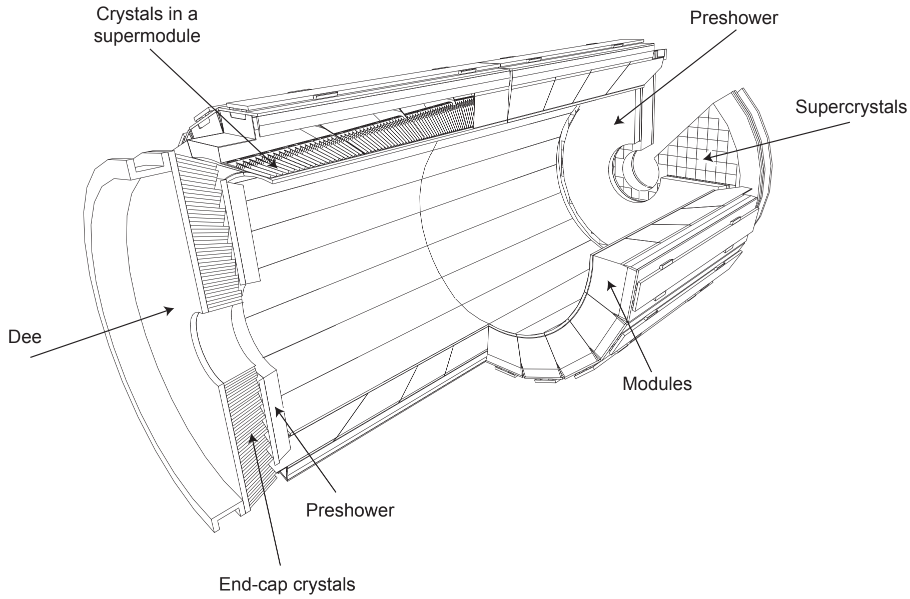

FIGURE 4.5: A drawing of the CMS electromagnetic calorimeter. [37]

Operation temperature of the detector is 18°C at which ∼4.5 photoelectrons are collected per MeV of deposited energy. The blue-green scintillation light is measured by the avalanche photodiodes in the barrel and vacuum phototriodes in the endcaps.

The ECAL energy resolution is affected by three uncorrelated sources and can be described by the relation 4.3. Parameters a, b and c are determined from the test beam. The stochastic term a is very low for the lead tungstate crystals ($a = 2.83 \pm 0.3\%$), which means that showers are mostly contained within the crystals. The noise term b is determined from the electronics and amounts to $b = 124$ MeV. The last term c is the constant term which limits the ECAL accuracy at high energies.

$$\left(\frac{\sigma_E}{E}\right)^2 = \left(\frac{a}{\sqrt{E}}\right)^2 + \left(\frac{b}{E}\right)^2 + c^2 \tag{4.3}$$

4.5 The hadronic calorimeter

The hadronic calorimeter (HCAL) is used to measure energies of hadron particles such as pions, kaons, protons, neutrons etc. Barrel and endcap hadronic calorimeters cover the pseudorapidity rande to $|\eta| = 3$. Since the absorber in the transverse direction thickness is only 5.82 interaction lengths, additional layer was placed outside the solenoid and is called HO. HCAL is a sampling calorimeter which consists of layers of brass and plastic scintillator layers. Showers are produced mostly in brass and are detected in the scintillator and reemitted in the narrow wavelength range in which photodetectors operate. In the endcap region, steel and quartz are used because of their higher radiation hardness. There is an additional part of the detector placed 11.2 meters from the interaction point on both sides called forward HCAL which extends the coverage to $|\eta| = 5.2$. Large HCAL coverage and good energy measurement are very important for jet reconstruction as well as for missing transverse energy determination.

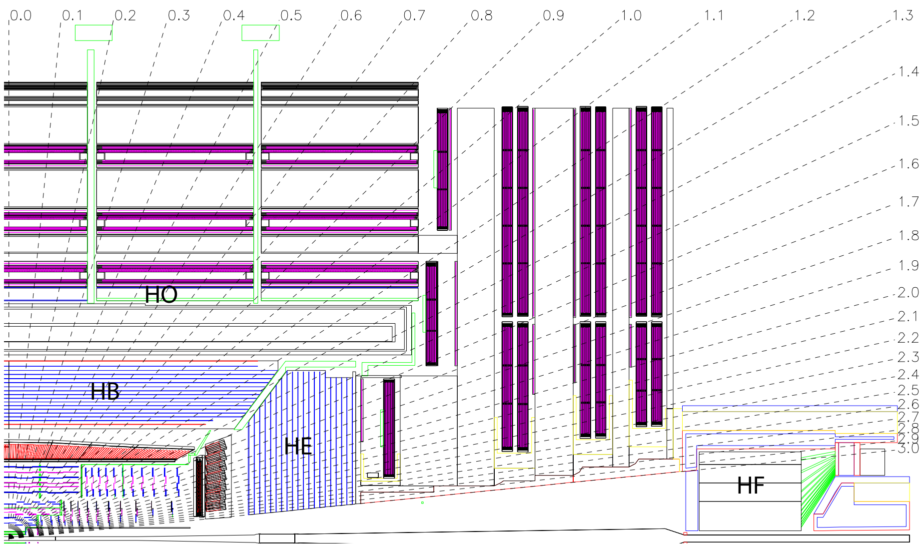

FIGURE 4.6: A drawing of the CMS Hadronic Calorimeter. [37]

4.6 The muon chambers

Muons are the only particles that can pass the calorimeters and the solenoid. Their charge and momentum is measured also in the outer part of the detector by the muon chambers. There are three different types of the gaseous detectors used in the muon system, Drift tubes (DT), Resistive Plate Chambers (RPC) and Cathode Strip Chambers (CSC). Drift tubes are used in the barrel region where muon rate is relatively low and covers pseudorapidity range of $|\eta| < 1.2$. The signal in Drift tubes is generated when a particle ionizes the gas inside the tube and the charge is collected by wires which are at high voltages. Cathode Strip Chambers are used in the endcap region where muon rate is much higher and magnetic field is not uniform. These are multi-wire proportional chambers with anodes that collect charge from the gas ionization. Resistive Plate Chambers are placed both in barrel and endcap region. These detectors are designed as two parallel plates which create a uniform electric field in the gas between them. The electrodes on the plates are highly resistive so when charged particle passes, it causes an electron avalanche which passes through the plates and is collected by the external metallic strips. Their time resolution is of the order $\sim$1 ns which makes RPCs a good choice for triggering although their spatial resolution is not so good.

Large magnetic field enables even for high p_T muons to be measured with a reasonable cell size in the muon chambers. The limiting factor for a good resolution of low p_T muons is multiple scattering, and for high p_T muons the chamber resolution. The momentum resolution as a function of muon p_T is shown in Figure 4.8 for both muon chambers and inner tracking as well as the combined result.

4.7 The trigger

The design rate of the proton collisions at the LHC is 40 MHz, although during Run 1 data taking period, the rate was 20 MHz which corresponds to 50 ns bunch spacing. Data

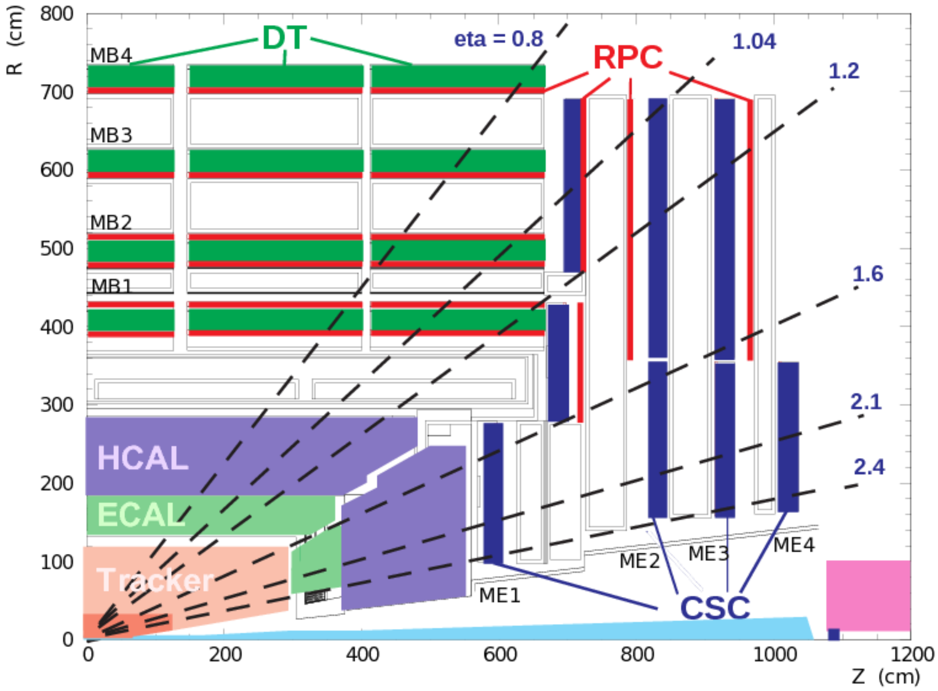

FIGURE 4.7: A drawing of the CMS muon chambers which consist of three different types of the detectors: Drift tubes, Cathode Strip Chambers and Resistive Plate chambers. [37]

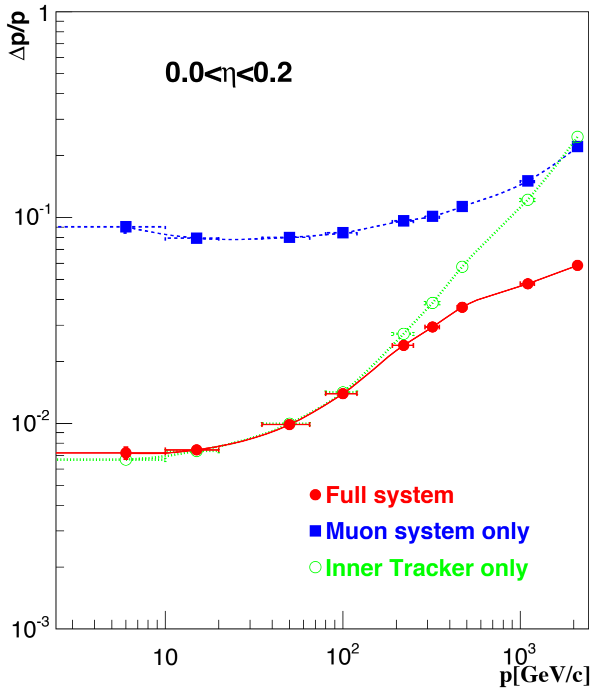

FIGURE 4.8: Muon resolution measurements for tracker, muon chambers and combined [37]

collected in the same bunch crossing is called an event. Since there are huge amounts of data coming from the subdetectors, it is necessary to apply some selections which can reduce the rate to about 100 events per second. This is done by two level triggering system, the first one called Level 1 (L1) trigger and the second one called High Level Trigger (HLT). L1 trigger uses a special custom made electronics designed to reduce the output rate from 40 MHz to 100 kHz. Events which pass some loose criteria are than passed to the HLT. The L1 trigger uses the information from calorimeters and muon chambers to take the decision whether the event should be accepted or rejected usually searching for the presence of muons, jets above certain p_T, or looking at the total amount of E_T and E_T^{miss}. The time needed to send the signals to the electronics, run the L1 selection and send the information back to the subdetectors in 3.2 μs. If the L1 trigger accepts the event, that is stored in the readout buffers where partial reconstruction takes place and the event is than processed by the HLT, which is a software farm that reduces the number of events to about 100 per second. The schematic of the trigger system is shown in figure 4.9.

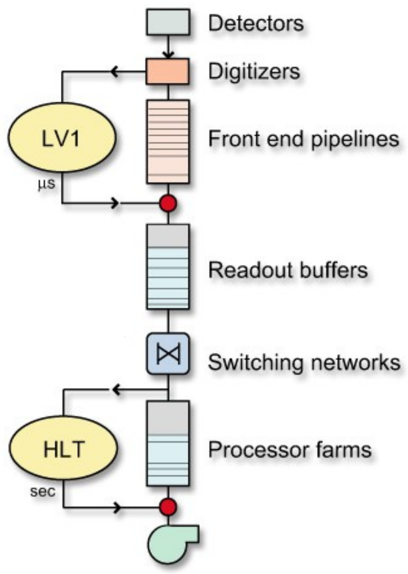

FIGURE 4.9: A schematic of CMS Trigger System. [37]

4.8 Luminosity measurement

Accurate and precise luminosity measurement is essential for physics analyses. CMS measurement is based either on the activity in the forward hadronic calorimeter (HF) or on the number of clusters in the pixel detector. The forward calorimeter is placed in the high pseudorapidity region, covering range $3 < |\eta| < 5$. The measurement relies on the fraction of nonempty calorimeter towers to estimate the number of interactions. The uncertainty to this measurement comes from the nonlinear response of the HF to luminosity and the occurrence of the afterglow, the effect when the energy deposits created in a given bunch crossing produce a signal in subsequent bunch crossings.

Luminosity measurement with the pixel detector is described in detail in [43, 44]. This method relies on the effective cross section measurement for pixel clusters determined with Van der Meer scan. This scan determines the shape and size of the interaction region by moving the beams across each other in transverse plane thus measuring the maximum available collision rate. The value of this cross section is then used to determine integrated luminosity for each lumi-section (23.3 seconds). This approach is not suitable for online luminosity measurements as pixel bias voltage is not turned on until the stable beams are declared and the data is not available if the central data acquisition system is busy. On the other hand, in the offline analysis this is not a problem as the data recorded without the pixel detector is discarded anyway. The total luminosity delivered in 2012 was around 24 fb^{-1} while the luminosity recorded by the CMS was around 22 fb^{-1}. Ideally these two numbers would be the same, but due to the downtime of data acquisition or some of the subsystems, some of the delivered luminosity is not recorded.

Chapter 5

Physics objects definitions

The CMS detector is designed to efficiently reconstruct and identify interesting physics objects. The reconstruction procedure which takes as input the signals from all subdetectors and combines them to get physics objects is called *particle flow* [45]. This algorithm classifies all the objects into one of the following categories: charged hadrons, neutral hadrons, photons, electrons and muons. These are built from reconstructed tracks in the inner tracking system, energy deposits in the calorimeters and signals in the muon chambers, which are all combined to create a global event description. Additionally, a set of requirements is imposed on both input signals and reconstructed object in order to minimize the misidentification, e.g wrongly identifying electron as a jet.

The following sections show electron and muon reconstruction procedures and identification criteria. Jet reconstruction procedure is then described together with necessary jet corrections and b-tagging algorithms. After the reconstruction of all other objects, missing transverse energy is computed as the imbalance of the vectorial sum of traverse momentum of all reconstructed particles.

5.1 Electrons

Electrons in CMS are detected as a tracks in tracking system and an energy deposit in the electromagnetic calorimeter. Two different algorithms are used for electron reconstruction, *tracker driven* seeding which is more suitable for low p_T electrons and electrons inside jets and *ECAL driven* seeding optimized for high p_T isolated electrons. Both approaches take electromagnetic crystals with deposited energy and join them into *clusters*. This process begins by identifying the cryistal with the highest energy deposit which becomes the seed for the cluster. An electron passing through the detector bends due to the magnetic field and interacts with the detector material emitting *bremsstrahlung* photons. ECAL energy deposits from these photons are spread in ϕ direction in a very narrow η range and combined with the existing cluster forming a *supercluster*. Trajectories are reconstructed using modeling of electron energy loss in the detector material and fitted with a Gaussian Sum Filter (GSF) [46].

The two approaches differ in the way they match ECAL superclusters and reconstructed tracks. Tracker driven algorithms use track from the tracking system and try to match it with the supercluster in the ECAL, while ECAL driven algorithms start from the superclusters. Each electron candidate has to pass various quality criteria in order to maximize the probability of identifying the electron coming from the hard interaction, and reject electrons from jets or conversions. These selection criteria can be divided into three categories: identification, isolation and conversion rejection. Details on electron reconstruction and performance can be found in [47].

Electron identification

The electron identification procedure first focuses on good matching between reconstructed track and supercluster, by imposing cuts on spatial distance $\Delta\eta$ and $\Delta\phi$ between the two. These variables are computed as absolute η and ϕ distance between the supercluster and electron track extrapolated to the ECAL surface. Additionally, a cut is imposed on

$\sigma_{i\eta i\eta}$ which is a measure of a shower shape spread in η direction. This variable discriminates between energy deposits coming from electrons and photons, which are narrow, and jets, which are wide. Shower shape is defined as:

$$\sigma_{i\eta i\eta} = \sqrt{\frac{\sum_i^{5\times5} w_i(\eta_i - \eta_{seed})^2 \times \Delta\eta_{xtal}^2}{\sum_i^{5\times5}}} \tag{5.1}$$

where i runs over all crystals in 5×5 block around the supercluster seed, $\eta_i - \eta_{seed}$ is the distance in number of crystals in η direction between i-th crystal in supercluster and the seed crystal and $\Delta\eta_{xtal}$ is the average width of a single crystal. Each crystal is given a weight defined as $w_i = max(0, 4.7 + ln(E_i/E_{5\times5}))$, where E_i is a single crystal energy, and $E_{5\times5}$ is the sum of energy deposits inside a 5×5 crystal block. Additional cut on the ratio between the energy deposits in the hadronic and electromagnetic calorimeter for electrons is used to discard the electron candidates with significant hadron activity.

Electrons coming from photon conversions are rejected by requiring a hit in every layer of the inner tracking system. Additionally, for each electron track a fit is performed trying to combine it with another electron track under the hypothesis that both electrons originate from a converted photon. Electron is selected only if this probability is sufficiently small. Electron compatibility with the primary vertex is estimated by looking at the impact parameters in both xy and z planes. Due to the gap in the electromagnetic calorimeter in $1.4442 < |\eta| < 1.566$, all electrons which have a supercluster position reconstructed in this range are rejected. A full list of identification criteria is summarized in Table 5.1.

5.2 Muons

Muons in CMS are reconstructed by combining a reconstructed track inside the tracker(*tracker track*) and a track in muon chambers (*standalone muon track*). Individual track segments in the muon chambers are fitted using a Kalman filter technique [48] in order to obtain

TABLE 5.1: Summary of electron identification criteria used in this analysis.

Variable	Barrel	Endcap
$\Delta\eta <$	0.004	0.005
$\Delta\phi <$	0.03	0.02
$\sigma_{i\eta i\eta} <$	0.01	0.03
$H/E <$	0.12	0.10
$d_{xy} <$	0.02 cm	0.02 cm
$d_z <$	0.1 cm	0.1 cm
$(1/E - 1/p) <$	0.05	0.05
Missing hits	0	1
Vertex Fit Probability	10^{-6}	10^{-6}

a standalone muon track. As for electrons, two approaches are used for combining track from tracker and standalone track.

The global muon reconstruction approach uses a standalone muon track in the muon chambers and tries to find a matching tracker track by combining parameters of the two tracks by projecting it to the common surface. This *outside-in* approach uses Kalman fitter technique to combine these two objects in an object called *global muon.* Muon momentum is then determined from this global muon track using all available systems which shows improved precision in comparison to other approaches.

The second approach for muon reconstruction is *tracker muon reconstruction* which starts from tracks inside the tracker with $p_T > 0.5$ GeV/c and total momentum $p > 2.5$ GeV/c as potential muon candidates. Extrapolation is than performed to the muon chambers taking into account the magnetic field, Coulomb scattering in the material and other energy losses. *Tracker moun* is found if at least one muon segment matches the extrapolated track. The efficiency of the *Tracker muon* reconstruction is higher for low energy muons than the efficiency for the global muons, because only a single muon segment in the muon chambers is required. For high energy muons where there are more segments inside muon chambers, the *global muon* algorithm is designed to have high efficiency. Detailed muon reconstruction procedure is shown in [49].

Muon identification

In this analysis *particle flow* muon identification selection is applied to the *global muons*. A selection is applied in order to minimize misidentification of charged hadrons as muons, maximize the efficiency of muon identification inside jets and ensure good momentum measurement. Muons used in the analysis have $|\eta| < 2.1$ and transverse momentum $p_T > 30$ GeV with more than 5 hits in the inner tracker system and at least one hit in pixel detector. At least one good muon chamber hit is required and the *global muon* track fit is required to have $\chi^2/ndof < 10$. At least two segments in two different muon stations should be matched to a track in order to suppress muons from in-flight decays. Cosmic muons are rejected by applying cuts on the impact parameter with respect to the primary vertex, $|d_{xy}|$ <0.2 cm and $|d_z| < 0.5$ cm. Muon identification criteria are summarized in Table 5.2.

TABLE 5.2: A summary of muon identification criteria.

Variable	Requirement
number of pixel hits >	0
number of inner tracker hits >	5
$\chi^2/ndof$ <	10
number of muon hits >	0
chambers with matched segments >	1
d_{xy} <	0.2 cm
d_z <	0.5 cm

5.3 Lepton isolation

Leptons from W decays are in general expected to be well isolated from other particles in the final state. The degree of isolation is calculated using *particle flow* approach by summing the transverse momenta contributions of particles around the lepton inside a specific cone. All charged particles as well as photons and neutral hadrons are considered if they have p_T >0.5 GeV. The cone used for determination of energy deposits is defined as $\Delta R = \sqrt{\Delta\phi^2 + \Delta\eta^2}$ around the lepton axis and isolation measure is defined as:

$$I_{PF}^{rel} = \frac{\sum p_T^{charged} + max(0, \sum E_T^{\gamma} + \sum E_T^{neutral} - 0.5 \sum E_T^{PU})}{p_T^l} \tag{5.2}$$

where $\sum p_T^{charged}$ is the sum of the momenta of charged hadrons and E_T^{γ} and $E_T^{neutral}$ are the sums of photon and neutral hadron momenta. E_T^{PU} is the sum of the pile-up transverse energies from charged particles and is calculated as a sum of track transverse momenta not coming from the primary vertex inside the isolation cone. This is multiplied by the factor of 0.5, which corresponds approximately to the ratio of neutral to charged hadron production in the hadronization process of pile-up interactions. Selected muons are required to pass isolation cut $I_{rel}^{PF} < 0.12$. On the other hand, if there is a requirement that there be no leptons in the event, the isolation cut is $I_{PF}^{rel} < 0.2$. Electron isolation is computed in the very same way with cut of $I_{rel}^{PF} < 0.1$ for selected electrons and $I_{rel}^{PF} < 0.15$ for vetoed additional electrons.

5.4 Jets

In high energy physics, a jet is a collimated group of hadrons which emerges as a result of quark or gluon fragmentation and hadronization process. Hadrons reconstructed in a particle detector need to be combined in order to form a jet and give information about the initial parton. A set of rules has to be created which define how to group particles and how to assign momentum to the jet. Usually this is done by summing the four-momentum of each particle in a jet.

5.4.1 Jet algorithms

Jet algorithms take into account the distance between particles and define rules to determine which particle belongs to what jet. The same jet algorithms should be applicable to both, experimental data and theoretical calculation. Other important properties of jet algorithms are *infrared safety* and *collinear safety* which means if an event is modified by addition of soft emission of collinear splitting, the final number of hard jets will remain unchanged. These two properties together are called *IRC safety*. IRC unsafe jet algorithms may break the cancellation of divergences by yielding one set of jets for tree-level splitting while loop diagrams lead to another, as shown if figure 5.1, giving infinite cross-sections in the full calculations. Jet definitions, jet relation to partons and an overview of different jet algorithms are summarized in [50].

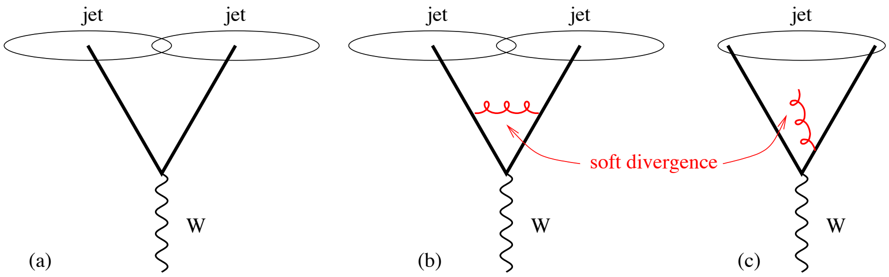

FIGURE 5.1: Configuration showing IC unsafety with W boson and two partons. Adding a soft gluon causes two jets to be reconstructed as one. [50]

There are two types of jet algorithms which are most commonly used: *cone algorithms* and *sequential recombination algorithms*. In the case of *cone algorithms*, a jet is defined as a set of particles inside a stable cone around their center of mass. Most popular cone algorithm is *iterative cones* (IC) where a seed particle is chosen and momenta of all particles around that initial particle inside a cone of radius R are summed. After adding each new particle to the sum, the direction of the new sum is taken as a seed direction, and the procedure repeats until the direction of the resulting cone is stable. Particles inside the cone are than removed from the list of available particles and the procedure repeats. This approach is not IRC safe given that nearly collinear splitting of the hardest particle in the event can be reconstructed as two jets. In that case, a less energetic, particle, pointing in another direction, can become the hardest particle in the event, yielding different set of jets. Cone algorithms can be IRC safe using a *seedless cone* (SC) algorithm where all stable cone solutions are identified at once. However this approach is very time consuming even for small number of particles and thus very impractical to use.

In the *sequential recombination algorithms* at hadron colliders two longitudinally invariant distances are introduced: d_{ij} which is the distance between each pair of particles and d_{iB} which is the particle-beam distance. These distances are defined as:

$$d_{ij} = min(k_{T,i}^{2p}, k_{T,j}^{2p}) \frac{\Delta R_{ij}^2}{R^2} \tag{5.3}$$

$$d_{iB} = k_{T,i}^{2p} \tag{5.4}$$

where ΔR_{ij} denotes the distance in the $\eta - \phi$ plane and is computed as

$$\Delta R_{ij}^2 = (\eta_i - \eta_j)^2 + (\phi_i - \phi_j)^2.$$

k_T is transverse momentum of the particle, R is an angular cut-off similar to the one in *cone algorithms*, and p defines which particles are clustered first and is described below. Both R and p are free parameters of the algorithm. The algorithm is applied using the following approach: distances d_{ij} between each pair of particles, and d_iB for each particle are computed and minimal value is found. If d_{ij} is the smallest value, particles i and j are combined, and treated as a new particle in the next iteration of the algorithm. In case of d_{iB} being the smallest, i is declared to be the final jet and is removed from the list of particles. The procedure continues until there are no more particles in the list.

The parameter p defines which particles are clustered first thus defining the type of algorithm. The k_T algorithm uses $p = 1$, clustering soft particles first. This results in irregularly shaped jets, as shown in figure 5.2, which are sensitive to radiation in the event and difficult to calibrate. The *Cambridge-Aachen* algorithm (CA) uses $p = 0$ thus relying only on angular distribution of the input particles. This approach is particularly useful for jet substructure analysis and is less sensitive to radiation. The algorithm used in this analysis is anti-k_T algorithm where $p = -1$ clusterizing the hardest particles first [51]. Anti-k_T is an IRC safe algorithm and results with jets that are circular in shape because they are not affected by the softer components of the jet.

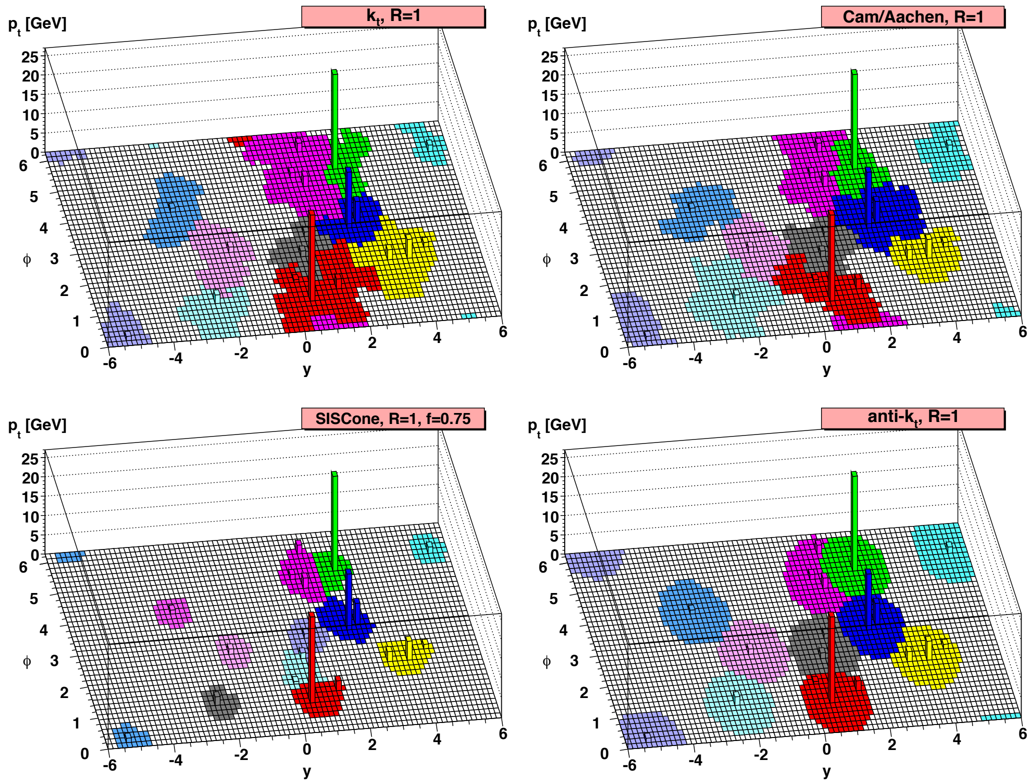

FIGURE 5.2: Clustering same set of reconstructed particles into jets using different jet algorithms. [50]

5.4.2 Jet corrections

Various measurements during the commissioning phase of the CMS detector showed that measured jet energy at detector level in general doesn't correspond to the energy of the originating particle. A jet calibration procedure is introduced to compensate for the nonlinear response of the calorimeters. This is done using a factorized approach where corrections on each level of correction are determined separately as described in [52]. The final corrected jet momentum is obtained from measured uncorrected transverse momentum p^{raw} according to:

$$p^{corr} = C_{res}(p''_T, \eta) \times C_{abs}(p'_T) \times C_{rel}(\eta) \times C_{offset}(p_T^{raw}, \eta) \times p^{raw} \tag{5.5}$$

Correction factors correspond to the following:

- The offset correction C_{offset} compensates for energy contributions arising from pile-up events or instrumental noise. The offset is determined in dependence of pseudorapidity and jet area p_T density which is described in detail in [53].
- The relative correction C_{rel} aims at flattening the jet energy scale in pseudorapidity. The correction is determined from simulated QCD multijet events, adjusting the jet scale in all η regions to one of the jets in $|\eta| < 1.3$ without changing the absolute scale.
- Absolute correction C_{abs} flattens the jet scale in p_T. This correction is also determined from QCD multijet events as the inverse of average response at some fixed generated jet transverse momentum.
- The residual correction C_{res} is applied only to data in order to account for possible residual differences between data and simulation after applying absolute and relative corrections. These corrections are derived using events with momentum balance in the transverse plane, like dijet events or Z/γ + jet events.

C_{offset} and calibration factors C_{rel} and C_{abs} are applied to both data and simulation and C_{res} is applied only to data. Corrections are applied sequentially, in a fixed order such that $p'_T = C_{offset} \times C_{rel}(\eta) \times p^{raw}$, and $p''_T = C_{abs}(p'_T) \times C_{rel}(\eta) \times C_{offset}(p_T^{raw}, \eta) \times p^{raw}$. Correction factors used in this analysis can be found in [54].

The total jet correction for a fixed jet p_T as a function of pseudorapidity is shown in figure 5.3. The total jet correction for a fixed jet pseudorapidity as a function of transverse momentum is shown in figure 5.4. It is shown that jet energy correction factors for PF jets and JPT jets are relatively stable between 1 and 1.2 across wide p_T and η range. The total uncertainties to the jet energy corrections as a function of jet transverse momentum are shown in figure 5.5.

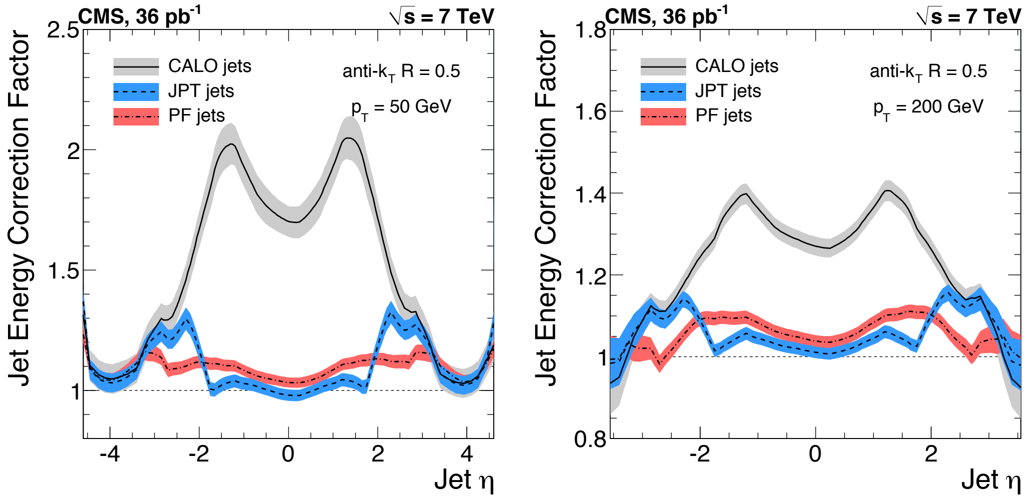

FIGURE 5.3: Total jet energy correction as a function of pseudorapidity of two different jet p_T values. Corrections are shown for all three types of jets, calo, JPT and PF jets. Bands indicate corresponding uncertainty.[52]

5.4.3 Jet identification

This analysis uses the anti-k_T algorithm with cone size $R = 0.5$. Jet algorithm implementation is done in the FASTJET package [55]. Depending on which signals the algorithm is applied to, there are different kinds of jets: calo jets (calorimeter deposits used), jet-plus-track jets (calorimeter deposits complemented with tracker information) and most widely used *particle flow* jets (PF). These jets are clustered from particle flow objects identified with the PF algorithm, thus using the information not only from HCAL, but also from the tracking system and ECAL, which result in much better resolution. Only the neutral fraction of jets is measured with HCAL alone which makes about 15% of the total jet composition. PF jets show excellent performance and are the default jets for most CMS analyses. Pile-up information is also taken into account by removing charged hadrons originating from pile-up vertices from the list of particles available for the jet clusterization. This procedure is called *charged hadron subtraction*. Some additional cuts to the jet composition are applied in order to ensure good jet identification. All jet identification criteria are summarized in the table 5.3.

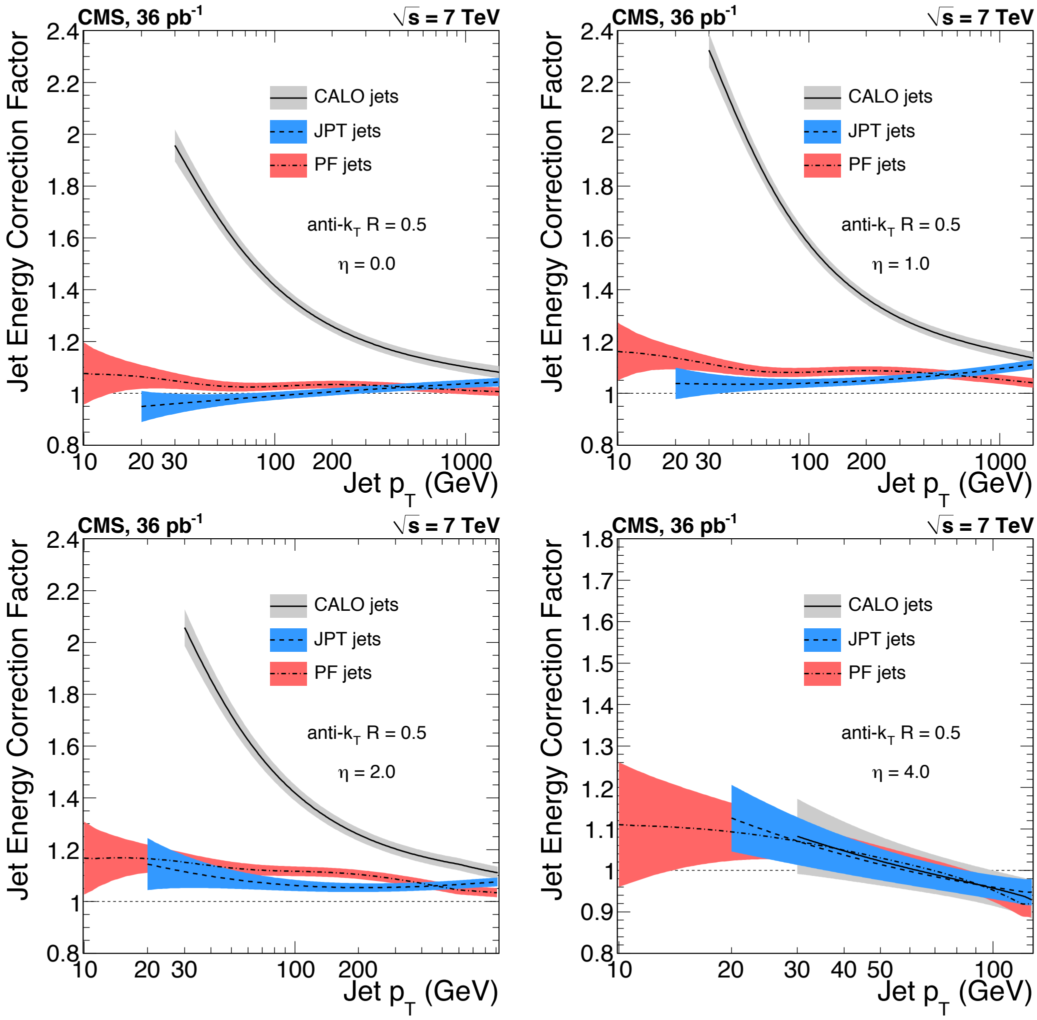

FIGURE 5.4: Total jet energy correction as a function of transverse momentum for four different η values. Corrections are shown for all three types of jets, calo, JPT and PF jets. Bands indicate corresponding uncertainty.[52]

5.4.4 Jets from b quarks

The unique properties of the bottom quark can be used to identify hadronic jets originating from b quarks, which are usually referred to as b-jets. The long lifetime of B hadrons is a consequence of weak force decay which results in the displacement of their decay vertices by few millimeters at the LHC energies. These hadrons have relatively large masses and daughter particles with hard momentum spectra. The process of b-jet identification is called $b - tagging$. It takes one or more variables and produces a single discriminant

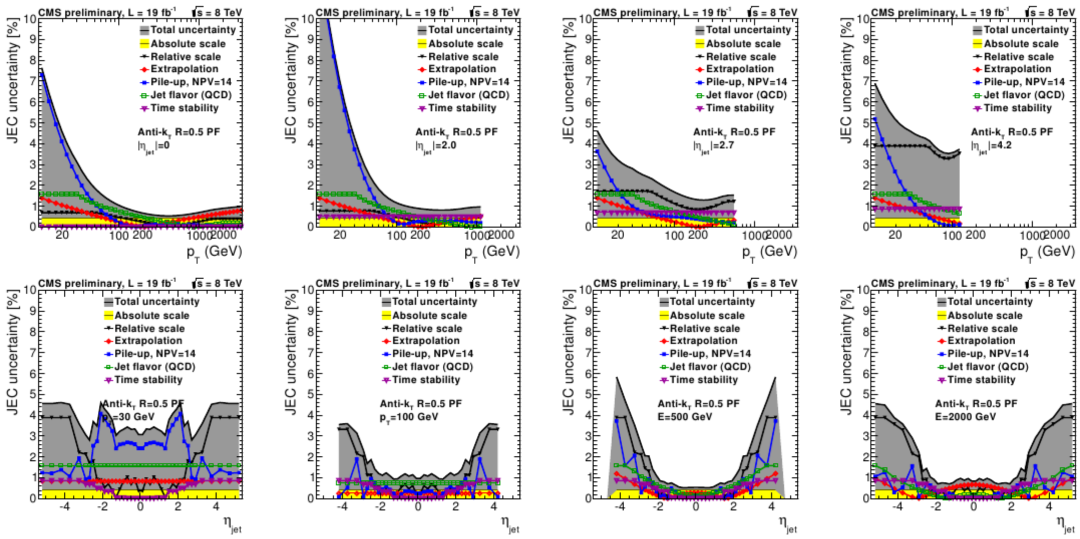

FIGURE 5.5: Total jet uncertainty and contribution from different sources in jet p_T and η [54]

TABLE 5.3: A summary of jet identification criteria.

Variable	Requirement
Neutral hadron fraction	< 0.99
Neutral EM fraction	< 0.99
Number of Constituents	> 1
Additional cuts for $\|\eta\| < 2.4$	
Charged hadron fraction	> 0
Charged multiplicity	> 0
Charged EM fraction	< 0.99

value for each jet. This value shows how much the observed jet looks like a b-jet. There are several *b-tagging* algorithms in use at CMS which are described in detail in [56] the following were used for 2012 data:

- *Track counting*(TC) - The discriminant uses the impact parameter significance, which is calculated as the impact parameter value divided by the respective impact parameter uncertainty. Impact parameter significance values are sorted in increasing order and the second or the third lowest value is used as a discriminant. Depending on whether the second or third value is chosen, the algorithm is denoted as high efficiency or high purity.

- *Jet Probability*(JP) - This algorithm combines information from several tracks inside a jet by computing a likelihood that all tracks originate from the primary vertex.

- *Combined secondary vertex*(CSV) - This is the most efficient *b-tagging* algorithm currently used in CMS. Secondary vertex and track related informations are combined to build the CSV discriminator. It shows high efficiency even when no good secondary vertex can be reconstructed. Some of the variables used in the CSV algorithm are flight distance, vertex mass, impact parameter significance, track multiplicity at the vertex and track multiplicity in a jet. The distribution of CSV discriminator is shown in figure 5.6.

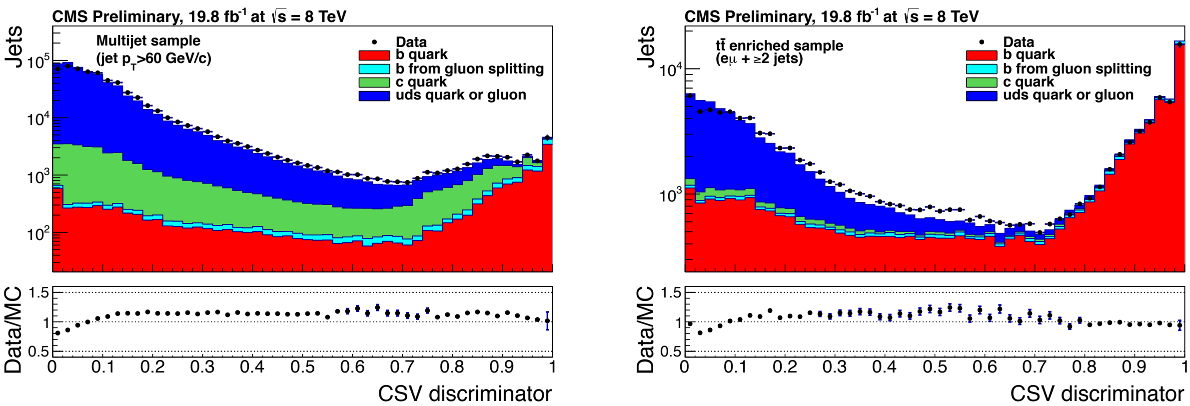

FIGURE 5.6: Combined secondary vertex discriminator for multijet QCD sample (left) and tt enriched sample(right)[57]

For each non-b-jet there is a chance that it would be identified as b-jet. Three working points are chosen based on the mistagging efficiency. For an average jet of 80 GeV, these values correspond to misidentification rates of 10%, 1% and 0.1% for loose, medium and tight working point respectively [58]. Misidentification probabilities as a function of b-jet transverse momentum for combines secondary vertex algorithm is shown in figure 5.7.

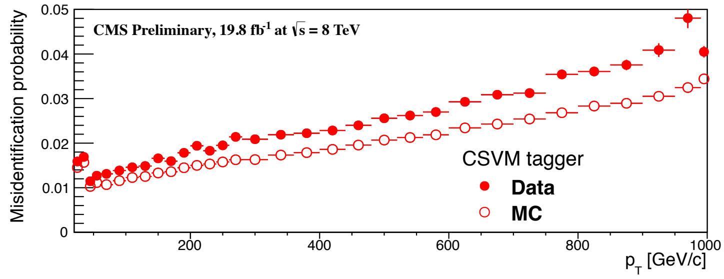

FIGURE 5.7: Combined secondary vertex misidentification probability for data and MC for medium working point.[57]

5.5 Missing transverse energy

The missing transverse momentum is the imbalance in the vectorial sum of transverse momenta of all measured particles. Missing transverse energy is the magnitude of the missing transverse momentum and is calculated as:

$$E_T^{miss} = |-\sum_i \vec{p}_i| \tag{5.6}$$

where i goes over all visible particles. Momentum conservation suggests that the imbalance could arise from weakly interacting neutral particles such as neutrinos or any other particle that doesn't interact with the detector. Measurement of the missing transverse energy relies on the good measurement of all other particles in the event and as such is very sensitive to detector resolution, particle missmeasurements, limited acceptance of the detector, cosmic-ray particles, all of which can cause artificial missing energy. There are several approaches to determine E_T^{miss}. In this analysis, the particle flow technique is used, which tries to identify each particle in the event by combining the information from all subdetectors and gives the best missing energy resolution.[59, 60] Several corrections are applied to the E_T^{miss} which correct for the possible bias in the missing energy measurement:

- Type-I correction: propagates jet energy corrections described in Section 5.4.2 to missing energy. This correction replaces the uncorrected transverse momenta of particles in a jet by the transverse momentum of a jet to which JEC were applied in the missing energy calculation.

- xy-shift correction: aims at correcting the observed missing energy ϕ modulation. The true missing energy distribution is expected not to depend on ϕ because of the rotational symmetry of collisions around the beam axis. The possible causes for such modulation include unisotropic detector response, detector misalignment or the displacement of the beam spot. The amplitude of the modulation is observed to increase with the number of pile-up interactions. This correction can thus be seen as mitigation for the pile-up effects.

Missing transverse energy, together with the reconstructed muon or electron, is used to construct W boson candidates. Transverse mass distribution particularly useful in the case of a decay into two particles, when one particle cannot be detected directly but is only indicated by missing transverse energy. If the daughter particles are massless, transverse mass is described with:

$$M_T = \sqrt{2p_T^{lepton} E_T^{miss}(1 - cos\Delta\phi)}. \tag{5.7}$$

Chapter 6

Event selection and background estimation

This chapter describes the event selection criteria used to identify the process $pp \rightarrow W + bb + X$. The selection is focused on the leptonic decay modes of W boson, thus requiring the presence of an isolated muon or electron, missing energy, and two b-tagged jets. The reconstruction and identification of these objects has been described in the previous chapter. All major backgrounds are identified using simulation and are used to get the final signal yields for the cross section measurement in chapter 7. This chapter is organized as follows. The samples used in the analysis together with a short description of simulation procedures are presented in section 6.1. In order to obtain good agreement between data and simulation, certain corrections are applied to the simulation to take into account trigger and reconstruction efficiencies, pileup reweighing and b-tagging inefficiencies. The applied corrections are summarized in section 6.2. Signal selection criteria are described in section 6.3 while the estimation of the background sources is described in section 6.4.

6.1 Data and Monte Carlo samples

The data samples used in this analysis are consist of pp collisions at center of mass energy of 8 TeV collected with the CMS experiment during 2012. After performing necessary data-quality checks, 19.8fb^{-1} of data was marked as good quality for physics analysis. Selected events are required to pass one of the following triggers:

- Isolated muon with $p_T > 24$ GeV and $|\eta| < 2.1$,
- Electron with $p_T > 27$ GeV and $|\eta| < 2.1$

Simulated samples for signal and background processes were obtained using Monte Carlo methods, as a part of the official 2012 CMS production campaign. Simulated samples include W+jets, Z+jets, $t\bar{t}$, single top and WZ samples. Diboson samples were generated with Pythia event generator while W+jets, Z+jets and $t\bar{t}$ samples were produced with Madgraph and showered with Pythia.Several event generators were used to produce samples needed in the analysis:

- **Pythia** [61, 62] is a multi-purpose generator which can also simulate parton shower. Pythia is able to calculate only tree-level 1→2 and 2→2 processes while higher orders are approximated with parton shower algorithm. Parton showering in all samples uses the so called Z2 tune for modeling the underlying event [63, 64].
- **Madgraph** [65] calculates matrix elements at tree level for decays and 2→ n scatterings (with n going up to 10). Radiation of hard gluons in initial and final state is taken into account at the matrix element calculation level. A minimum p_T threshold is defined in order to avoid soft gluon emissions which cause the total cross section to be strongly scale dependent. Cross section is normalized to predictions (N)NLO from other programs, such as MCFM [66] for standard model processes.
- **aMC@NLO** [67] automates and unifies the tree-level and next-to-leading order computation tools within the MadGraph family.

- **Powheg** [68] is a package optimized for heavy quark production in hadronic collisions. The hard process is calculated at the NLO order. For fragmentation and hadronization other software is used (e.g. Pythia). Single top events were produced using this generator and showered with Pythia.

- **Tauola** [69] is a package for simulation of τ decays.

The detector response is simulated using the GEANT4 simulation package [70]. Data was analyzed using ROOT framework [71]. The list of the used samples together with the corresponding cross sections is shown in the Table 6.1.

TABLE 6.1: Samples, generators and cross sections used for normalizations for signal and background simulation considered in this analysis. All samples are normalized to the NLO cross-section calculation except the W+jets which is NNLO and $t\bar{t}$ which is normalized to the latest combined cross section measurement of ATLAS and CMS collaborations [72].

Sample	Generator	$\sigma(pb)(NLO)$
W($\rightarrow l\nu$)+jets	Madgraph + Pythia	37509 (NNLO)
W + 1 jet	Madgraph + Pythia	–
W + 2 jets	Madgraph + Pythia	–
W + 3 jets	Madgraph + Pythia	–
W + 4 jets	Madgraph + Pythia	–
W + bb	Madgraph + Pythia	377.4
Z + jets	Madgraph + Pythia	3531.9
$t\bar{t}$ semi-leptonic	Madgraph + Pythia	107.7
$t\bar{t}$ full-leptonic	Madgraph + Pythia	25.8
single t - t$-$channel	Powheg + Pythia	56.4
single t - s$-$channel	Powheg + Pythia	3.97
single t - tW$-$channel	Powheg + Pythia	11.1
single $\bar{t}$ - t$-$channel	Powheg + Pythia	30.7
single $\bar{t}$ - s$-$channel	Powheg + Pythia	1.76
single $\bar{t}$ - tW$-$channel	Powheg + Pythia	11.1
WZ	Pythia	33.6
WW	Pythia	56.0

Signal events are simulated in exclusive W+1,2,3,4 jets samples using the Madgraph event generator and showered with Pythia. These samples are generated using the five-flavour scheme with massless b-quark in the initial state. Samples are than divided into three subsamples labeled as W+b(b), W+c(c) and W+light. W+b(b) subsample is selected by the requirement that there be a generated particle starting with pdgId=±5 in one of the jets. W+c(c) samples is selected if c quark is generated in one of the jets (pdgId= ±4). Events are classified sequentially with W+b(b) events selected first. All other events are labeled as W+light jets (W+udcsg). Additionally, the analysis has been preformed using the shape from the four-flavour sample listed in the Table 6.1, which has much larger number of generated signal events. It was normalized to the five-flavour cross section .

6.2 Monte-Carlo corrections

6.2.1 Pileup

In proton-proton collisions at high beam intensities, there is a high probability that multiple interactions will happen in a single bunch crossing. These additional interactions are usually referred to as pileup interactions and contain low$-p_T$ QCD processes. The identification of such jets as well as their removal is described in detail in [73]. The total inelastic cross section at $\sqrt{s}$ =8 TeV, in the 2012 is 69 mb, so the luminosity per bunch crossing of 69 mb^{-1} results in one interaction per bunch crossing. As the instantaneous luminosity per bunch crossing was higher than the total inelastic cross section, this resulted in 21 primary interactions on average during 2012, with some bunch crossings going up to 70. Under these conditions it is important to recognize the signature from such interactions.

Simulated events have a different distribution for the number of pileup interaction with respect to data. This occurs because it was difficult to predict the exact pileup distribution in data during the generation of the simulated events. Therefore, simulated events were reweighed to match the distribution in data. For each simulated event, a weight w_{PU} is derived based on the number of pileup events provided by the generator.

Figure 6.1 shows the number of reconstructed vertices before and after the reweighing procedure for the events passing full selection described in section 6.3 in the muon channel. The agreement between data and simulation has improved after the reweighing procedure which is also visible in the ratio plot.

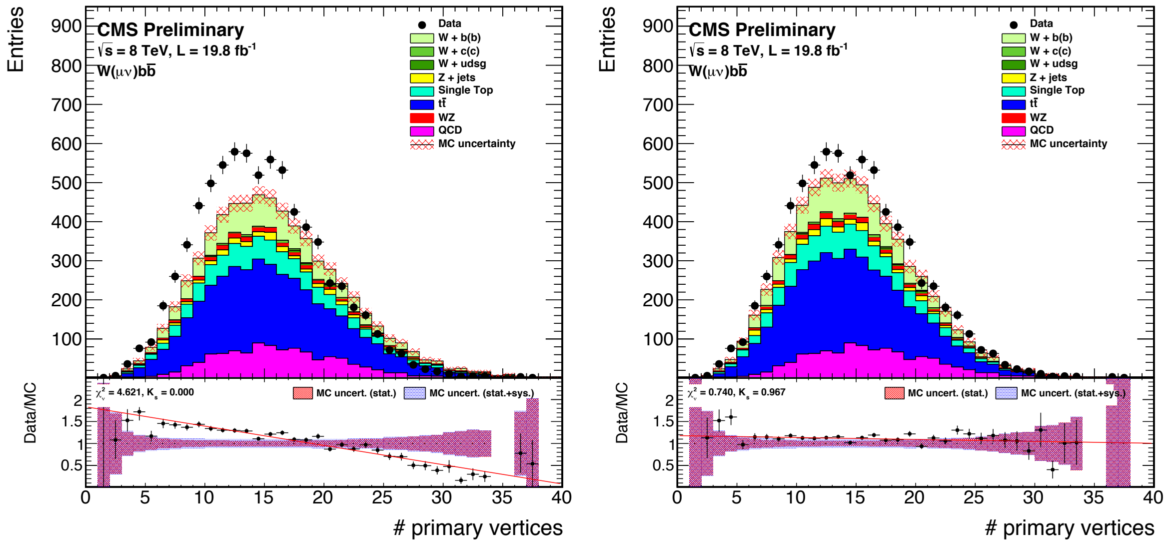

FIGURE 6.1: Number of primary vertices before (*left*) and after (*right*) the pileup reweighing procedure.

6.2.2 Lepton efficiency measurement

Events used for the cross section measurement are required to pass certain triggers in order to be selected. However, the trigger selection is not 100% efficient and the selection efficiency has to be determined. The additional steps in the analysis, like reconstruction and isolation, which introduce some inefficiencies as well. The efficiency estimation from simulation shows large systematic uncertainties due to inaccuracy in signal modeling and detector response. This was the main motivation for the development of the fully data-driven lepton efficiency estimation called *Tag and probe*. In this method well-known mass resonances, such as the Z boson, are used and the following selection criteria is applied to the decay products. Very tight selection criteria are applied on one Z boson daughter lepton (*tag*) while the looser cuts, used in the analysis, are applied on the other (*probe*) lepton. The efficiency (ϵ) for a given cut is than determined by counting the number of probe leptons that pass the cut (N_{pass}) divided by the number of all probe leptons. This number includes the probe leptons that passed and failed the cut (N_{fail}):

$$\epsilon = \frac{N_{pass}}{N_{pass} + N_{fail}} \tag{6.1}$$

As it is not possible to uniquely identify Z bosons, while performing tag and probe method, invariant mass distributions of the two leptons are used to determine N_{pass} and N_{fail}.

Signal and background are parameterized and their contributions are estimated using a maximum likelihood fit. For signal events, a convolution of Z generator shape with a Gaussian is used to take into account the detector effects, while for background parametrization, a combination of exponential function and polynomial was used.

The efficiency was measured as a function of pseudorapidity and transverse momentum of the probe. Trigger, identification and isolation criteria were used in electron and muon channels separately. Both data and Monte Carlo efficiencies were measured and their ratio was used as a scale factor applied to each event in order to match simulated lepton efficiencies to measured efficiencies in data. The muon identification and isolation efficiency for data and MC for the barrel part ($|\eta| < 0.9$) of the detector is shown in figure 6.2 while the trigger efficiency measurement is shown in figure 6.3. Similar values for the efficiencies are obtained for the other parts of the detector.

6.2.3 *b-tagging* scale factors

CMS simulations describe very well the detector performance. However, it is difficult to accurately model all parameters used in b-tagging algorithms. The procedure used to identify b-jets is described in 5.4.4 and it depends on track reconstruction efficiency, tracking resolution and other tracking related parameters. Efficiency and misidentification probabilities are functions of transverse momentum and pseudorapidity of a jet. Therefore, it is very important to determine the b-tagging efficiency from data. The obtained

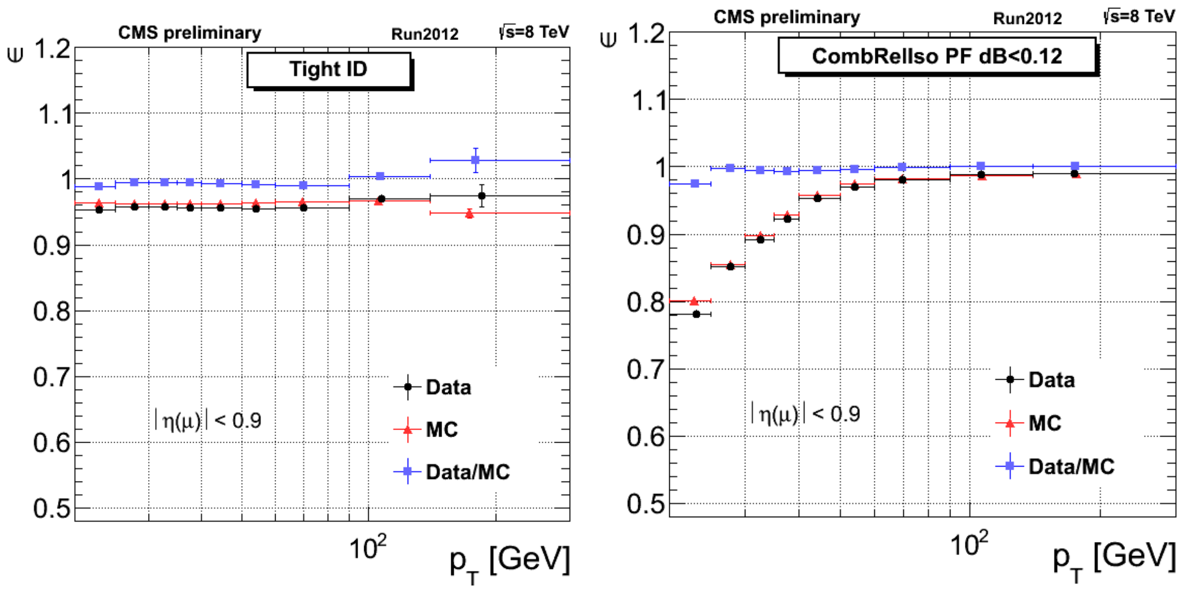

FIGURE 6.2: Muon identification (*left*) and isolation (*right*) efficiencies determined using *tag and probe* method as a function of probe p_T, for the barrel part of the detector($|\eta| < 0.9$) [74].

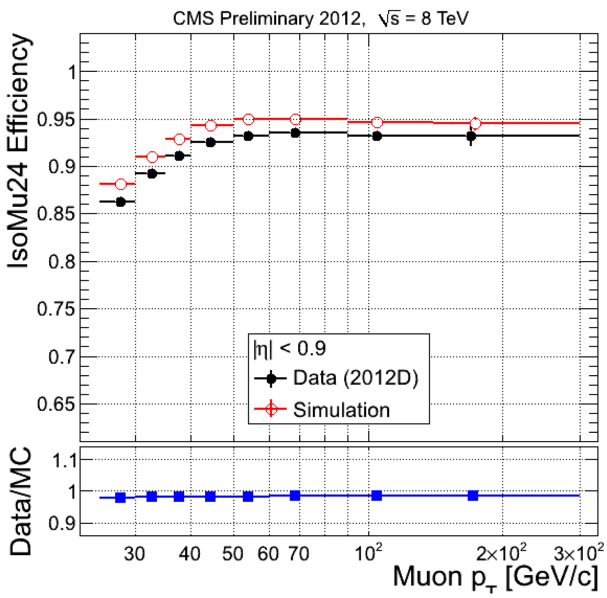

FIGURE 6.3: Efficiency for HLT muon trigger for barrel part of the detector ($|\eta| < 0.9$) determined using *tag and probe* method .

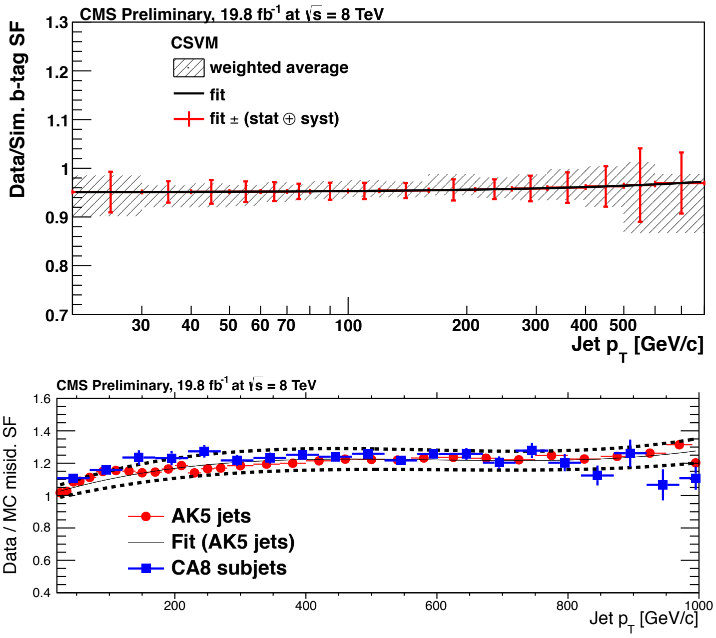

FIGURE 6.4: B-tagging (*up*) and misstag (*bottom*) scale factors. [57]

corrections are applied to simulated events as scale factors which are defined as the ratio between efficiency measured in collisions ϵ_b^{data} and efficiency from simulated events ϵ_b^{MC}:

$$SF_b = \frac{\epsilon_b^{data}}{\epsilon_b^{MC}} \tag{6.2}$$

The scale factor determination has to be performed using a b-jet enriched sample such as $t\bar{t}$ or multijets events with jet containing a muon within a $\Delta R < 0.4$ cone from the jet axis. The choice of the jet which contains a muon relies on the fact that the B hadron semileptonic branching ratio is much higher than that for other hadrons ($\sim$ 20% when including b→c→ decays) and such jets are much more likely to arise from B hadron decay. With very high muon detection efficiency at CMS, it is relatively easy to obtain a clean sample with jets containing nonisolated muons. Another efficiency measurement is performed using a $t\bar{t}$ enriched sample [57]. By combining the results from both measurements, scale factors were obtained as a function of jet p_T together with statistical and systematic uncertainty for each p_T bin. The same strategy is used to obtain misidentification rates by using the inverted cut on b-tag discriminator. The estimated scale factors as a function of jet transverse momentum are shown in figure 6.4. The usage of the scale factors depends on the number of b-tagged jets in the event. In this analysis two b-tagged jets are required and the weight for each event is derived as:

$$w(2|2) = SF_{b||light}(\text{1st jet}) \times SF_{b||light}(\text{second jet}) \tag{6.3}$$

where $w(2|2)$ is the event weight for an event with 2 jets where both jets are b-tagged. The choice between SF_b and SF_{light} depends on the flavor of the jet in the simulation. A jet is considered a b jet if there is a B hadron present among the jet constituents within a cone of 0.4 from the jet axis.

6.3 Event selection

Signal events are characterized by the presence of a W boson and two jets which have been tagged as coming from b quarks. Candidates for a W boson are identified as isolated muons or electron and significant missing energy. Jets are identified as particle flow objects clustered with anti-k_T algorithm with a cone size of 0.5. The combined secondary vertex (CSV) algorithm is then used to identify jets arising from fragmentation and hadronization of b-quarks as is explained in 5.4.4. Signal events are selected using the following requirements:

- One muon or electron with $p_T > 30$ GeV, within $|\eta| < 2.1$, which passes the trigger requirement ($p_T > 24(27)$ GeV for muons(electrons) and tight ID criteria described in 5.2, and has $I^{PF}_{rel} < 0.12$ (0.10) in case of muons (electrons).
- Exactly two jets with jet $p_T > 25$ GeV, within $|\eta| < 2.4$ passing loose ID criteria from 5.4.3 with distance between lepton and jet $\Delta R > 0.5$.
- Events containing jets with $p_T > 25$ in high pseudorapidity range $2.4 < |\eta| < 5$ are rejected.

- Events containing additional lepton with $p_T > 10$ GeV, within $|\eta| < 2.1$, tight ID and loose isolation are rejected.
- Both selected jets are required to pass tight CSV discriminator cut of 0.898.
- Transverse mass higher than 45 GeV.

Several detector level distributions are shown in figure 6.5 for the muon channel and in figure 6.6 for the electron channel obtained after applying all the correction factors described in section 6.2. It is visible that the final sample contains only around 20% of Wbb events. Therefore it is essential to understand the contributions from all major backgrounds. The estimation of the various background contributions to the signal sample is described in the following section.

6.4 Background estimation

After applying all selection cuts described in the previous section, the major backgrounds that remain are top quarks, Z+jets, W+jets, diboson and QCD multijet processes. All samples describing the signal and background processes are normalized to their corresponding cross sections as described in the section 6.1. The obtained distributions are then used as an input the fitting procedure described in the chapter 7 aimed to determining the final yields used in the cross section calculation. Each of the background contributions is described in detail below.

6.4.1 Top quark background

Production of $t\bar{t}$ pairs and single top represent a challenging background at the LHC because of their relatively large production cross sections. $t\bar{t}$ events are largely suppressed by requiring a veto to the existence of additional jets in the event. Single top background is more difficult to reduce using only topological cuts. However, its production cross-section

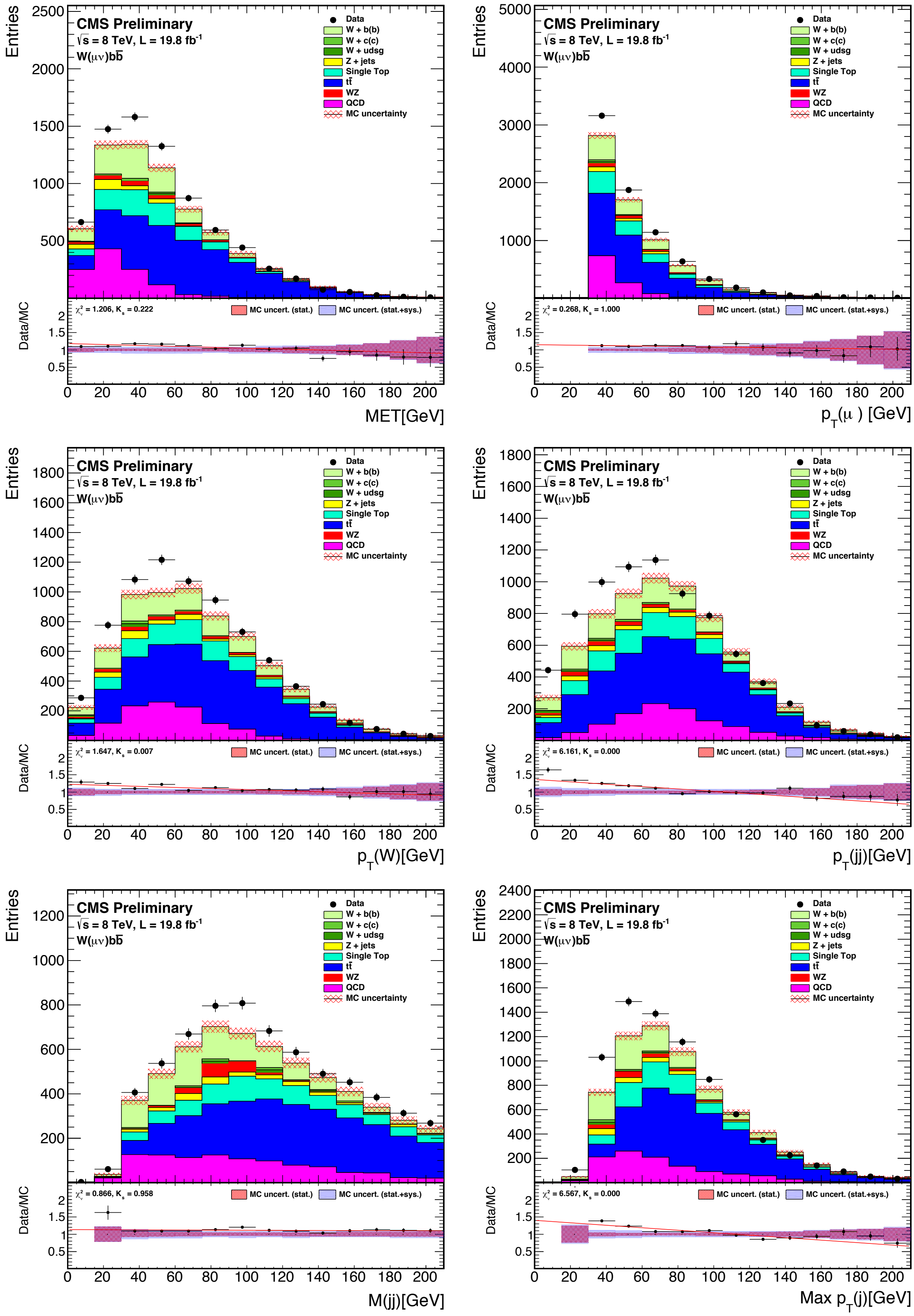

FIGURE 6.5: Various signal region distributions for the electron channel: missing energy, lepton transverse momentum, W transverse momentum, invariant mass and transverse momentum of two b jets and highest jet transverse momentum.

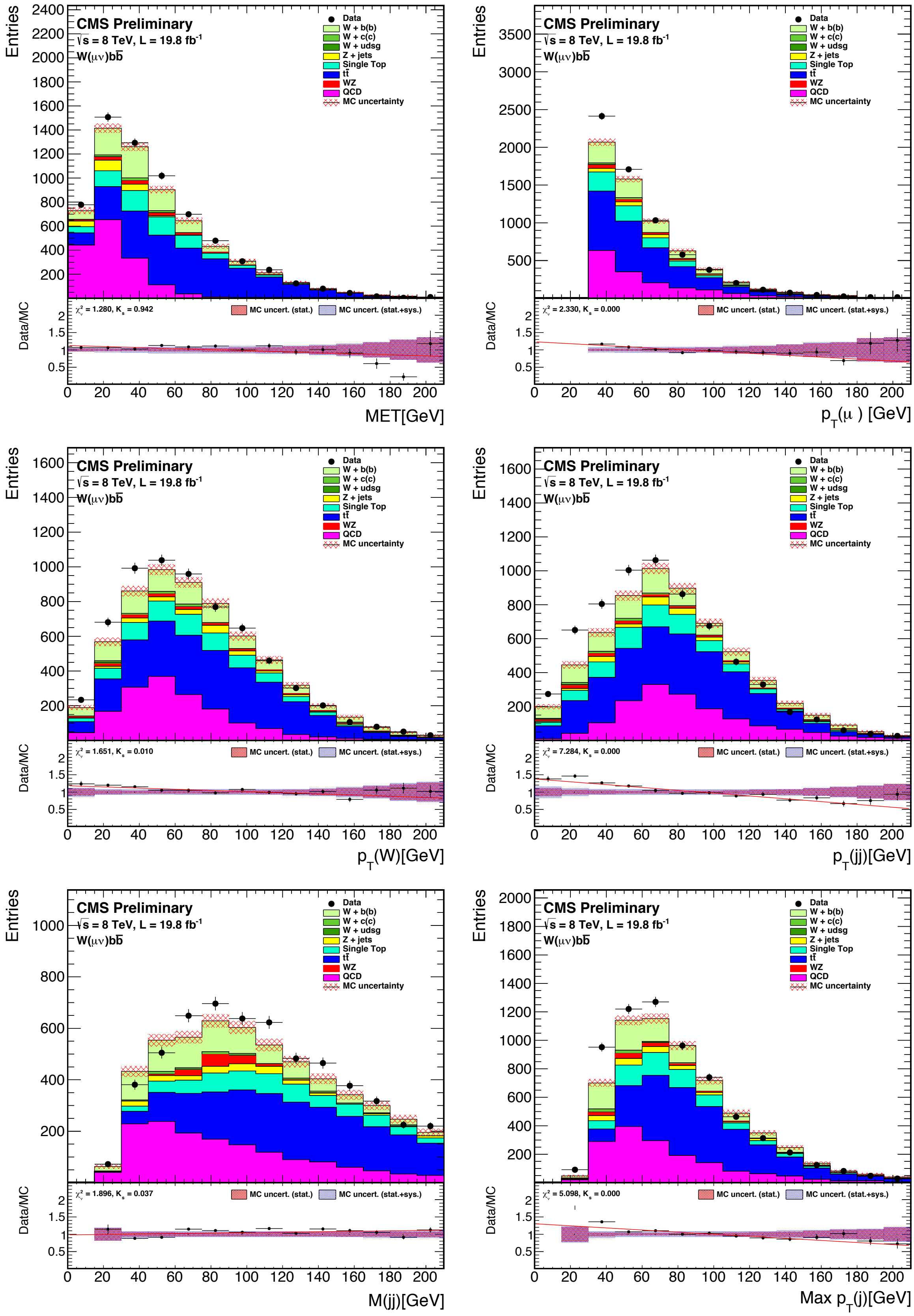

FIGURE 6.6: Various signal region distributions for the electron channel: missing energy, lepton transverse momentum, W transverse momentum, invariant mass and transverse momentum of two b jets and highest jet transverse momentum.

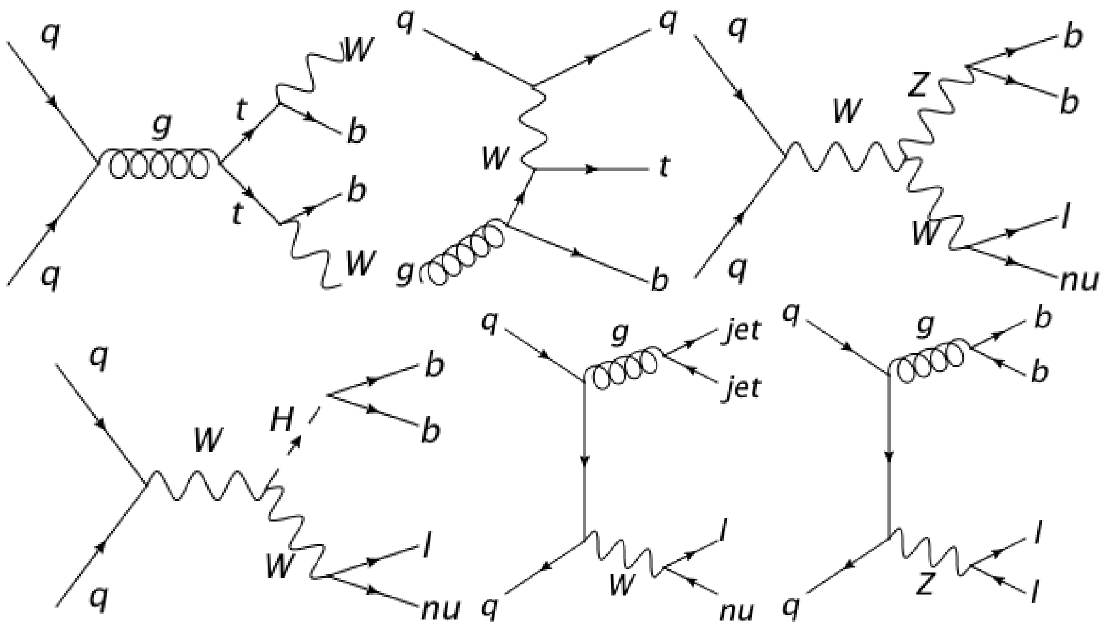

FIGURE 6.7: Feynmann diagrams for major backgrounds: $t\bar{t}$, single top, WZ, WH, W+jets and Z+jets.

is smaller resulting in a smaller contribution in the final distributions. Nevertheless, the contribution from top quark backgrounds in the final sample is around 60%.

As the $t\bar{t}$ background is large, it is mandatory to perform a test of its normalization. For that purpose, a separate control region is defined requiring additional jet activity with jet p_T >25 GeV and $|\eta|$ <2.4. This results in a $t\bar{t}$ enriched sample. Various distributions including missing energy, lepton transverse momentum, W transverse momentum, invariant mass and transverse momentum of the two b jets and the highest jet transverse momentum are shown in figure 6.8. It is visible that the shape of the distributions is in agreement between data and simulation, but the difference in the overall normalization after applying all scale factors is of the order of 12%. The disagreement is likely coming from the b-tagging scale factors not being properly determined. This is taken into account while performing the global fit in order to extract the number of signal events, which will be described in detail in the next chapter.

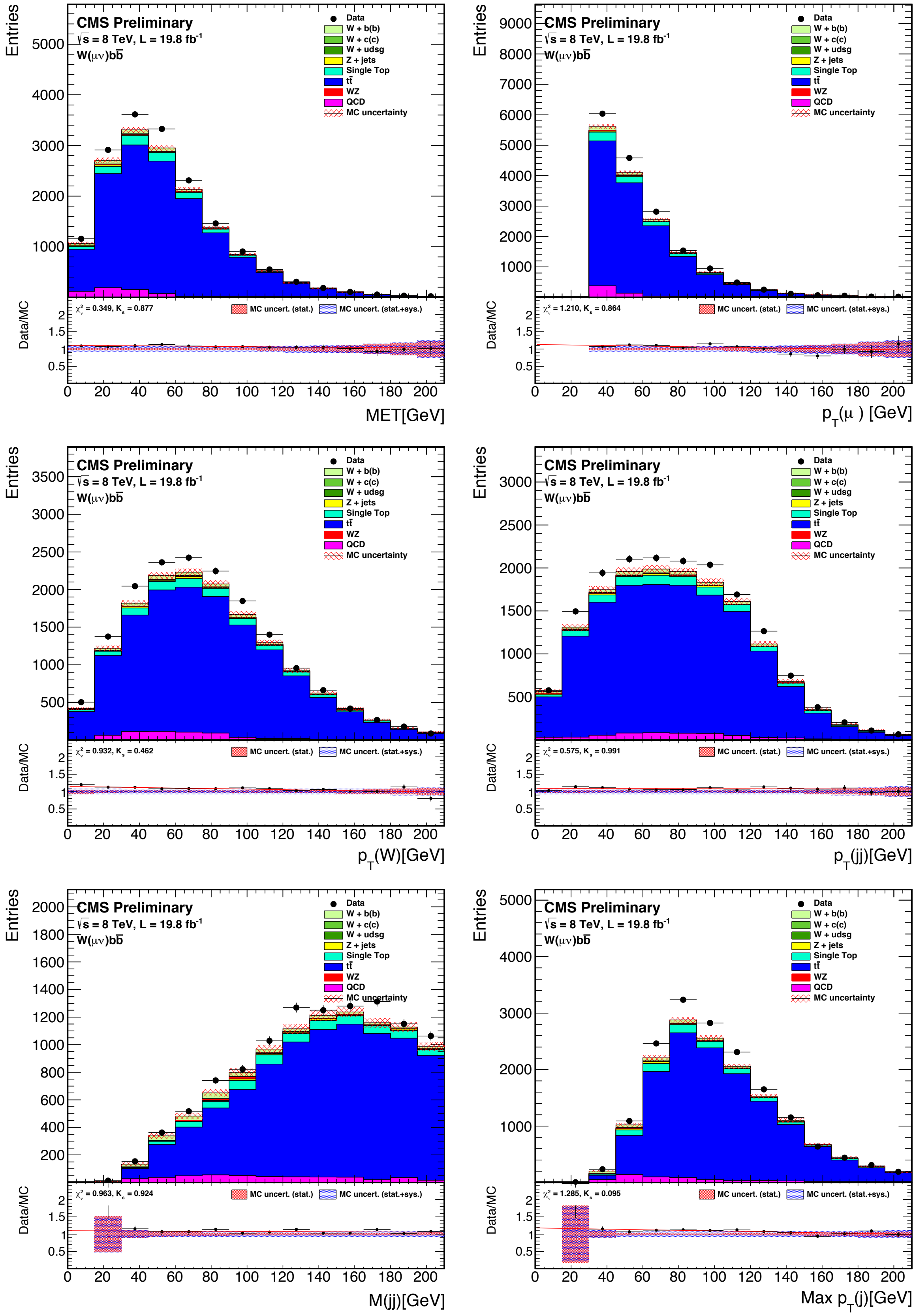

FIGURE 6.8: Various top quark control region distributions: missing energy, lepton transverse momentum, W transverse momentum, invariant mass and transverse momentum of two b jets and highest jet transverse momentum. Good shape agreement between data and simulation is observed, however simulation normalization is smaller than expected from data.

6.4.2 Z+jets

The contribution from the events where a Z boson is produced in association with two b jets is largely suppressed by requiring only one lepton in the event. However, it can happen that one of the leptons from the Z decay escapes detection or is missidentified, which may cause significant missing energy. Such events are then passing all selection criteria and have to be taken into account in the final cross section measurement. Contribution from Z+jets background in the final distribution is around 3%.

6.4.3 W+light jets and W+charm

W+jets is the major background before applying the b-tagging criteria is visible in figure 6.9. Both shape and normalization agree well between data and Monte Carlo for several distributions shown. Very tight b-tag selection, which is applied to the selected jets in the signal region, reduces both W+light jets and W+charm to almost negligible levels.

6.4.4 QCD multijets

The QCD background arises from QCD multijet events containing a soft lepton that passes lepton selection criteria. An example of such an event is shown in the left part of figure 6.10. This is one of the most challenging backgrounds as it is difficult to simulate significant amount of such events because of the very high cross section for such processes. Therefore, the contribution of QCD events in the signal region is determined from data. Two uncorrelated variables are chosen, in this case the transverse mass and the lepton isolation. The transverse mass distribution shows a Jacobian peak for the events containing a W boson. Thus it is a natural choice for discrimination from the final states without W boson. The transverse mass distribution at low values is dominated by QCD multijet events. Their contribution is estimated using the so called ABCD method. The method is illustrated on the right hand side of the figure 6.10. The signal region is marked

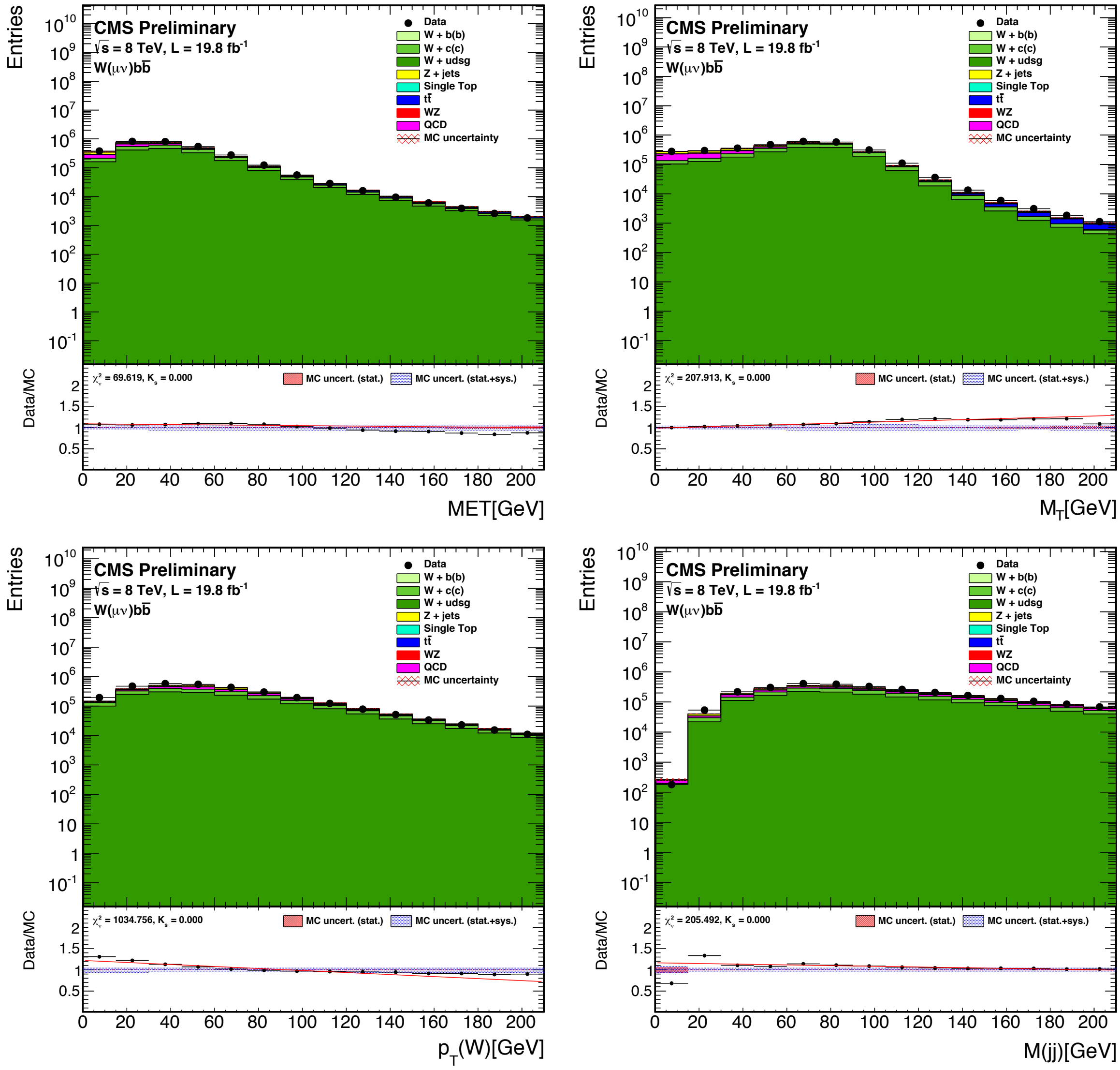

FIGURE 6.9: Distribution obtained using Wbb event selection before applying b-tagging criteria.

with A. A control sample dominated by QCD events is created by inverting the lepton isolation cut to $I_{rel}^{PF} > 0.2$ (0.15) for muons (electrons) and is marked with C. The rest of the selection criteria in the control sample is the same as in the signal region. The obtained sample is relatively clean, however there are still some small contributions from background processes as it is visible in figure 6.11. The shape of the final distribution is determined by subtracting these background events from the data distribution.

It is assumed that the QCD distribution has the same shape in regions A and C.

Normalization of the QCD distribution is determined from the M_T region below 30 GeV (normalizing D region to B region). In these regions, contributions from other processes is subtracted from the data before the normalization using MC expectations. The number of QCD events is expressed as:

$$QCD^A = \frac{N^B_{data} - N^B_{MC}}{N^D_{data} - N^D_{MC}} \times QCD^C_{data} \tag{6.4}$$

where N^B_{data} and N^D_{data} are the number of data events in data in regions B and D respectively, and N^C_{MC} and N^D_{MC} are the number of MC background events in regions B and D respectively. The signal region before and after the QCD contribution determination is shown in figure 6.12. The QCD contribution in the final distribution is approximately 20%.

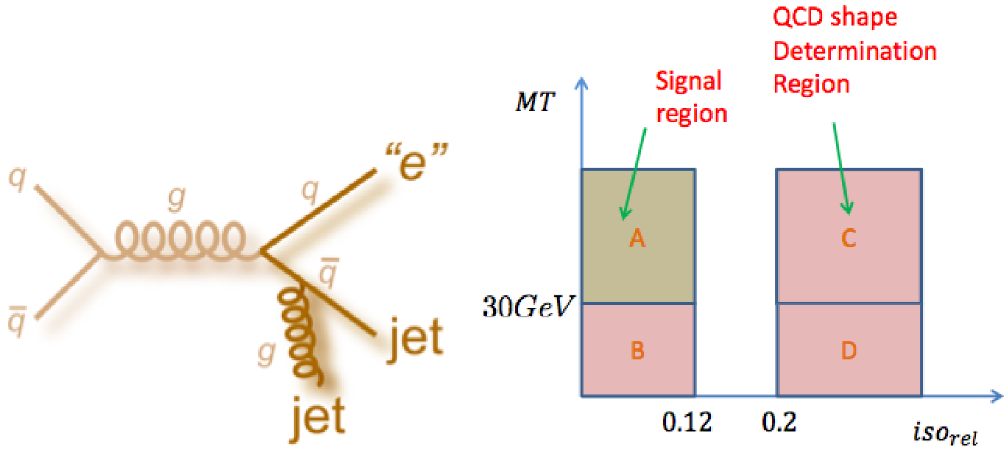

FIGURE 6.10: An example of QCD event which looks like signal event (*left*) and illustration of ABCD method used for QCD background determination (*right*)

6.4.5 Other backgrounds

Other backgrounds include processes with final states that match the final state of the signal. One of such signals is WZ where W decays leptonically and Z decays in a pair of b quarks. Another example is the production of Higgs boson in association with W

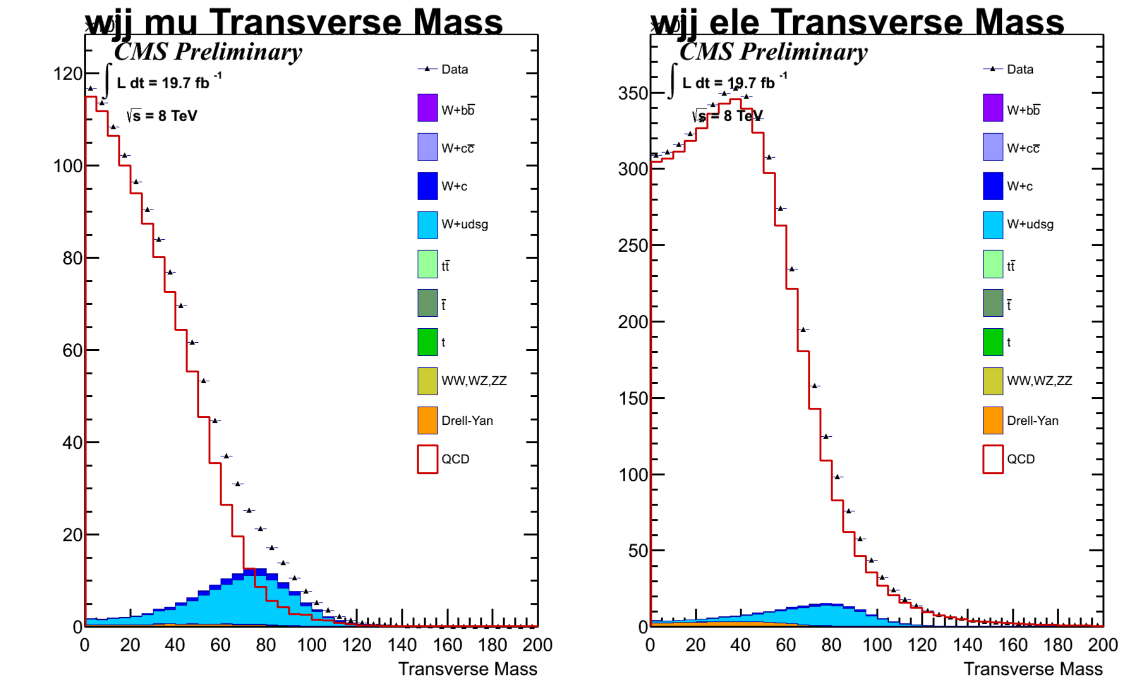

FIGURE 6.11: The shape of the QCD is found by inverting the isolation cut on the lepton and subtracting the remaining MC contributions from the data. This plot shows data and MC in the inverted lepton isolation region together with the extrapolated QCD shape for muon (*left*) and electron (*right*) channel.

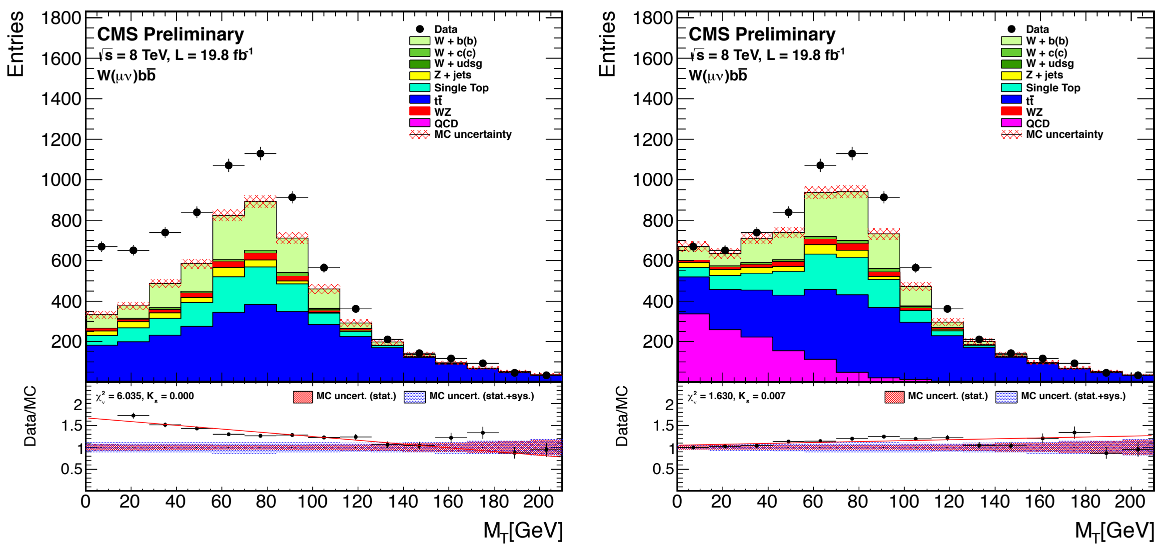

FIGURE 6.12: Transverse mass distribution without (*left*) and with QCD background (*right*).

boson where Higgs decays to a pair of b quarks. Such backgrounds are called irreducible backgrounds.

Chapter 7

Cross section measurement

The cross section for the pp→W+bb+X process is determined separately in the electron and the muon channel using the relation:

$$\sigma = \frac{N_{sig}}{A \times \epsilon \cdot \mathcal{L}} \tag{7.1}$$

where N_{sig} is the overall number of the signal events, which is precisely determined by performing the fit procedure presented in the next sections. $A \times \epsilon$ is the detector acceptance and efficiency (section 7.3) and $\mathcal{L}$ is the total integrated luminosity.

Fit methodology is shortly presented in the section 7.1, while the systematic uncertainties, which are taken into account during the fit, are described in detail in section 7.2. The procedure for the calculation of $A \times \epsilon$ is described in section 7.3 and lastly, in section 7.4 the cross sections results are given and compared to the theoretical prediction.

7.1 Signal extraction method

The Wbb yield is obtained from a fit to the transverse mass distribution recovered after applying the selection criteria described in section 6.3. The fit was performed in the full

M_T range to better constrain the QCD contribution. The Wbb contribution is modeled using the four-flavor scheme and five-flavor scheme separately, as described in detail in 6.1. The comparison between the two samples is given in figure 7.1. Small differences in shapes can be seen.

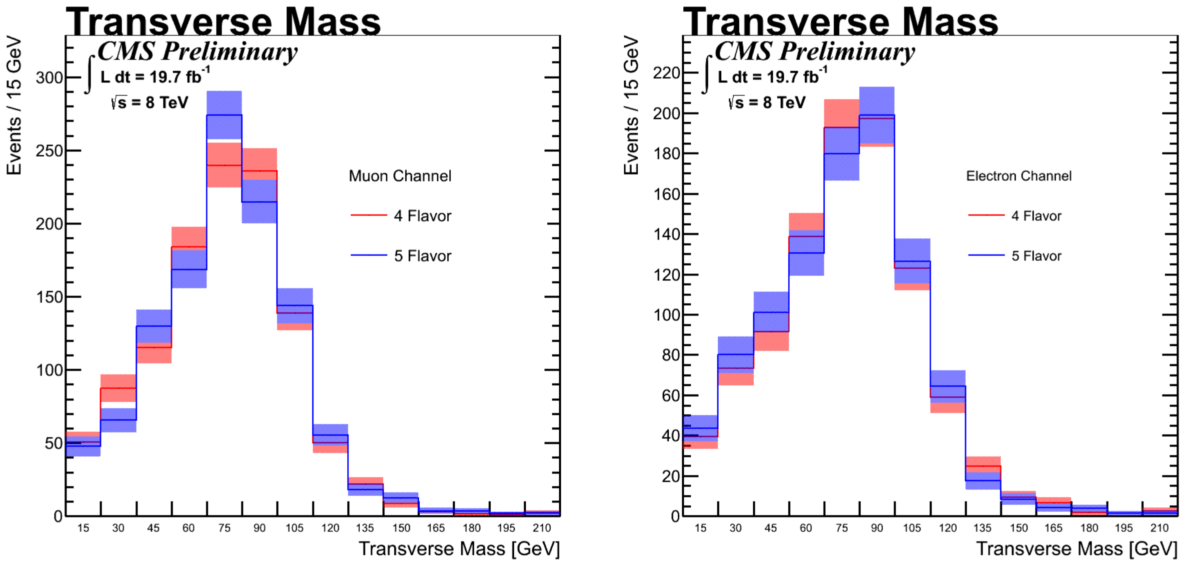

FIGURE 7.1: Shape comparison of the two samples used to obtain the number of signal events. The left figure shows the muon channel while the right figure shows the electron channel.

Signal yields and background yields are extracted using a binned maximum likelihood fit. The details of the fitting procedure are described in [75]. Due to the observed difference in the overall normalization of the $t\bar{t}$ sample, a simultaneous fit was performed in the Wbb region and in the $t\bar{t}$ multijet control region. The predictions for both, signal and background yields, depend on various uncertainties, which are included in the fit as nuisance parameters. The likelihood function is constructed as:

$$\mathcal{L}(\text{data}|\mu, \theta) = Poisson(\text{data}|\mu \cdot s(\theta) + b(\theta)) \cdot p(\widetilde{\theta}|\theta). \tag{7.2}$$

In this expression "data" represents the actual measurements, θ is a set of nuisance parameters describing the uncertainties while $s(\theta)$ and $b(\theta)$ describe signal and background yields respectively, which depend on the nuisance parameters. μ is the signal strength, which is the ratio between the cross section under test and the theoretical cross section. *Poisson* in the context of the binned maximum likelihood represents the product of Poisson probabilities to find n_i events in bin i where the expected number of events is $\mu s_i + b_i$:

$$\prod_i \frac{(\mu s_i + b_i)^{n_i}}{n_i!} e^{-(\mu s_i + b_i)} \tag{7.3}$$

Probability density functions $p(\theta)$, with some $\widetilde{\theta}$ as the best estimate of the parameter set describing each of the nuisances, are used to characterize the nuisances. Different options for *pdf* include flat distribution, Gaussian, log-normal and gamma distribution. In this analysis, systematic uncertainties are treated in two different ways. In cases where the systematic uncertainty does not change the shape of the fitted distribution, a log-normal *pdf* is used because it is suitable for the description of the positively defined variables like cross-section, luminosity or cut efficiency. Here the value of $\widetilde{\theta}$ in the case of the normalizations of different background shapes corresponds to the normalization of the distribution used in the fit. The width of the log-normal distribution $\rho(\theta)$ is defined by the parameter κ:

$$\rho(\theta) = \frac{1}{\sqrt{2\pi} ln(\kappa)} exp\left(\frac{(ln(\theta/\widetilde{\theta}))^2}{2(ln\kappa)^2}\right)\frac{1}{\theta}. \tag{7.4}$$

The value of κ implies by how much an observable can be larger or smaller, both deviations having a chance of 16%. Another way of treating systematic uncertainties is by producing two additional input shapes for each process affected by some uncertainty, by shifting up and down that parameter by one standard deviation. When building the likelihood, each shape uncertainty is associated to a nuisance parameter taken from a unit Gaussian distribution, which is used to interpolate or extrapolate using the specified histograms. After the construction of the likelihood function, parameters θ and μ are extracted by minimizing the likelihood function. The next section lists the major sources of systematic uncertainties together with the strategy used for determination of the corresponding nuisance *pdf*.

7.2 Systematic uncertainties

Systematic uncertainties on the expected signal and background yields and shapes affect the final results. For several systematic variations, a new set of signal and background shapes was created, which may differ both in shape and normalization from the original shape. In cases where systematic uncertainty does not change the shape of the distribution used in the fit, only the systematic effect on the normalization was taken into account as described in the previous section. Several sources of systematic variations have been considered:

Jet energy scale uncertainty

The source of jet energy scale uncertainty arises from the uncertainty on different jet energy corrections applied to unify the detector response in energy and pseudorapidity as described in section 5.4.2. The uncertainty for each level of corrections is estimated separately and added in quadrature to get the final uncertainty [52]. The jet energy scale for each jet is varied within one standard deviation of the applied jet energy corrections and the efficiency of the analysis selection is recomputed to assess the systematic variation on the normalization and shape of the signal and all background components.

Jet energy resolution

The jet energy resolution in simulation is smeared in order to take into account differences between data and Monte Carlo. The uncertainty on the applied smearing factors is used to produce modified signal and background shapes. These modified shapes are then used in the final fit.

Jet b-tagging efficiencies

Jet b-tagging efficiencies are determined for the jets selected in the analysis as described in section 6.2.3. These efficiencies are applied as weight factors for each event and depend on p_T, η and flavour of the selected jets. To estimate the effect of the uncertainties on the efficiency determination, each scale factor is shifted up and down by the corresponding uncertainty, and event weights are recalculated. The procedure is done separately for b jet efficiencies and for light flavour mistag rate. The uncertainty for jets from c quark is taken to be twice as large as the one from b jets since there is no proper measurement for this uncertainty. The scale factor variation is found to be of the order of a few percent.

Lepton scale factors

Muon and electron trigger, reconstruction, and identification efficiencies are determined in data using the standard tag-and-probe technique with Z bosons as described in 6.2.2. The effects of the corresponding uncertainties were assessed by varying the corresponding scale factors by one standard deviation and producing the modified signal and background shapes.

Lepton energy scale

The lepton energy scale measurement uncertainty corresponds to 1% for muons in the whole detector and electrons in the barrel region. Systematic uncertainty of 2.5% is associated to the electrons in the endcap region. The effect on the yield is evaluated by varying the lepton energy scale for each lepton within one standard deviation and creating corresponding transverse mass distributions used in the final fit.

Unclustered missing energy

The uncertainty on missing energy measurement from unclustered energy, e.g. jets with p_T <10 GeV and $|\eta|$ <4.7 is estimated. The energy scale of such jets is varied by 10%, which is propagated into the calculation of missing energy. New transverse mass distributions are created and taken into account in the final fit.

MC samples normalizations

The finite size of the signal and background MC samples are included in the normalization uncertainties. Normalizations for each of the Monte-Carlo samples are also allowed to vary within the uncertainties of measured standard model cross-sections. Cross section uncertainties are summarized in the table 7.1

Luminosity uncertainty

Luminosity measurement is performed using the cluster counting in the Pixel detector described in section 4.8. An uncertainty of 2.6% for the luminosity measurement during 2012 data taking is reported by the CMS luminosity group [76].

Process	Cross section uncertainty
W+c(c)	8.1%
W+udsg	13.2%
Z+jets	7.9%
Single Top	5.4%
$t\bar{t}$	7.4%
VV	8.1%

TABLE 7.1: Standard model cross section uncertainties used in the evaluation of MC normalization systematic effect.

In figures 7.2 and 7.3 the effect of different systematic uncertainties on the shape of the transverse mass distribution is shown for signal and $t\bar{t}$ control region. The shown

M_T distributions are obtained by summing signal and all background contributions. The largest systematic variations come from the b-tagging uncertainties. A more detailed study of the final signal strength dependence on the systematic variations is shown in section 7.4.1.

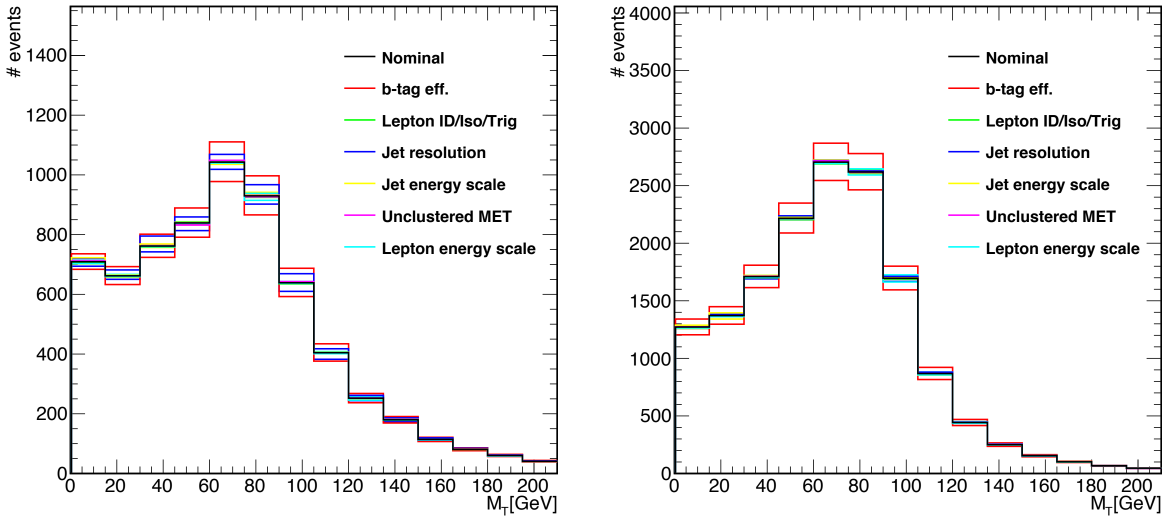

FIGURE 7.2: Shape of the transverse mass distribution in the muon channel for each systematic variation in both, signal region (*left*) and $t\bar{t}$ control region (*right*).

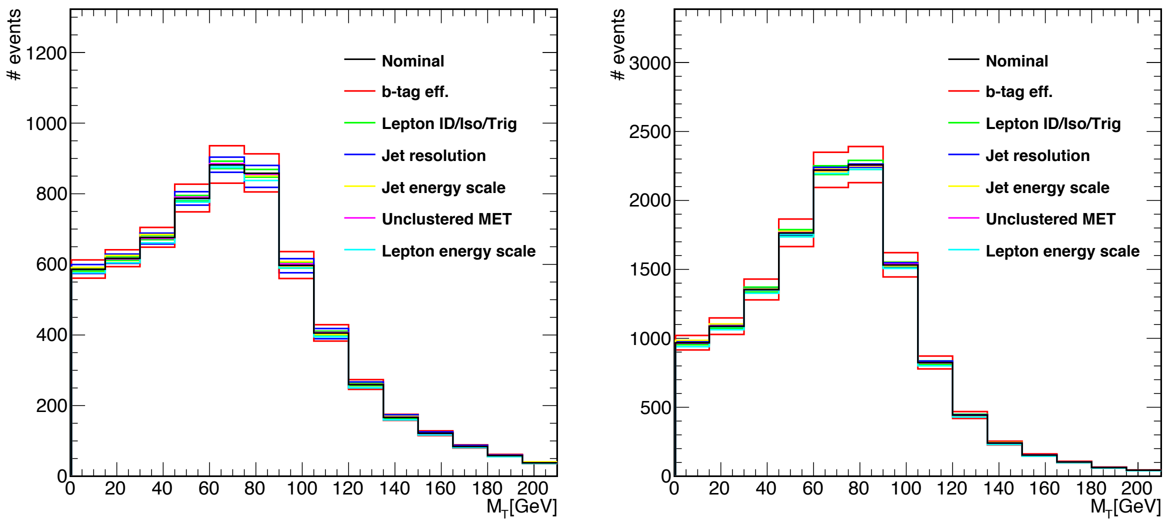

FIGURE 7.3: Shape of the transverse mass distribution in the electron channel for each systematic variation in both, signal region (*left*) and $t\bar{t}$ control region (*right*).

7.3 Acceptance and efficiency

Due to the limitations of the detector, not all produced signal events will be detected. Some final state particles will end up outside the functional part of the detector. The fraction of the phase space covered with a functional detector for signal final state particles is called *acceptance*. The fiducial region in which the cross section is computed corresponds to one lepton with p_T >30 GeV and $|\eta|$ <2.1. The four-momentum of the lepton is corrected for final state radiation by summing all the photons four-momenta inside a cone of 0.1 from the lepton and cut is applied on the corrected value. Additionally, exactly two jets with p_T > 25 GeV and $|\eta|$ <2.4 are required in the event. Jets are clustered from the list of generated particles not considering neutrinos, using anti$-k_T$ algorithm with a cone size of 0.5. Jets are required to contain at least one particle originating from a B hadron decay within a cone of 0.5 from the jet axis in the list of the clustered particles. Fiducial region requirements are summarized in table 7.2. However, a fraction

Variable	Cut
Lepton p_T	$>$ 30 GeV
Lepton $\|\eta\|$	$<$ 2.1
Jet p_T	$>$ 25
Jet $\|\eta\|$	$<$ 2.4
ΔR(jet, B hadron)	$<$ 0.5

TABLE 7.2: Fiducial cuts used for cross section measurements.

of the events that fall into the fiducial volume will not be detected due to trigger and reconstruction inefficiencies or selection cuts imposed at trigger or analysis level. Usually, the acceptance and efficiency are estimated as a single quantity, which is a product of these two numbers, defined as:

$$A \times \epsilon = \frac{\text{number of selected Wbb events}}{\text{number of generated Wbb events in the fiducial volume}} \tag{7.5}$$

This ratio is computed using simulated Wbb sample for each of the channels separately. The number of selected events is obtained by applying the selection cuts described in 6.3.

The number of generated events is obtained by applying generator-level cuts summarized in table 7.2. As this ratio is derived from simulation, it is necessary to correct it for differences between data and Monte-Carlo. These corrections include pile-up w^{PU}, lepton trigger, reconstruction and identification scale factors w^{lep}, and b-tagging scale factors w^{b-tag} all described in 6.2. With all the corrections, $A \times \epsilon$ for each channel becomes:

$$A \times \epsilon = \frac{\sum^{sel} w^{lep} w^{PU} w^{b-tag}}{N^{gen}_{fiducial}} \tag{7.6}$$

where the sum in the numerator runs over selected events. Obtained results are summarized in table 7.3 for each channel.

Channel	A×ϵ
Muon channel	9.14 ± 0.18 %
Electron channel	7.66 ± 0.17 %

TABLE 7.3: Results of the A×ϵ determination for both, muon and electron channel together with the statistical uncertainty.

7.4 Results

Transverse mass distributions in the signal region and $t\bar{t}$ region were fitted simultaneously in order to obtain the signal strength for Wbb. Yields before and after the fit are shown in Table 7.4 for the muon channel and 7.5 for the electron channel. The obtained signal strength values are:

$$\mu_{muon} = 1.37 \pm 0.07(\text{stat.}) \pm 0.20(\text{syst.})$$

$$\mu_{ele} = 1.51 \pm 0.08(\text{stat.}) \pm 0.20(\text{syst.})$$

The total uncertainty was obtained by including both systematic and statistical uncertainties. Another fit was performed without systematic uncertainties in order to obtain the statistical error. The total systematic error was computed by subtracting in quadrature the statistical error from the total error. Figures 7.4 and 7.5 show the most important detector distribution after performing the fit for the muon and electron channels respectively. The recovered distributions show a good agreement between data and simulation for all considered distributions.

TABLE 7.4: Yields obtained in the muon channel before and after the fitting procedure.

Sample	Prefit yields	Fitted yields	Prefit yields($M_T > 45$GeV)	Fitted yields($M_T > 45$GeV)
W+bb	1137.4±25.9	1616.4±209.5	877.1±22.9	1243.4±165.7
W+cc	71.3±7.6	85.5±23.7	55.2±7.3	65.9±20.4
W+udsg	38.2±9.1	55.1±36.5	30.3±8.2	43.8±29.0
Z+jets	208.7±22.4	218.1±36.5	121.8±17.2	127.9±31.7
Single Top	913.1±16.7	989.4±87.2	700.2±14.6	750.1±66.5
$T\bar{T}$	3093.2±13.0	3491.1±109.9	2499.6±11.3	2716.7±86.3
VV	145.2±3.1	152.2±15.3	108.4±2.7	113.4±11.8
QCD	1110.5±28.2	913.6±72.8	293.9±15.2	241.8±19.3
Sum	6717.6±50.6	7521.3±380.4	4686.4±39.0	5302.9±205.2
Data	7481.0		5372.0	
$N_{data} - N_{bkg}$			1312.5±141.5	

TABLE 7.5: Yields obtained in the electron channel before and after the fitting procedure.

Sample	Prefit yields	Fitted yields	Prefit yields($M_T > 45$GeV)	Fitted yields($M_T > 45$GeV)
W+bb	964.2±23.9	1452.3±176.5	732.5±22.9	1107.6±140.9
W+cc	70.5±8.5	72.7±13.2	61.7±7.3	62.0±14.8
W+udsg	15.9±5.4	17.0±4.0	13.0±8.2	13.6±3.3
Z+jets	202.3±21.6	190.3±17.2	89.2±17.2	96.8±22.8
Single Top	722.4±14.9	696.6±48.2	547.6±14.6	527.1±41.3
$T\bar{T}$	2460.2±11.4	2360.3±82.9	1992.0±11.3	1876.4±68.9
VV	110.3±2.7	110.5±10.5	85.4±2.7	86.6±9.0
QCD	1836.0±26.1	1698.7±121.3	910.5±15.2	840.7±60.0
Sum	6381.9±46.6	6598.3±333.6	4432.0±39.0	4610.7±175.3
Data	6575.0		4639.0	
$N_{data} - N_{bkg}$			1135.9±124.6	

7.4.1 Effects of the systematic uncertainties

Information about each source of systematic uncertainty together with the information whether just normalization or shape is included in the final fit is shown in table 7.6 for the muon channel and 7.7 for the electron channel. The tables also show the uncertainties on

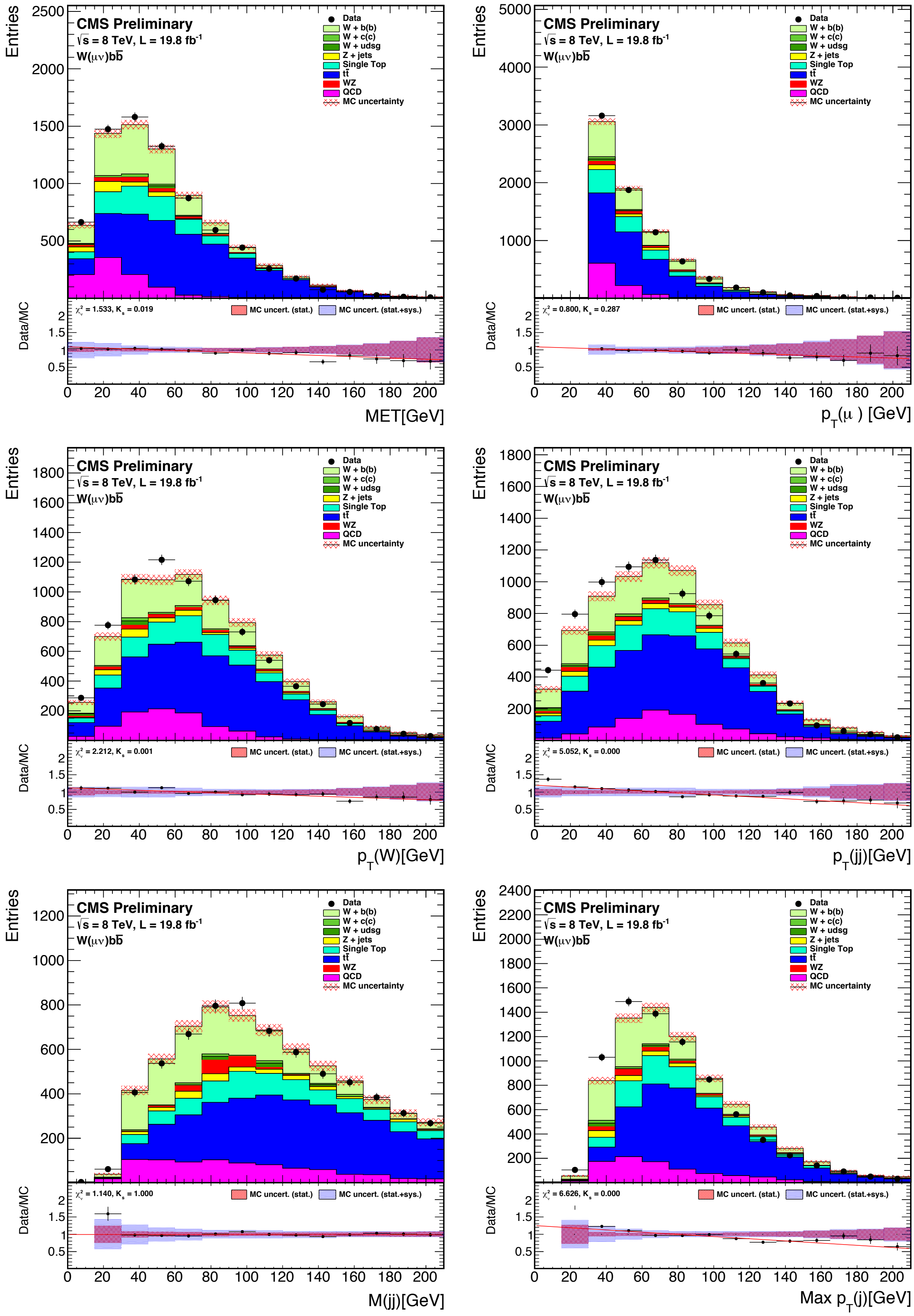

FIGURE 7.4: Muon channel distributions after the fit.

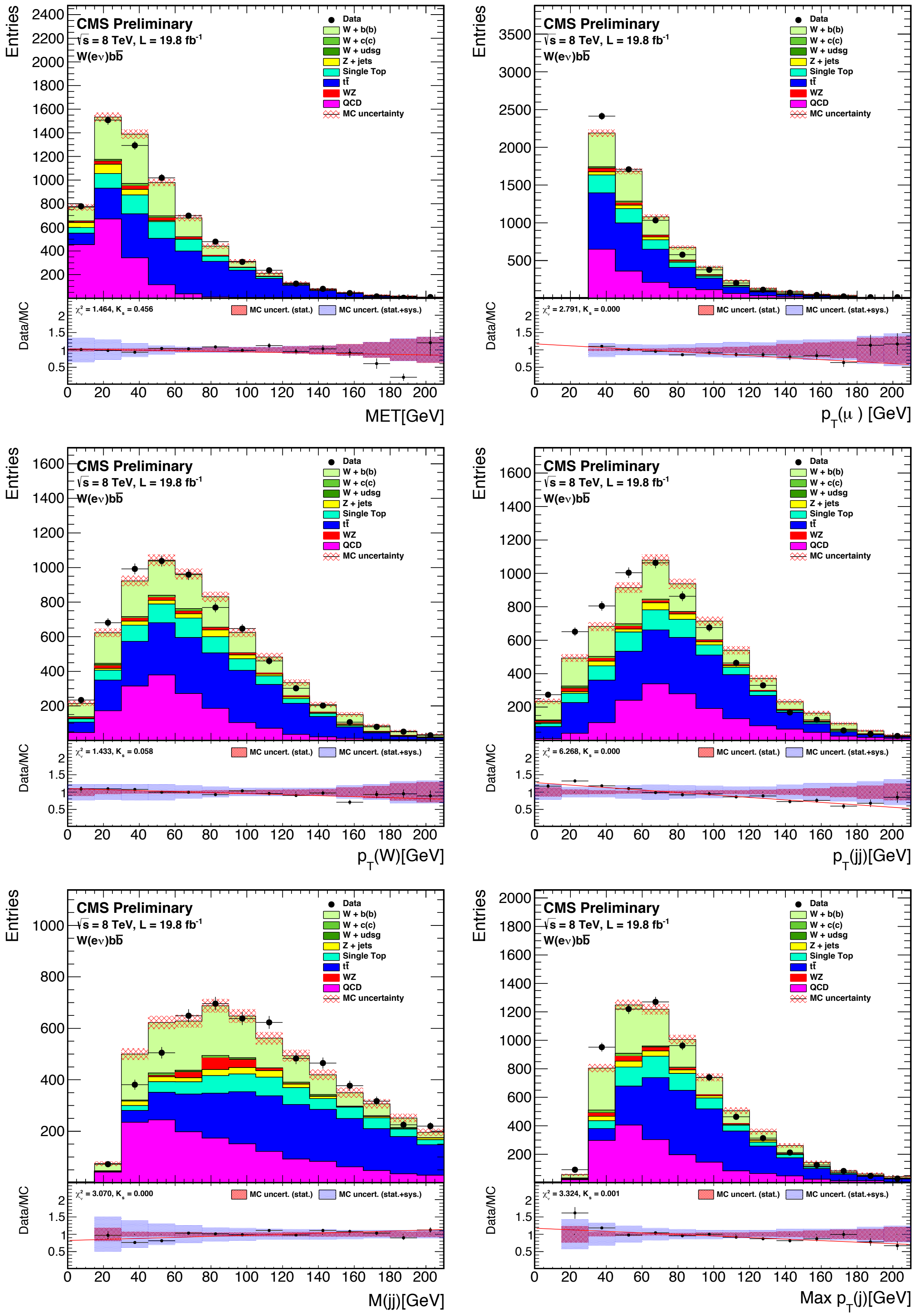

FIGURE 7.5: Electron channel distributions after the fit.

Table 7.6: Systematic uncertainty effect on the final yield is shown in the table together with the uncertainty on the signal and background yields and relative contribution to the signal strength uncertainty.

Source	Type	Event yield uncertainty range (%)	Individual contribution to μ uncertainty (%)	Effect of removal on μ uncertainty (%)
b-tag efficiency	shape	6.80	0.97	3.76
Lepton ID/Iso/Trig	shape	0.57	0.27	< 0.01
Jet resolution	shape	0.03	< 0.01	0.07
Jet energy scale	shape	0.05	3.43	0.63
Unclustered MET	shape	0.00	< 0.01	9.35
Muon energy scale	shape	1.09	0.13	0.01
Luminosity	norm.	2.60	0.67	0.02
Monte Carlo statistics	norm.	0.75	3.63	10.10

Table 7.7: Same as table 7.6 for the electron channel.

Source	Type	Event yield uncertainty range (%)	Individual contribution to μ uncertainty (%)	Effect of removal on μ uncertainty (%)
b-tag efficiency	shape	6.69	1.75	1.50
Lepton ID/Iso/Trig	shape	1.50	0.99	0.04
Jet resolution	shape	0.10	0.04	1.61
Jet energy scale	shape	0.29	1.67	1.55
Unclustered MET	shape	0.00	0.04	< 0.01
Electron scale	shape	0.75	0.02	0.03
Luminosity	norm.	2.60	1.22	< 0.01
Monte Carlo statistics	norm.	0.85	2.88	2.69

signal and background yields and the relative contribution to the signal strength uncertainty. Due to correlations, the total systematic uncertainty is smaller that the quadrature sum of individual uncertainties. The last column shows the decrease in total systematic uncertainty when removing a specific source of uncertainty.

7.4.2 Tests of the fit stability

Additional tests were performed in order to verify consistency of the obtained signal strength. This was done by fitting different combinations of distributions in both signal region and $t\bar{t}$ control region. Additional distributions include missing energy in the signal region and $t\bar{t}$ control region shown in figures 6.5 and 6.8 and invariant mass of third and fourth jet in $t\bar{t}$ control region. All used distributions show good agreement in shapes between data and simulations making them suitable for the fit. Fitting procedure is performed in the muon channel only, as previously described. Obtained signal strengths are summarized in Table 7.8 and are found to be consistent with the transverse mass fit.

Fitted distribution (Wbb/$t\bar{t}$)	Signal Strength	Yield Ratio
M_T/M_T	1.34±0.15	1.55
M_T/E_T^{miss}	1.31±0.14	1.52
$M_T/M(j_3j_4)$	1.35±0.16	1.53
E_T^{miss}/M_T	1.43±0.21	1.64
E_T^{miss}/E_T^{miss}	1.33±0.17	1.53
$E_T^{miss}/M(j_3j_4)$	1.38±0.21	1.55

TABLE 7.8: Signal strengths obtained by fitting different distributions. Signal strengths are found to be consistent with each other within the uncertainties.

7.4.3 Cross section measurement

The inclusive cross section measurement was performed in the fiducial region corresponding to one lepton with p_T >30 GeV and $|\eta|$ <2.1 and exactly two jets $p_T >$ 25 GeV and $|\eta|$ <2.4. Jets are required to have at least one particle originating from a B hadron within a cone of 0.5 from the jet axis. Cross section was computed using the relation 7.1, where the final yields were obtained from the tables 7.4 and 7.5 for muon and electron channel respectively. The N_{sig} was obtained by subtracting the sum of MC contributions of all backgrounds from the number of events obtained in data after applying the selection cuts. Acceptance and efficiency are taken from table 7.3 and luminosity corresponds to 19.8 fb^{-1}. The measured cross sections are:

$$\sigma(pp \to W + bb) \times \mathcal{B}(W \to \mu\nu) = 0.73 \pm 0.03(\text{stat.}) \pm 0.10(\text{syst.})$$
$$\sigma(pp \to W + bb) \times \mathcal{B}(W \to e\nu) = 0.75 \pm 0.04(\text{stat.}) \pm 0.10(\text{syst.})$$

The quoted systematic and statistical uncertainties take into account all previously described effects. However, these results are not taking into account the systematic effects on the acceptance and efficiency calculation of different choices for the parton distribution functions, or the effect of variation of factorization and renormalization scales. These effects were assessed in the previous measurements of Wbb process by the CMS experiment and contribute 10% to the total cross section uncertainty [33]. The obtained cross sections are in good agreement as predicted by the standard model.

7.4.4 Theoretical predictions and comparison with the measurement

The theoretical prediction for the cross section defined in table 7.2 was estimated using MCFM 6.8 in the massless five flavour scheme at NLO precision with factorization and renormalization scales set to the mass of the W boson. A hadronization correction factor 0.92 ± 0.01 to extrapolate from the final-state particle jets to the parton-level cross section is estimated with MADGRAPH+PYTHIA. The obtained result is the following:

$$\sigma_{TH}(pp \to W{+}bb) \times \mathcal{B}(W \to l\nu) = 0.508 \pm 0.001(\text{stat.}) \pm 0.005(\text{PDF}) \pm 0.029(\text{scale}) \pm 0.01(\text{hadr.})\ \text{pb}$$

The statistical uncertainty associated to this result comes from the integration step of the calculation; the PDF and scale uncertainties have been estimated by repeating the calculation with different PDF sets and by varying the renormalization and factorization scales by a factor two with respect to the reference values (M_W).

The double parton scattering contribution was not taken into account during the theoretical calculation. However, it has been estimated following the procedure described in section 2.2.2.1 using the formula:

$$\sigma_{DPS} = \frac{\sigma_W \times \sigma_{bb}}{\sigma_{eff}} \tag{7.7}$$

where σ_W and σ_{bb} are the corresponding single parton scattering cross sections for the production of the W boson and the production of b quark pair respectively. These cross sections were estimated for the same fiducial region as for the analysis and correspond to:

$$\sigma_W = 4361 \pm 79 \text{ pb}$$
$$\sigma_{bb} = 0.18 \pm 0.09 \ \mu\text{b}.$$

The inclusive cross section for the W boson production σ_W is estimated with FEWZ [77] at NNLO level. The total cross section for a pair of b quarks is estimated on a sample of events created with Madgraph and is accurate to LO precision, yielding a much larger associated uncertainty. The value of the effective cross section σ_{eff} measured by the CMS is:

$$\sigma_{eff} = 20.7 \pm 6.6 \text{ mb}.$$

The resulting contribution from double parton scattering to the Wbb cross section is:

$$\sigma_{DPS} = 0.40 \pm 0.02 \text{ pb}.$$

yielding the final Wbb cross section of:

$$\sigma_{TH}(pp \to W + bb) \times \mathcal{B}(W \to l\nu) = 0.55 \pm 0.03(\text{theor.}) \pm 0.02(\text{DPS}) \text{ pb}.$$

The results for the cross section measurement obtained in this thesis are one standard deviation away from the theoretical predictions for the electron and the muon channel.

Chapter 8

Conclusions

This thesis presents the inclusive cross section measurement for W boson production in association with two b jets in proton-proton collisions at $\sqrt{s}$ =8 TeV. The analyzed data have been collected with the CMS detector during 2012, corresponding to an integrated luminosity of 19.8 fb^{-1}. From the theoretical point of view, this process is important as a probe into the perturbative QCD calculations and can point to the need of improvement of theoretical calculations. On the other hand, from the experimental point of view, accurate knowledge of Wbb process leads to more precise measurements of other processes to which this one is a background, such as the top quark or associated Higgs and W boson production, with Higgs boson decaying to a pair of b quarks.

The cross section measurement was performed in the fiducial region defined by a presence of a lepton and exactly two 2 b-tagged jets. The result is quoted separately in the muon and electron channel:

$$\sigma(pp \to W + bb) \times \mathcal{B}(W \to \mu\nu) = 0.73 \pm 0.03(\text{stat.}) \pm 0.10(\text{syst.})$$
$$\sigma(pp \to W + bb) \times \mathcal{B}(W \to e\nu) = 0.75 \pm 0.04(\text{stat.}) \pm 0.10(\text{syst.})$$

The measured values in the two channels are compatible, as predicted by the standard model. The theoretical cross section was derived using MCFM. The measured values are around one standard deviation higher than the predicted theoretical values. Several measurements including a W boson and b jets in the final state were performed in the past. However the results cannot be directly compared because of different phase space and slightly different final states.

The uncertainty on the measured values is dominated by the systematic effects. The largest uncertainties are associated with the b tagging procedure, jet energy scale and jet energy resolution. Reducing these uncertainties in the future, would allow for more sensitive test of perturbative QCD calculation at next-to-leading order.

After the long shutdown, which started in 2013, the LHC has just restarted its operations, reaching the highest energy of $\sqrt{s} = 13$ TeV. This marks the start of another exciting period, which is aimed at precision measurements of Higgs boson as well as various beyonf standard model searches like supersymmetry which may even answer the question of dark matter. As for the measurements of W boson produced in association with b quarks, one of the main goals for the future is to reduce the large systematic uncertainties as stated previously. Measuring differential cross section as a function of various variables, like leading jet transverse momentum, would be of great interest to theorists. Another goal would be to probe different final states, for example studying events with two B hadrons in the same jet, or using track based tagging without requiring jets. This would allow us to study collinear final state in depth.

Chapter 9

Strukturirani sažetak - Mjerenje udarnog presjeka zajedničke produkcije W bozona i para b kvarkova

9.1 Uvod

Standardni model fizike elementarnih čestica je teorija nastala šezdesetih i sedamdesetih godina dvadesetog stoljeća, pokušavajući odgovoriti na pitanje od čega je materija načinjena i kako interagira. Predviđanja Standardnog modela testirana su veliki put puta različitim eksperimentima, međutim nikada nisu opovrgnuta. Jedina nedostajuća karika bio je Higgsov bozon, čestica čije je postojanje portvrđeno 2012. godine, a svojstva su joj izmjerena narednih godina. Time je zaokružena slika Standardnog modela. Međutim, postoje različiti fenomeni koji ne se ne mogu opisati u okviru Standardnog modela kao što su postojanje neutrinskih oscilacija, asimetrije između materija i antimaterije, postojanje tamne materije i tamne energije. Ovi fenomeni upućuju na postojanje fizike izvan

Standardnog modela. Osjetljivost pojedinog eksperimenta na opažanje takvih fenomena izravno je povezano s preciznim mjerenjem već postojećih procesa.

Događaji u kojima je W bozon produciran zajedno s b kvarkvima u središtu je različitih teorijskih i eksperimentalnih istraživanja. Međutim, teorijska predviđanja još uvijek ne objašnjavaju dovoljno dobro eksperimentalne rezultate zbog pojave divergencija u slučaju kada izračeni gluoni imaju jako malu energiju ili je par kvarkova kolinearan. Nadalje, precizno mjerenje W bozona produciranog s parom b kvarkova omogućava bolje razumijevanje i teorijska predviđanja u okviru perturbativne kvantne kromodinamike (pQCD) i provjere valjanosti različitih teorijskih modela korištenih u simulacijama. Ovaj proces je i pozadina za različita mjerenja u okviru Standardnog modela, uključujući mjerenja povezana s top kvarkom i Higgsovim bozonom koji se raspada u par b kvarkova.

Tema ove teze je mjerenje udarnog presjeka za proces $pp \to W + bb + X$ koristeći podatke prikupljene CMS detektorom tijekom 2012 godine na energiji $\sqrt{s} = 8$ TeV. W bozon se raspada na elektron ili mion i odgovarajući neutrino. Prisutnost W bozona se očituje kroz postojanje izoliranog leptona visokog impulsa te nedostajuće energije koja dolazi od slabo interagirajućeg neutrina. Kvarkovi se u detektoru vide kao usmjereni mlazovi čestica te prolaze kroz posebne algoritme koji identificiraju mlazove nastale od b kvarkova.

9.2 Teorijski uvod i prethodna mjerenja

Složenost sudara protona proizlazi iz njihove unutarnje strukture. Iako je proton najvećim dijelom sastavljen od *uud* valentnih kvarkova, ostali kvakovi koje nazivamo kvarkovima mora, te gluoni također mogu sudjelovati u sudarima. Točna predviđanja konačnih stanja u sudarima protona uvelike ovise o kombinaciji teorijskih izračuna i eksperimentalnih rezultata. Opis takvih konačnih stanja se dijeli u nekoliko stupnjeva koji se odvijaju na različitim energijskim skalama. Na najvišim energijama se odvija tvrdi proces koji rezultira produkcijom teških ili visoko-energetskih čestica. Teške čestice se potom raspadaju na lakše. Ova dva procesa opisuju se matrični elementom. Pljusak partona je idući stupanj u opisu sudara protona i označava proces u kojem su izračene lagane čestice, fotoni i gluoni, koji su često kolinearni s originalnom česticom. Zadnji stupanj je hadronizacija tijekom koje partoni formiraju hadrone čijim se raspadima produciraju stabilne čestice opažene u detektoru.

Prethodna mjerenja procesa koji u konačnom stanju sadrže W bozon i b kvarkove izvršena su na Tevatronu, eksperimentima CDF i D0 [34, 35] te na LHC-u, eksperimentima ATLAS i CMS [33, 36]. Prethodna mjerenja ne mogu se izravno uspoređivati, budući da su proučavana različita konačna stanja u različitim faznim prostorima. Međutim, usporedba sa teorijskim predviđanjima ukazuje na slaganje.

9.3 LHC

Veliki hadronski sudarivač je ubrzivač protona smješten na švicarsko-francuskoj granici, u blizini Ženeve [41]. Nalazi se u podzemnom tunelu promjera 27 km, na prosječnoj dubini od 100 m. Veliki hadnonski sudarivač je najveći u nizu akceleratora čija je zadaća postupno ubrzavanje čestica, do maksimalne energije $\sqrt{s} = 14$ TeV. Snopovi čestica, kada dosegnu ciljanu energiju, sudaraju se na četiri mjesta gdje su izgrađeni detektori koji mjere čestice nastale u sudarima. Na dva mjesta nalaze se detektori široke namjene ATLAS (A Toroidal LHC Apparatus) [38] i CMS (Compact Muon Solenoid) [37]. Ovi detektori pokrivaju široki spektar tema iz fizike visokih energija, uključujući potragu za Higgsovim bozonom, supersimetričnim česticama, te detaljna mjerenja svojstava Standardnog modela. ALICE (A Large Ion Collider Experiment) detektor proučava kvarkovsko-gluonsku plazmu u sudarima iona olova [39]. LHCb (LHC Beauty) je usmjeren na pručavanje B fizike kroz raspade B mezona [40]. LHC je modularni ubrzivač sastavljen od oko 10000 različitih supravodljivih magneta koji fokusiraju i usmjeravaju snop čestica.

Snopovi se ubrizgavaju u LHC u obliku paketa protona te se ubrzavaju pomoću radiofrekventnih komora (RF). Tijekom 2012. godine, prosječan broj sudara je bio oko

21 unutar jednog sudara paketa protona. Broj sudara po jedinici vremena se naziva luminozitet, a ukupan broj sudara se u nekom vremenskom periodu se naziva integrirani luminozitet. Tijekom 2012. godine ukupno je prikupljeno više od 24 fb^{-1} inegriranog luminoziteta.

9.4 CMS detektor

Kompaktni mionski solenoid (CMS) izgrađen je oko jedne od četiri točaka interakcije na velikom hadronskom sudarivaču. Detektor je slojevitog cilindričnog dizajna, hermetički zatvoren i gotovo potpuno pokriva cijeli prostorni kut oko točke interakcije. CMS detektor koristi desni koordinatni sustav s ishodištem u središtu detektora. z os je postavljena duž smjera snopa, x os je usmjerena prema središtu prstena, a y os je okomita na njih. Detektor je podijeljen na centralni dio (*barrel*) koji se proteže do $\eta \approx \pm 1.5$, te bočne dijelove (*endcaps*). Unutar CMS-a nalazi se solenoid koji generira polje od 3.8 T u unutarnjem volumenu i oko 2 T izvan. Unutar solenoida nalaze se detektor tragova i kalorimetri, a izvan mionske komore. Jako magnetsko polje zakreće putanje nabijenih čestica nastalih u sudarima i omogučava mjerenje njihovog impulsa.

U samom središtu detektora, oko točke interakcije, smješten je silicijski piksel detektor. Sastoji se od tri sloja u središnjem dijelu i dva diska sa svake strane i sadrži oko 66 milijuna piksela. Oko njega nalazi se silicijski *strip* detektor, koji se sastoji od niza žica. U žicama se prolaskom nabijene čestice inducira naboj koji se potom dovodi do silicijskih detektora.

Elektromagnetski kalorimetar (ECAL) izgrađen je od olovnog volframata, kristala velike gustoće i malog Moliereovog radijusa, što rezultira kratkim i uskim pljuskovima prilikom upada fotona ili elektrona. Hadronski kalorimetar (HCAL) sastoji se od slojeva mjedenih absorbera i plastičnih scintilatora u središnjem dijelu, te čeličnih absorbera i kvarcnih scintilatora u bočnim dijelovima. Svrha hadronskog kalorimetra je zastavljanje hadronskih snopova, što se događa u absorberima, a rezultirajući pljusak čestica se detektira scintilatorima.

Mionske komore sastoje se od nekoliko vrsta detektora punjenih plinom. Driftne komore smještene su u središnjem dijelu i napunjene su plinom koji se ionizira prolaskom čestice. Katodne trakaste komore nalaze se u bočnim dijelovima te funkcioniraju na isti način kao i driftne komore, ali su dodatno isprepletene velikim brojem žica za prikupljanje naboja. Komore s otpornim pločama sastoje se od paralelnih ploča velike otpornosti između kojih je plin. U slučaju prolaska čestice dolazi do ionizacije plina i stvaranja pljuska elektrona. Ove detektore karakterizira visoka vremenska razlučivost, te su pogodni za korištenje kao dio sustava za okidanje.

Protoni u LHC-u se sudaraju frekvencijom od 40 MHz i generaju veliku količinu podataka koju nije moguće pohraniti. Uzimajući u obzir da su udarni presjeci za zanimljive fizikalne procese redove veličina manji od udarnog presjeka za sudar protona, potrebno je konstruirati sustav okidača koji će zapisivati samo zanimljive događaje. Ovaj sustav je dizajniran na dvije razine. Prva razina koristi posebnu elektroniku i pomoću jednostavnih zahtjeva na svaki događaj, uspijeva unutar 3 μs smanjiti broj događaja s 40 MHz na oko 100 kHz. Iduća razina se naziva *High Level Trigger* (HLT), čija je zadaća smanjiti broj sudara na oko 100 u sekundi.

9.5 Rekonstrukcija fizikalnih objekata

Elektoni u detektoru ostavljaju trag u detektoru tragova i deponiraju energiju u elektromagnetskom kalorimetru. Elektron prolaskom kroz materijal može emitirati i tzv. zakočno zračenje, odnosno fotone koji također deponiraju energiju u elektromagnetskom kalorimetru. Svi energetski depoziti od jednog elektrona formiraju tzv. *supercluster* koji se potom kombinira s tragom u detektoru tragova koristeći GSM (*Gaussian Sum Filter*) algoritam [46, 47].

Mione karakterizira trag u detektoru tragova i signali u mionskim komorama. Rekonstrukcija kreće od mionskih komora gdje se prilagodbama iz signala rekonstruira trag (tzv. *stanalone muon*). Zatim se izgrađuje globalni mion kombiniranjem traga iz detektora tragova i traga iz mionskih komora [48, 49].

Mlazovi su usmjerena grupa hadrona koja nastaje kao rezultat fragmentacije i hadronizacije kvarkova. Detektirani hadroni se kombiniraju u mlaz posebnim algoritmima, čime se pokušavaju saznati informacije o početnom partonu. Najpopularniji takav algoritam je anti$-k_T$ algoritam koji na osnovu udaljenosti čestica i njihovih impulsa grupira čestice unutar unaprijed definiranog konusa oko čestice najvišeg impulsa [51]. Proces je iterativan i nastavlja se sve dok svi hadroni ne budu pridruženi nekom mlazu.

Mlazovi iz b kvarkova se identificiraju pomoću posebnih algoritama [56]. Ti algoritmi koriste karakteristična svojstva b kvarkova kao što su njihova masa i dugo vrijeme života za formiranje jedinstvene varijable koja definira koliko je neki mlaz nalik na mlaz nastao iz b kvarka. Algoritam korišten u ovoj tezi je CSV (*Combined secondary vertex*) koji traga za sekundarnim točkama interakcije koje su odmaknute od mjesta sudara i gleda tragove čestica iz tog mjesta sudara.

Nedostajuća transverzalna energija je neravnoteža u transverzalnom impulsu svih detektiranih čestica i određuje se kao:

$$E_T^{miss} = | - \sum_i \vec{p}_i|. \tag{9.1}$$

Budući da je trasverzalni impuls očuvan, nedostajuća energija mjeri impuls kojeg odnose nevidljive čestice. Određivanje nedostajuće energije je ovisno o rezoluciji detektora, ograničenoj pokrivenosti prostornog kuta, pogrešnom interpretacijom detektiranog signala ili kozmičkim zrakama. Ove pojave mogu umjetno povećati iznos nedostajuće energije što treba uzeti u obzir [60].

9.6 Selekcija događaja i navažnije pozadine

U tezi su predstavljeni rezultati mjerenja udarnog presjeka za produkciju W bozona zajedno s parom mlazova nastalih iz b kvarka u sudarima protona na energiji $\sqrt{s} = 8$ TeV. Podaci su prikupljeni 2012. godine CMS detektorom i odgovaraju integriranom luminozitetu od 19.8 fb^{-1}. Za simuliranje signala i pozadine korišteni su generatori Madgraph [65], Powheg [68] i Pythia [61].

Zbog boljeg slaganja podataka i simulacija, na simulacije se primjenjuje niz korekcija:

- Korekcije zbog različitog broja primarnih interakcija. Budući da su simulirani uzorci često generirani prije nego što su uvjeti tijekom prikupljanja podataka poznati, kao što je trenutni luminozitet, potrebno je korigirati simulirane događaje. Korekcija se provodi pridavanjem težine svakom simuliranom događaju tako da raspodjela broja primarnih interakcija u događaju izgleda jednako u podacima i simulacijama [73].
- Efikasnost identifikacije, izolacije i okidača za leptone. Efikasnosti su određene iz podataka korištenjem tzv. *Tag-and-probe* metode, ovisne su o transverzalnom impulsu i pseudorapiditetu te se primjenjuju kao težine za svaki simulirani događaj.
- Efikasnost algoritma za određivanje b mlazova. Budući da je teško točno modelirati sve parametre koji ulaze u algoritam za određivanje b mlazova, potrebno je korigirati simulirane događaje za omjer efikasnosti algoritma u podacima i simulacijama [57].

Događaji korišteni za mjerenje udarnog presjeka moraju sadržavati W bozon koji se raspada na mion ili elektron, te značajnu količinu nedostajuće energije koja ukazuje na postojanje neutrina. Rekonstruirani mlazovi čestica trebaju zadovoljavati kriterije za b mlazove. Svi kriteriji za selekciju događaja sabrani su ovdje:

- Jedan mion ili elektron s $p_T > 30$ GeV i $|\eta| <2.1$ i izolacijskom varijablom $I_{rel}^{PF} < 0.12$ (0.10) za mione (elektrone),

- Točno dva mlaza s $p_T > 25$ GeV i $|\eta|$ <2.4 i konusom između mlaza i leptona većim od 0.5,
- Događaji koji sadrže više od dva mlaza s $p_T > 25$ GeV i $|\eta|$ <2.4 su odbačeni,
- Događaji koji sadrže dodatni lepton s $p_T > 10$ GeV i $|\eta|$ <2.1 su odbačeni,
- Oba mlaza moraju imati disktiminantu za određivanje b-mlazova veću od 0.898,
- Iznos transverzalne mase mora biti veći od 45 GeV.

Najvažnije pozadine uključuju procese s t kvarkovima, Z i W bozone producirane zajedno s mlazovima, dvobozonske događaje te QCD događaje. Pozadine s t kvarkovima su reducirane zahtjevima za točno jednim leptonom i dva mlaza, međutim nakon toga zahjeva, doprinos od tih procesa u konačnom uzorku je oko 60%. Zbog toga je konstruirano posebno kontrolno područje dominirano doprinosom procesa s t kvarkovima u konačnom stanju s ciljem provjere normalizacije tih procesa. Kontrolno područje je dobiveno zahtjevom za više od dva mlaza u konačnom stanju. Uočeno je da je razlika između podataka i simulacija oko 12% što je uzeto u obzit prilikom određivanja broja događaja signala.

Događaji koji sadrže Z bozon i mlazove u konačnom stanju mogu proći selekciju ako jedan lepton nije dobro rekonstruiran, čime se umjetno stvara nedostajuća energija. Procesi s W bozonom i mlazovima nastalim od lakih kvarkova u konačnom stanju reducirani su na zanemarive vrijednosti postavljanjem zahtjeva na diskriminatornu varijablu b tagging algoritma. Dvobozonski procesi u kojima nastaju W i Z bozon koji se potom raspada na par b kvarkova čine ireducibilnu pozadinu. QCD procesi u konačnom stanju sadrže lepton koji uspjeva proći konačnu selekciju, ali nije nastao raspadom W bozona. Ova pozadina se određuje direktno iz podataka. Oblik raspodjele je određen invertiranjem izolacije na lepton i oduzimanjem MC doprinosa od podataka. Normalizacija raspodjele određuje se u području niskih vrijednosti transverzne mase $M_T < 30$ GeV.

9.7 Rezultati

Udarni presjek za proces pp→W+bb+X mjeren je odvojeno u elektronskom i mionskom kanalu i određen je izrazom:

$$\sigma = \frac{N_{sig}}{A \times \epsilon \cdot \mathcal{L}} \tag{9.2}$$

gdje je N_{sig} ukupni broj događaja signala koji je određen prilagodbom. $A \times \epsilon$ definira aktivno područje i efikasnost detektora, a $\mathcal{L}$ integrirani luminozitet. Aktivno područje i efikasnost detektora definirano je kao:

$$A \times \epsilon = \frac{\text{broj izabranih Wbb događaja}}{\text{broj generiranih Wbb događaja}} \tag{9.3}$$

Ova se vrijednost određuje iz simulacija za svaki kanal posebno. Rezultat je naveden u tablici 9.1. Broj događaja signala određen je prilagodbom distribucije transverzne mase

Channel	A×ϵ
Mionski kanal	9.14 ± 0.18 %
Elektronski kanal	7.66 ± 0.17 %

Tablica 9.1: Rezultati određivanja A×ϵ za mionski i elektronski kanal.

koristeći metodu najveće vjerodostojnosti (*maximum likelihood fit*). Prilagodba je izvedena istovremeno u signalnom području i u prethodno opisanom kontrolnom području koristeći distribucije prikazane na slici 9.1. Sistematski efekti su također uzeti u obzir na način da su za svaki doprinos i za svaku pozadinu producirane dvije dodatne distribucijem koje odgovaraju pomaku od jedne standardne devijacije gore i dolje u odnosu na nominalnu vrijednost. Promatrani izvori sistematskih neodređenosti su:

- Mjerenje energije mlazova,
- Rezulucija mlazova,
- Efikasnost određivanja b mlazova,

- Mjerenje energije leptona,
- Efikasnost okidača te identifikacije i izolacije leptona,
- Nedostajuća energija od mlazova niskih energija,
- Normalizacije simuliranih uzoraka,
- Mjerenje luminoziteta.

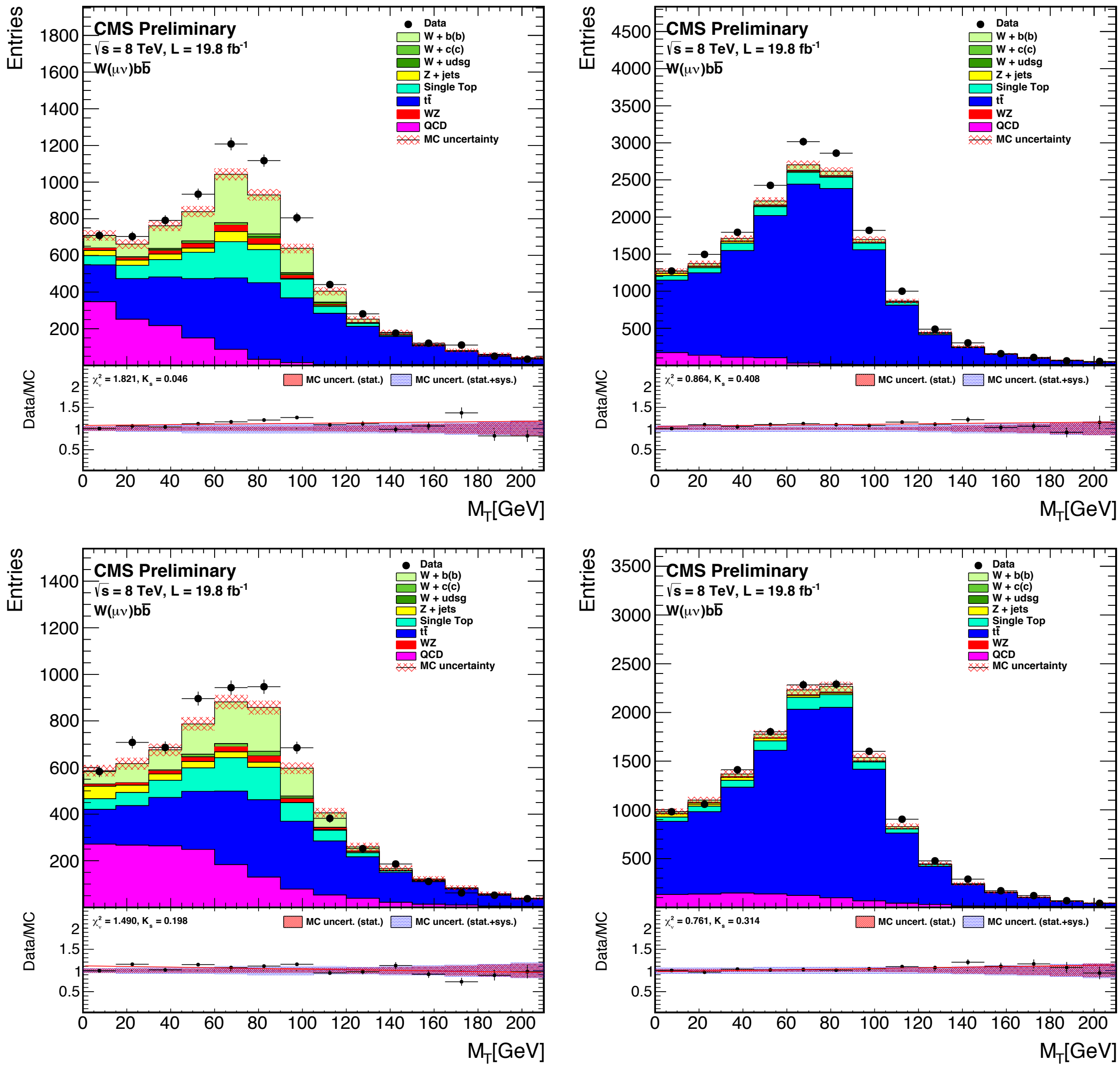

SLIKA 9.1: Distribucije transverzne mase za mionski (*gore*) i elektronski (*dolje*) za signalno područje i kontrolno područje dominitanu top kvark pozadinom.

U konačnoj prilagodbi svi doprinosi variraju unutar neodređenosti osim signala koji je slobodan. Konačni rezultat, iskazan kao omjer mjerenog udarnog presjeka i teorijskog predviđanja (*signal strength*), označava se sa μ i iznosi:

$$\mu_{mu} = 1.37 \pm 0.07(\text{stat.}) \pm 0.20(\text{syst.})$$
$$\mu_{ele} = 1.67 \pm 0.08(\text{stat.}) \pm 0.27(\text{syst.})$$

Korištenjem relacije 9.2 može se sada odrediti udarni presjek. Broj događaja signala je definiran kao broj događaja prije prilagodbe pomnožen s μ. Aktivni dio detektora i efikasnost se uzimaju iz tablice 9.1, a integrirani luminozitet iznosi 19.8 fb^{-1}. Dobiveni vrijednost udarnog presjeka je:

$$\sigma(pp \to W + bb) \times \mathcal{B}(W \to \mu\nu) = 0.66 \pm 0.03(\text{stat.}) \pm 0.10(\text{syst.})$$
$$\sigma(pp \to W + bb) \times \mathcal{B}(W \to e\nu) = 0.78 \pm 0.04(\text{stat.}) \pm 0.13(\text{syst.})$$

Navedeni rezultati uključuju sve prethodno navedene sistematske neodređenosti. Međutim, u obzir nisu uključene sistematske neodređenosti na određivanje aktivnog dijela detektora i efikasnosti prilikom različitog odabira partonske distribucijske funkcije i varijacije renormalizacijske i faktorizacijske skale.

Teorijsko predviđanje određeno je MCFM paketom na NLO preciznost s faktorizacijskom i renormalizacijskom skalom postavljenom na masu W bozona. Uzimajući u obzir i doprinos događaja u kojima su se sudarila po dva partona iz svakog protona (*Double parton scattering - DPS*) [32], udarni presjek tada iznosi:

$$\sigma_{TH}(pp \to W + bb) \times \mathcal{B}(W \to l\nu) = 0.55 \pm 0.03(\text{theor.}) \pm 0.02(\text{DPS})\ \text{pb}.$$

9.8 Zaključak

Ova teza predstavlje rezultate mjerenja udarnog presjeka za produkciju W bozona zajedno s parom mlazova nastalih iz b kvarka u sudarima protona na energiji $\sqrt{s} = 8$ TeV. Podaci su prikupljeni 2012. godine CMS detektorom i odgovaraju integriranom luminozitetu od 19.8 fb^{-1}. Udarni presjek je mjeren posebno u elektronskom i mionskom kanalu, a dva su rezultata kompatibilna unutar neodređenosti. Teorijsko predviđanje za ovaj proces izračunato je pomoću MCFM paketa. Mjerena vrijednost je za jednu standardnu devijaciju viša od predviđene teorijske vrijednosti. Neodređenost mjerenja udarnog presjeka je dominirana sistematskim pogreškama, prvenstveno neodređenošću identifikacije b mlazova. Smanjanje ovih efekata bi omogućilo testiranje predviđanja perturbativne kromodinamike. Daljnja istraživanja ovog i sličnih procesa uključuju i mjerenje diferencijalnog udarnog predjeka u ovisnosti o npr. transverzalnom impulsu vodećeg b mlaza što bi dovelo do unapređenja torijskih modela. Nadalje, mogu se proučavati i stanja u kojim su dva B hadrona u istom mlazu što bi dovelo do boljeg razumijevanja kolinearnih konačnih stanja.

Appendix A

Lorentz angle measurement in Pixel detector

Lorentz angle measurement was performed regularly during 2011 and 2012. This parameter is used in reconstruction to estimate charge sharing and improve the overall resolution of the Pixel detector. The results presented here were obtained using 2012 collision data and early 2015 cosmics data.

A.1 Grazing angle method

Lorentz angle is measured by using the grazing angle method described in detail in [78]. From the individual signals in the detector, using reconstruction algorithms, tracks of muon candidates are obtained. From these reconstructed track it is possible to extract the entry point (x_{reco},y_{reco}) to each layer of the detector. Distance between reconstructed entry point and the actual hit in the detector is then defined as (Δx,Δy):

$$\Delta x = x_{center} - x_{reco} \tag{A.1}$$

$$\Delta y = y_{center} - y_{reco} \tag{A.2}$$

where (x_{center},y_{center}) is the position of each individual pixel center in the observed cluster. Drift of the electrons can be determined using three impact angles defined in the following way:

$$\tan\alpha = \frac{p_z}{p_x} \tag{A.3}$$

$$\tan\beta = \frac{p_z}{p_y} \tag{A.4}$$

$$\tan\gamma = \frac{p_x}{p_y} \tag{A.5}$$

where p_x,p_y and p_z are momentum components in local coordinate system which are calculated from reconstructed track parameters (Fig. A.1).

Drift of the electrons depends on the depth at which electrons are created. Depth of the

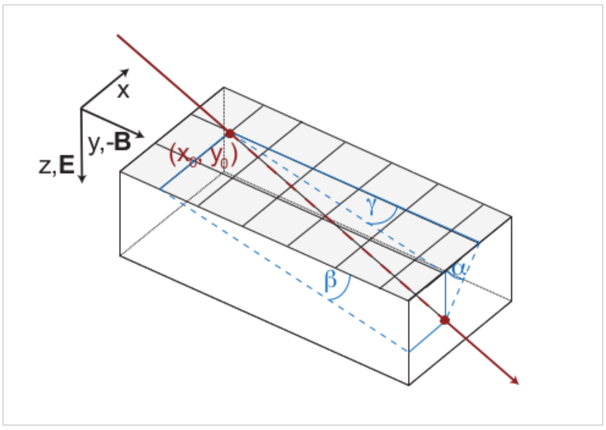

FIGURE A.1: Angle definitions for grazing angle method.

electron production z and drift due to magnetic field d are defined:

$$z = \Delta y \tan\beta \tag{A.6}$$

$$d = \Delta x - \Delta y \tan\gamma \tag{A.7}$$

This procedure is repeated for each pixel over many tracks in order to obtain charge drift distance vs depth. The Lorentz angle is the slope of this distribution. Without a magnetic field, the direction of the clusters largest extension is parallel to the track projection on the (x, y) plane. The average drift distance of an electron created at a certain depth is obtained from Fig. A.2. A linear fit is performed over the total depth of the detector excluding the first and last 50 μ where the charge drift is systematically displaced by the finite size of the pixel cell (Fig:A.3).

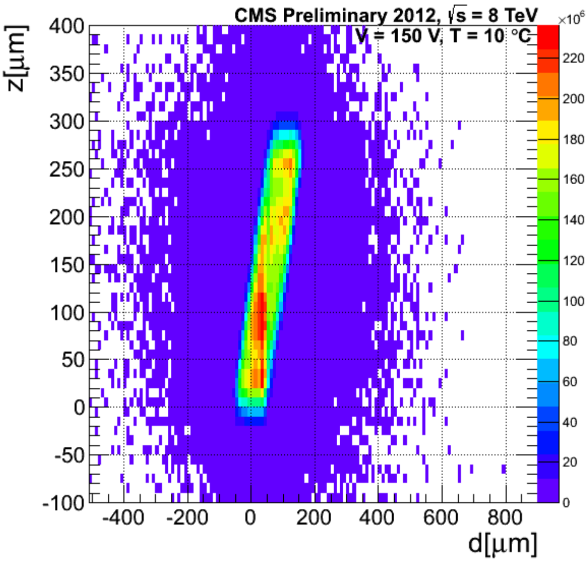

FIGURE A.2: Depth at which electrons in silicon bulk were produced as a function of Lorentz drift.

In order to obtain a good measurement, it is important to use clean tracks. Therefore, it required to have a well reconstructed muon tracks with $p_T > 3$GeV and $\chi^2/ndof < 2$ which are required to have shallow impact angle with respect to local y direction with cluster size of at least 4 pixels in this direction. Summary of the selection criteria can be found in table A.1.

TABLE A.1: Selection criteria for Lorentz angle measurement

Cluster size in y	> 3
Track p_t	> 3GeV/c
χ^2/ndof	< 2
Hit residuals	$< 50\mu m$
Cluster charge	< 120000e

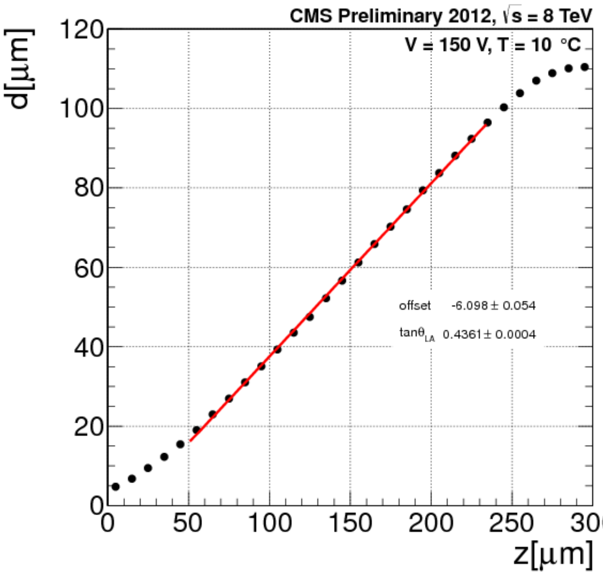

FIGURE A.3: The average drift of electrons as a function of the production depth. Slope of the linear fit result is the $tan\theta_L$.

Figure A.4 shows how Lorentz angle changes with integrated luminosity. Results are shown for 23fb^{-1} of delivered luminosity in 2012. Increase in Lorentz angle measured with grazing angle method has been observed in all layers, with largest effect (6%) visible in layer 1 over this period of data taking.

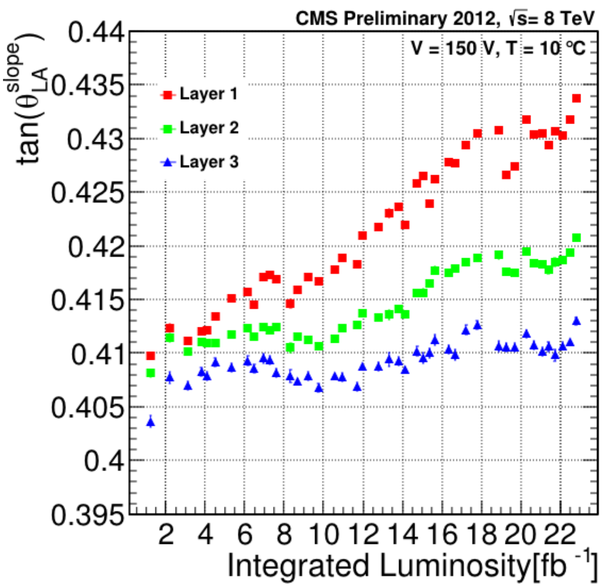

FIGURE A.4: Lorentz angle as a function of integrated luminosity for 2012.

A.2 Minimum cluster size method (V-method)

The pixel cluster size in the drift direction depends on the incident angle and is minimal when incident angle is equal to the Lorentz angle. Thus, measuring the average cluster size in drift direction as a function of incident angle and obtaining a minimum of that distribution is an alternative and direct method of measuring the Lorentz angle. The method is usually referred to as V-method due to a shape of distribution which in the simple case can be approximated with formula

$$p_1 * abs(tan(\theta) - p_0) + p_2 \tag{A.8}$$

where p_0, p_1 and p_2 are parameters obtained from the fit and $p_0 = tan(\theta_{LA})$.

The method was successfully applied to cosmic muon tracks during CMS commissioning period in 2008 and again in 2015. The fit result is shown in figure A.5.

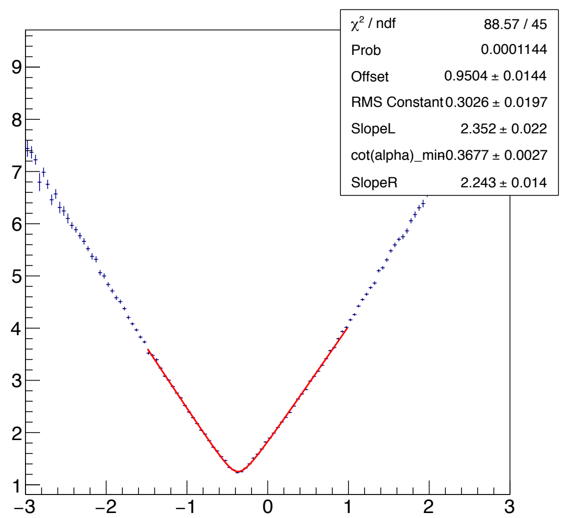

FIGURE A.5: An example of V-method fit.

Application to collision data is more challenging. Coordinates of a track passing through the detector, its incoming angle, and its p_T are correlated and therefore incoming angles from collision tracks have limited range. With standard running conditions the value of Lorentz angle is at the edge of that range where tracks with very low p_T (<0.5 GeV) dominate. Because of that average cluster size as a function of incoming angle cannot be described by a simple model like above mentioned for cosmic data. While results for collision data obtained with V-method are in general agreement with the default calculation, the uncertainty of the method at present is too big to be used as a viable alternative.

Bibliography

[1] Sheldon L. Glashow. Partial-symmetries of weak interactions. *Nuclear Physics*, 22(4):579 – 588, 1961. ISSN 0029-5582. doi: http://dx.doi.org/10.1016/0029-5582(61)90469-2. URL http://www.sciencedirect.com/science/article/pii/0029558261904692.

[2] Steven Weinberg. A model of leptons. *Phys. Rev. Lett.*, 19:1264–1266, Nov 1967. doi: 10.1103/PhysRevLett.19.1264. URL http://link.aps.org/doi/10.1103/PhysRevLett.19.1264.

[3] Abdus Salam. Weak and Electromagnetic Interactions. *Conf.Proc.*, C680519:367–377, 1968.

[4] G. Arnison et al. Experimental observation of isolated large transverse energy electrons with associated missing energy at s=540 gev. *Physics Letters B*, 122(1):103 – 116, 1983. ISSN 0370-2693. doi: http://dx.doi.org/10.1016/0370-2693(83)91177-2. URL http://www.sciencedirect.com/science/article/pii/0370269383911772.

[5] G. Arnison et al. Experimental observation of lepton pairs of invariant mass around 95 gev/c2 at the cern sps collider. *Physics Letters B*, 126(5):398–410, 1983. doi: 10.1016/0370-2693(83)90188-0. URL http://www.scopus.com/inward/record.url?eid=2-s2.0-23044516930&partnerID=40&md5=8be07e2a211517aafdf5135170ca9591.

[6] Georges Aad et al. Observation of a new particle in the search for the Standard Model Higgs boson with the ATLAS detector at the LHC. *Phys.Lett.*, B716:1–29, 2012. doi: 10.1016/j.physletb.2012.08.020.

[7] Serguei Chatrchyan et al. Observation of a new boson at a mass of 125 GeV with the CMS experiment at the LHC. *Phys.Lett.*, B716:30–61, 2012. doi: 10.1016/j.physletb.2012.08.021.

[8] D. Griffiths. *Introduction to Elementary Particles*. John Wiley & Sons, New York, USA, 1987.

[9] Makoto Kobayashi and Toshihide Maskawa. CP Violation in the Renormalizable Theory of Weak Interaction. *Prog.Theor.Phys.*, 49:652–657, 1973. doi: 10.1143/PTP.49.652.

[10] Bernard Aubert et al. Measurement of CP violating asymmetries in B^0 decays to CP eigenstates. *Phys.Rev.Lett.*, 86:2515–2522, 2001. doi: 10.1103/PhysRevLett.86.2515.

[11] K. Abe et al. Observation of large CP violation in the neutral B meson system. *Phys.Rev.Lett.*, 87:091802, 2001. doi: 10.1103/PhysRevLett.87.091802.

[12] S. W. Herb, D. C. Hom, L. M. Lederman, J. C. Sens, H. D. Snyder, J. K. Yoh, J. A. Appel, B. C. Brown, C. N. Brown, W. R. Innes, K. Ueno, T. Yamanouchi, A. S. Ito, H. Jöstlein, D. M. Kaplan, and R. D. Kephart. Observation of a dimuon resonance at 9.5 gev in 400-gev proton-nucleus collisions. *Phys. Rev. Lett.*, 39:252–255, Aug 1977. doi: 10.1103/PhysRevLett.39.252. URL http://link.aps.org/doi/10.1103/PhysRevLett.39.252.

[13] G. Arnison et al. Experimental Observation of Isolated Large Transverse Energy Electrons with Associated Missing Energy at s**(1/2) = 540-GeV. *Phys.Lett.*, B122:103–116, 1983. doi: 10.1016/0370-2693(83)91177-2.

[14] M. Banner et al. Observation of Single Isolated Electrons of High Transverse Momentum in Events with Missing Transverse Energy at the CERN anti-p p Collider. *Phys.Lett.*, B122:476–485, 1983. doi: 10.1016/0370-2693(83)91605-2.

[15] Michelangelo L. Mangano. Production of W plus heavy quark pairs in hadronic collisions. *Nucl.Phys.*, B405:536–554, 1993. doi: 10.1016/0550-3213(93)90558-7.

[16] Serguei Chatrchyan et al. Search for the standard model Higgs boson produced in association with a W or a Z boson and decaying to bottom quarks. *Phys.Rev.*, D89 (1):012003, 2014. doi: 10.1103/PhysRevD.89.012003.

[17] Serguei Chatrchyan et al. Evidence for the direct decay of the 125 GeV Higgs boson to fermions. *Nature Phys.*, 10:557–560, 2014. doi: 10.1038/nphys3005.

[18] Vardan Khachatryan et al. Precise determination of the mass of the Higgs boson and tests of compatibility of its couplings with the standard model predictions using proton collisions at 7 and 8 TeV. *Eur.Phys.J.*, C75(5):212, 2015. doi: 10.1140/epjc/s10052-015-3351-7.

[19] Serguei Chatrchyan et al. Search for supersymmetry in final states with a single lepton, b-quark jets, and missing transverse energy in proton-proton collisions at $\sqrt{s} = 7$ TeV. *Phys.Rev.*, D87(5):052006, 2013. doi: 10.1103/PhysRevD.87.052006.

[20] T. Gleisberg, Stefan. Hoeche, F. Krauss, M. Schonherr, S. Schumann, et al. Event generation with SHERPA 1.1. *JHEP*, 0902:007, 2009. doi: 10.1088/1126-6708/2009/02/007.

[21] K.A. Olive et al. Review of Particle Physics. *Chin.Phys.*, C38:090001, 2014. doi: 10.1088/1674-1137/38/9/090001.

[22] John M. Campbell, J.W. Huston, and W.J. Stirling. Hard Interactions of Quarks and Gluons: A Primer for LHC Physics. *Rept.Prog.Phys.*, 70:89, 2007. doi: 10.1088/0034-4885/70/1/R02.

[23] A.D. Martin, W.J. Stirling, R.S. Thorne, and G. Watt. Parton distributions for the LHC. *Eur.Phys.J.*, C63:189–285, 2009. doi: 10.1140/epjc/s10052-009-1072-5.

[24] Michael Edward Peskin and Daniel V. Schroeder. *An introduction to quantum field theory*. Advanced book program. Westview Press Reading (Mass.), Boulder (Colo.), 1995. ISBN 0-201-50934-2. URL http://opac.inria.fr/record=b1131978.

[25] Fabio Maltoni, Giovanni Ridolfi, and Maria Ubiali. b-initiated processes at the LHC: a reappraisal. *JHEP*, 1207:022, 2012. doi: 10.1007/JHEP04(2013)095,10.1007/JHEP07(2012)022.

[26] R. Keith Ellis and Sinisa Veseli. Strong radiative corrections to W b anti-b production in p anti-p collisions. *Phys.Rev.*, D60:011501, 1999. doi: 10.1103/PhysRevD.60.011501.

[27] Michelangelo L. Mangano, Mauro Moretti, and Roberto Pittau. Multijet matrix elements and shower evolution in hadronic collisions: $Wb\bar{b}+n$ jets as a case study. *Nucl.Phys.*, B632:343–362, 2002. doi: 10.1016/S0550-3213(02)00249-3.

[28] F. Febres Cordero, L. Reina, and D. Wackeroth. NLO QCD corrections to W boson production with a massive b-quark jet pair at the Tevatron p anti-p collider. *Phys.Rev.*, D74:034007, 2006. doi: 10.1103/PhysRevD.74.034007.

[29] Seth Quackenbush, Edmond L. Berger, C.B. Jackson, and Gabe Shaughnessy. LHC Sensitivity to $Wb\bar{b}$ Production via Double Parton Scattering. 2011.

[30] Jonathan R. Gaunt and W. James Stirling. Double Parton Distributions Incorporating Perturbative QCD Evolution and Momentum and Quark Number Sum Rules. *JHEP*, 1003:005, 2010. doi: 10.1007/JHEP03(2010)005.

[31] Sunil Bansal, Paolo Bartalini, Boris Blok, Diego Ciangottini, Markus Diehl, et al. Progress in Double Parton Scattering Studies. 2014.

[32] Serguei Chatrchyan et al. Study of double parton scattering using W + 2-jet events in proton-proton collisions at $\sqrt{s}=7$ TeV. *JHEP*, 1403:032, 2014. doi: 10.1007/JHEP03(2014)032.

[33] Serguei Chatrchyan et al. Measurement of the production cross section for a W boson and two b jets in pp collisions at $\sqrt{s}$=7 TeV. *Phys.Lett.*, B735:204–225, 2014. doi: 10.1016/j.physletb.2014.06.041.

[34] T. Aaltonen et al. First Measurement of the b-jet Cross Section in Events with a W Boson in p anti-p Collisions at s**(1/2) = 1.96-TeV. *Phys.Rev.Lett.*, 104:131801, 2010. doi: 10.1103/PhysRevLett.104.131801.

[35] V.M. Abazov et al. Measurement of the $p\bar{p} \to W + b + X$ production cross section at $\sqrt{s} = 1.96$ TeV. *Phys.Lett.*, B718:1314–1320, 2013. doi: 10.1016/j.physletb.2012.12.044.

[36] Georges Aad et al. Measurement of the cross-section for W boson production in association with b-jets in pp collisions at $\sqrt{s} = 7$ TeV with the ATLAS detector. *JHEP*, 1306:084, 2013. doi: 10.1007/JHEP06(2013)084.

[37] S. Chatrchyan et al. The CMS experiment at the CERN LHC. *JINST*, 3:S08004, 2008. doi: 10.1088/1748-0221/3/08/S08004.

[38] G. Aad et al. The ATLAS Experiment at the CERN Large Hadron Collider. *JINST*, 3:S08003, 2008. doi: 10.1088/1748-0221/3/08/S08003.

[39] K. Aamodt et al. The ALICE experiment at the CERN LHC. *JINST*, 3:S08002, 2008. doi: 10.1088/1748-0221/3/08/S08002.

[40] Jr. Alves, A. Augusto et al. The LHCb Detector at the LHC. *JINST*, 3:S08005, 2008. doi: 10.1088/1748-0221/3/08/S08005.

[41] Lyndon Evans and Philip Bryant. LHC Machine. *JINST*, 3:S08001, 2008. doi: 10.1088/1748-0221/3/08/S08001.

[42] Oliver Sim Brüning, Paul Collier, P Lebrun, Stephen Myers, Ranko Ostojic, John Poole, and Paul Proudlock. *LHC Design Report*. CERN, Geneva, 2004.

[43] Absolute Calibration of the Luminosity Measurement at CMS: Winter 2012 Update. Technical Report CMS-PAS-SMP-12-008, CERN, Geneva, 2012. URL https://cds.cern.ch/record/1434360.

[44] CMS Collaboration. CMS Luminosity Based on Pixel Cluster Counting - Summer 2013 Update. Technical Report CMS-PAS-LUM-13-001, 2013.

[45] CMS Collaboration. Particle-Flow Event Reconstruction in CMS and Performance for Jets, Taus, and MET. CMS Physics Analysis Summary CMS-PAS-PFT-09-001, 2009.

[46] W. Adam, R. Frühwirth, A. Strandlie, and T. Todorov. RESEARCH NOTE FROM COLLABORATION: Reconstruction of electrons with the Gaussian-sum filter in the CMS tracker at the LHC. *Journal of Physics G Nuclear Physics*, 31:9, September 2005. doi: 10.1088/0954-3899/31/9/N01.

[47] CMS Collaboration. Electron reconstruction and identification at sqrt(s) = 7 TeV. CMS Physics Analysis Summary CMS-PAS-EGM-10-004, 2010.

[48] R. Frühwirth. Application of kalman filtering to track and vertex fitting. *Nuclear Instruments and Methods in Physics Research Section A: Accelerators, Spectrometers, Detectors and Associated Equipment*, 262(2–3):444 – 450, 1987. ISSN 0168-9002. doi: http://dx.doi.org/10.1016/0168-9002(87)90887-4. URL http://www.sciencedirect.com/science/article/pii/0168900287908874.

[49] The CMS Collaboration. Performance of CMS muon reconstruction in pp collision events at $\sqrt{s} = 7$ TeV. *Journal of Instrumentation*, 7:2P, October 2012. doi: 10.1088/1748-0221/7/10/P10002.

[50] Gavin P. Salam. Towards Jetography. *Eur.Phys.J.*, C67:637–686, 2010. doi: 10.1140/epjc/s10052-010-1314-6.

[51] Matteo Cacciari, Gavin P. Salam, and Gregory Soyez. The Anti-k(t) jet clustering algorithm. *JHEP*, 0804:063, 2008. doi: 10.1088/1126-6708/2008/04/063.

[52] Serguei Chatrchyan et al. Determination of Jet Energy Calibration and Transverse Momentum Resolution in CMS. *JINST*, 6:P11002, 2011. doi: 10.1088/1748-0221/6/11/P11002.

[53] CMS Collaboration. Pileup subtraction using jet areas. *Physics Letters B*, 659(1–2):119 – 126, 2008. ISSN 0370-2693. doi: http://dx.doi.org/10.1016/j.physletb.2007.09.077. URL http://www.sciencedirect.com/science/article/pii/S0370269307011094.

[54] CMS Collaboration. 8 TeV Jet Energy Corrections and Uncertainties based on 19.8 fb^{-1} of data in CMS. Technical report, Oct 2013. URL http://cds.cern.ch/record/1627305.

[55] Matteo Cacciari, Gavin P. Salam, and Gregory Soyez. FastJet User Manual. *Eur.Phys.J.*, C72:1896, 2012. doi: 10.1140/epjc/s10052-012-1896-2.

[56] Serguei Chatrchyan et al. Identification of b-quark jets with the CMS experiment. *JINST*, 8:P04013, 2013. doi: 10.1088/1748-0221/8/04/P04013.

[57] CMS Collaboration. Performance of b tagging at sqrt(s)=8 TeV in multijet, ttbar and boosted topology events. CMS Physics Analysis Summary CMS-PAS-BTV-13-001, 2013.

[58] The CMS collaboration. Identification of b-quark jets with the cms experiment. *Journal of Instrumentation*, 8(04):P04013, 2013. URL http://stacks.iop.org/1748-0221/8/i=04/a=P04013.

[59] Particle-Flow Event Reconstruction in CMS and Performance for Jets, Taus, and MET. Technical Report CMS-PAS-PFT-09-001, CERN, 2009. Geneva, Apr 2009. URL http://cds.cern.ch/record/1194487.

[60] Serguei Chatrchyan et al. Missing transverse energy performance of the CMS detector. *JINST*, 6:P09001, 2011. doi: 10.1088/1748-0221/6/09/P09001.

[61] Torbjorn Sjostrand, Stephen Mrenna, and Peter Z. Skands. PYTHIA 6.4 Physics and Manual. *JHEP*, 0605:026, 2006. doi: 10.1088/1126-6708/2006/05/026.

[62] Torbjorn Sjostrand, Stephen Mrenna, and Peter Z. Skands. A Brief Introduction to PYTHIA 8.1. *Comput.Phys.Commun.*, 178:852–867, 2008. doi: 10.1016/j.cpc.2008.01.036.

[63] Rick Field. Early LHC Underlying Event Data - Findings and Surprises. 2010.

[64] Serguei Chatrchyan et al. Jet and underlying event properties as a function of charged-particle multiplicity in proton–proton collisions at $\sqrt{s} = 7$ TeV. *Eur.Phys.J.*, C73(12):2674, 2013. doi: 10.1140/epjc/s10052-013-2674-5.

[65] Johan Alwall, Michel Herquet, Fabio Maltoni, Olivier Mattelaer, and Tim Stelzer. MadGraph 5 : Going Beyond. *JHEP*, 1106:128, 2011. doi: 10.1007/JHEP06(2011)128.

[66] John M. Campbell and R.K. Ellis. MCFM for the Tevatron and the LHC. *Nucl.Phys.Proc.Suppl.*, 205-206:10–15, 2010. doi: 10.1016/j.nuclphysbps.2010.08.011.

[67] J. Alwall, R. Frederix, S. Frixione, V. Hirschi, F. Maltoni, et al. The automated computation of tree-level and next-to-leading order differential cross sections, and their matching to parton shower simulations. *JHEP*, 1407:079, 2014. doi: 10.1007/JHEP07(2014)079.

[68] Carlo Oleari. The POWHEG-BOX. *Nucl.Phys.Proc.Suppl.*, 205-206:36–41, 2010. doi: 10.1016/j.nuclphysbps.2010.08.016.

[69] S. Jadach, Z. Was, R. Decker, and Johann H. Kuhn. The tau decay library TAUOLA: Version 2.4. *Comput.Phys.Commun.*, 76:361–380, 1993. doi: 10.1016/0010-4655(93)90061-G.

[70] S. Agostinelli et al. GEANT4: A Simulation toolkit. *Nucl.Instrum.Meth.*, A506:250–303, 2003. doi: 10.1016/S0168-9002(03)01368-8.

[71] R. Brun and F. Rademakers. ROOT: An object oriented data analysis framework. *Nucl.Instrum.Meth.*, A389:81–86, 1997. doi: 10.1016/S0168-9002(97)00048-X.

[72] CMS Collaboration. Combination of ATLAS and CMS top quark pair cross section measurements in the emu final state using proton-proton collisions at 8 TeV. CMS Physics Analysis Summary CMS-PAS-TOP-14-016, 2014.

[73] CMS Collaboration. Pileup Jet Identification. CMS Physics Analysis Summary CMS-PAS-JME-13-005, 2013.

[74] The CMS collaboration. Performance of cms muon reconstruction in pp collision events at $\sqrt{s} = 7$ tev. *Journal of Instrumentation*, 7(10):P10002, 2012. URL http://stacks.iop.org/1748-0221/7/i=10/a=P10002.

[75] Procedure for the LHC Higgs boson search combination in summer 2011. Technical Report ATL-PHYS-PUB-2011-011, CERN, Geneva, Aug 2011. URL https://cds.cern.ch/record/1375842.

[76] CMS Luminosity Based on Pixel Cluster Counting - Summer 2013 Update. Technical Report CMS-PAS-LUM-13-001, CERN, Geneva, 2013. URL http://cds.cern.ch/record/1598864.

[77] Ryan Gavin, Ye Li, Frank Petriello, and Seth Quackenbush. W Physics at the LHC with FEWZ 2.1. *Comput.Phys.Commun.*, 184:208–214, 2013. doi: 10.1016/j.cpc.2012.09.005.

[78] B Henrich and R Kaufmann. Lorentz-angle in irradiated silicon. *Nucl. Instrum. Methods Phys. Res., A*, 477(1-3):304–307, 2002.

Curriculum vitae

Personal

Name	Jelena Luetić
Address	Supilova 7, 10000 Zagreb, Croatia
Date of Birth	April 5, 1987
Place of birth	Split, Croatia
Citizenship	Croatian
Phone	+385 91 1480103
Email	jelena.luetic@cern.ch
Languages	English, basic Italian and French, Croatian - native

Education

2011 -	**PhD**, Faculty of Science, Physics department *Title*: Measurement of the cross section for associated production of a W boson and two b quarks with the CMS detector at the Large Hadron Collider *Advisor:* Prof. Vuko Brigljević, thesis defence is scheduled for July, 15th 2015.
2005 - 2010	**MSc**, Faculty of Science, Physics department *Title*: Measurement of Z boson cross section in proton-proton collisions with CMS detector at Large Hadron Collider *Advisor:* Prof. Ivica Puljak, thesis defended on November, 30th 2010.

Professional experience

Since 2009 I've been a part of the CMS group at Ruđer Bošković Institute, working on gauge boson produced in association with jets measurements and on technical aspects of CMS detector:

- One of the main contributors to Wbb cross section measurement at $\sqrt{s} = 8$ TeV. Collaboration with University of Wisconsin-Madison, University of Trieste and CERN.
- Responsible for Lorentz angle monitoring and calibration for CMS Pixel detector.
- Responsible for development and maintenance of technical tools used in the offline analysis shared with other members of CMS Pixel group.
- Participated in pixel detector recommissioning during the long shutdown.
- Paricipated in CMS Pixel Operations

Teaching

2011 - 2015	Faculty of Science, Zagreb, Croatia Teaching assistant in 2 courses - *Introductory laboratory exercises* (2011.- 2012.) and *Programming in C* (2011.-2015.)
2010 - 2011	Faculty of Electrical Engineering, Mechanical Engineering and Naval Architecture in Split, Croatia Teaching assistant - *Laboratory exercises in Modern physics*

Schools and Conferences

2009	CERN Summer Student Programme, Geneva, Switzerland
2010	CERN School of Computing, London, UK
2011	CMSDAS - Data analysis school, Pisa, Italy
2012	Silicon Detector Workshop, Split, Croatia *Talk:* Lorentz angle measurement in CMS Pixel detector
2013	EDIT - Excellence in Detectors, Tsukuba, Japan *Poster*: CMS Pixel detector and Lorentz angle determination
2014	Fermilab - CERN Hadron Collider School, Fermilab, USA

Computer skills

- Computer languages: C, C++, Fortran, Python
- Software: ROOT, Mathematica, LabView

Other

Participation in various physics and science outreach programs:

- Organization of International Masterclasses: lectures and laboratory exercises for high school students covering various topics in high energy physics.
- Participated in several science fairs for general public demonstrating experiments.

Publications

1. **"Combined Measurement of the Higgs Boson Mass in *pp* Collisions at $\sqrt{s} = 7$ and 8 TeV with the ATLAS and CMS Experiments"**, G. Aad *et al.* [ATLAS and CMS Collaborations], Phys. Rev. Lett. **114**191803 (2015)

2. **"Search for vector-like T quarks decaying to top quarks and Higgs bosons in the all-hadronic channel using jet substructure"**, V. Khachatryan *et al.* [CMS Collaboration], JHEP **1506**080 (2015)

3. **"Study of final-state radiation in decays of Z bosons produced in *pp* collisions at 7 TeV"**, V. Khachatryan *et al.* [CMS Collaboration], Phys. Rev. D **91**no. 9092012 (2015)

4. **"Search for physics beyond the standard model in events with two leptonsjetsand missing transverse momentum in pp collisions at sqrt(s) = 8 TeV"**, V. Khachatryan *et al.* [CMS Collaboration], JHEP **1504**124 (2015)

5. **"Measurement of the Zγ production cross section in pp collisions at 8 TeV and search for anomalous triple gauge boson couplings"**, V. Khachatryan *et al.* [CMS Collaboration], JHEP **1504**164 (2015)

6. **"Nuclear effects on the transverse momentum spectra of charged particles in pPb collisions at $\sqrt{s_{\rm NN}} = 5.02$ TeV"**, V. Khachatryan *et al.* [CMS Collaboration], Eur. Phys. J. C **75**no. 5237 (2015)

7. **"Searches for supersymmetry using the M$_{T2}$ variable in hadronic events produced in pp collisions at 8 TeV"**, V. Khachatryan *et al.* [CMS Collaboration], JHEP **1505**078 (2015)

8. **"Measurement of J/ψ and ψ(2S) Prompt Double-Differential Cross Sections in pp Collisions at $\sqrt{s}$=7 TeV"**, V. Khachatryan *et al.* [CMS Collaboration], Phys. Rev. Lett. **114**no. 19191802 (2015)

9. **"Performance of electron reconstruction and selection with the CMS detector in proton-proton collisions at $\sqrt{s} = 8$ TeV"**, V. Khachatryan *et al.* [CMS Collaboration], JINST **10**no. 06P06005 (2015)

10. **"Search for a standard model Higgs boson produced in association with a top-quark pair and decaying to bottom quarks using a matrix element method"**, V. Khachatryan *et al.* [CMS Collaboration], Eur. Phys. J. C **75**no. 6251 (2015)

11. **"Search for supersymmetry using razor variables in events with *b*-tagged jets in *pp* collisions at $\sqrt{s} = 8$ TeV"**, V. Khachatryan *et al.* [CMS Collaboration], Phys. Rev. D **91**052018 (2015)

12. **"Search for decays of stopped long-lived particles produced in proton–proton collisions at $\sqrt{s} = 8\,\mathrm{TeV}$"**, V. Khachatryan *et al.* [CMS Collaboration], Eur. Phys. J. C **75**no. 4151 (2015)

13. **"Search for resonances and quantum black holes using dijet mass spectra in proton-proton collisions at $\sqrt{s}$ = 8 TeV"**, V. Khachatryan *et al.* [CMS Collaboration], Phys. Rev. D **91**no. 5052009 (2015)

14. **"Precise determination of the mass of the Higgs boson and tests of compatibility of its couplings with the standard model predictions using proton collisions at 7 and 8 TeV"**, V. Khachatryan *et al.* [CMS Collaboration], Eur. Phys. J. C **75**no. 5212 (2015)

15. **"Search for pair-produced resonances decaying to jet pairs in proton-proton collisions at sqrt(s) = 8 TeV"**, V. Khachatryan *et al.* [CMS Collaboration], Phys. Lett. B **747**98 (2015)

16. **"Search for physics beyond the standard model in dilepton mass spectra in proton-proton collisions at** $\sqrt{s}$ = 8 **TeV"**, V. Khachatryan *et al.* [CMS Collaboration], JHEP **1504**025 (2015)

17. **"Searches for supersymmetry based on events with b jets and four W bosons in pp collisions at 8 TeV"**, V. Khachatryan *et al.* [CMS Collaboration], Phys. Lett. B **745**5 (2015)

18. **"Measurement of the inclusive 3-jet production differential cross section in proton–proton collisions at 7 TeV and determination of the strong coupling constant in the TeV range"**, V. Khachatryan *et al.* [CMS Collaboration], Eur. Phys. J. C **75**no. 5186 (2015)

19. **"Measurements of differential and double-differential Drell-Yan cross sections in proton-proton collisions at 8 TeV"**, V. Khachatryan *et al.* [CMS Collaboration], Eur. Phys. J. C **75**no. 4147 (2015)

20. **"Search for stealth supersymmetry in events with jetseither photons or leptonsand low missing transverse momentum in pp collisions at 8 TeV"**, V. Khachatryan *et al.* [CMS Collaboration], Phys. Lett. B **743**503 (2015)

21. **"Search for long-lived particles that decay into final states containing two electrons or two muons in proton-proton collisions at $\sqrt{s}$ = 8 TeV"**, V. Khachatryan *et al.* [CMS Collaboration], Phys. Rev. D **91**no. 5052012 (2015)

22. **"Search for long-lived neutral particles decaying to quark-antiquark pairs in proton-proton collisions at $\sqrt{s}$ = 8 TeV"**, V. Khachatryan *et al.* [CMS Collaboration], Phys. Rev. D **91**no. 1012007 (2015)

23. **"Search for disappearing tracks in proton-proton collisions at** $\sqrt{s}$ = 8 **TeV"**, V. Khachatryan *et al.* [CMS Collaboration], JHEP **1501**096 (2015)

24. **"Measurement of the cross section ratio $\sigma_{tt b\bar{b}}/\sigma_{ttjj}$ in pp collisions at $\sqrt{s} =$ 8 TeV"**, V. Khachatryan *et al.* [CMS Collaboration], Phys. Lett. B **746**132 (2015)

25. **"Observation of the rare $B^0_s \to \mu^+\mu^-$ decay from the combined analysis of CMS and LHCb data"**, V. Khachatryan *et al.* [CMS and LHCb Collaborations], Nature **522**68 (2015)

26. **"Search for quark contact interactions and extra spatial dimensions using dijet angular distributions in proton–proton collisions at $\sqrt{s} = 8$ TeV"**, V. Khachatryan *et al.* [CMS Collaboration], Phys. Lett. B **746**79 (2015)

27. **"Performance of the CMS missing transverse momentum reconstruction in pp data at $\sqrt{s} = 8$ TeV"**, V. Khachatryan *et al.* [CMS Collaboration], JINST **10**no. 02P02006 (2015)

28. **"Constraints on parton distribution functions and extraction of the strong coupling constant from the inclusive jet cross section in pp collisions at $\sqrt{s} = 7$ TeV"**, V. Khachatryan *et al.* [CMS Collaboration], Eur. Phys. J. C **75**no. 6288 (2015)

29. **"Search for a standard model−like Higgs boson in the $\mu^+\mu^-$ and e^+e^- decay channels at the LHC"**, V. Khachatryan *et al.* [CMS Collaboration], Phys. Lett. B **744**184 (2015)

30. **"Study of vector boson scattering and search for new physics in events with two same-sign leptons and two jets"**, V. Khachatryan *et al.* [CMS Collaboration], Phys. Rev. Lett. **114**no. 5051801 (2015)

31. **"Measurement of the ratio of the production cross sections times branching fractions of $B^\pm_c \to J/\psi\pi^\pm$ and $B^\pm \to J/\psi K^\pm$ and $\mathcal{B}(B^\pm_c \to J/\psi\pi^\pm\pi^\pm\pi^\mp)/\mathcal{B}(B^\pm_c \to J/\psi\pi^\pm)$ in pp collisions at $\sqrt{s} = 7$ TeV"**, V. Khachatryan *et al.* [CMS Collaboration], JHEP **1501**063 (2015)

32. **"Study of Z production in PbPb and pp collisions at $\sqrt{s_{\mathrm{NN}}} = 2.76$ TeV in the dimuon and dielectron decay channels"**, S. Chatrchyan *et al.* [CMS Collaboration], JHEP **1503**022 (2015)

33. **"Identification techniques for highly boosted W bosons that decay into hadrons"**, V. Khachatryan *et al.* [CMS Collaboration], JHEP **1412**017 (2014)

34. **"Measurement of electroweak production of two jets in association with a Z boson in proton-proton collisions at $\sqrt{s} = 8$ TeV"**, V. Khachatryan *et al.* [CMS Collaboration], Eur. Phys. J. C **75**no. 266 (2015)

35. **"Searches for heavy Higgs bosons in two-Higgs-doublet models and for $t \to ch$ decay using multilepton and diphoton final states in pp collisions at 8 TeV"**, V. Khachatryan *et al.* [CMS Collaboration], Phys. Rev. D **90**112013 (2014)

36. **"Measurement of Prompt $\psi(2S) \to J/\psi$ Yield Ratios in Pb-Pb and $p-p$ Collisions at $\sqrt{s_{NN}}$ = 2.76 TeV"**, V. Khachatryan *et al.* [CMS Collaboration], Phys. Rev. Lett. **113**no. 26262301 (2014)

37. **"Measurement of the W boson helicity in events with a single reconstructed top quark in pp collisions at $\sqrt{s} = 8$ TeV"**, V. Khachatryan *et al.* [CMS Collaboration], JHEP **1501**053 (2015)

38. **"Search for Monotop Signatures in Proton-Proton Collisions at $\sqrt{s}$ = 8 TeV"**, V. Khachatryan *et al.* [CMS Collaboration], Phys. Rev. Lett. **114**no. 10101801 (2015)

39. **"Search for standard model production of four top quarks in the lepton + jets channel in pp collisions at $\sqrt{s}$ = 8 TeV"**, V. Khachatryan *et al.* [CMS Collaboration], JHEP **1411**154 (2014)

40. **"Measurement of the production cross section ratio sigma(chi[b2](1P)) / sigma(chi[b1](1P)) in pp collisions at sqrt(s) = 8 TeV"**, V. Khachatryan *et al.* [CMS Collaboration], Phys. Lett. B **743**383 (2015)

41. **"Search for Displaced Supersymmetry in events with an electron and a muon with large impact parameters"**, V. Khachatryan *et al.* [CMS Collaboration], Phys. Rev. Lett. **114**no. 6061801 (2015)

42. **"Long-range two-particle correlations of strange hadrons with charged particles in pPb and PbPb collisions at LHC energies"**, V. Khachatryan *et al.* [CMS Collaboration], Phys. Lett. B **742**200 (2015)

43. **"Searches for electroweak neutralino and chargino production in channels with HiggsZand W bosons in pp collisions at 8 TeV"**, V. Khachatryan *et al.* [CMS Collaboration], Phys. Rev. D **90**no. 9092007 (2014)

44. **"Search for dark matterextra dimensionsand unparticles in monojet events in proton–proton collisions at $\sqrt{s} = 8$ TeV"**, V. Khachatryan *et al.* [CMS Collaboration], Eur. Phys. J. C **75**no. 5235 (2015)

45. **"Search for neutral MSSM Higgs bosons decaying to a pair of tau leptons in pp collisions"**, V. Khachatryan *et al.* [CMS Collaboration], JHEP **1410**160 (2014)

46. **"Measurements of jet multiplicity and differential production cross sections of $Z+$ jets events in proton-proton collisions at $\sqrt{s}$ = 7 TeV"**, V. Khachatryan *et al.* [CMS Collaboration], Phys. Rev. D **91**no. 5052008 (2015)

47. **"Search for physics beyond the standard model in final states with a lepton and missing transverse energy in proton-proton collisions at sqrt(s) = 8 TeV"**, V. Khachatryan *et al.* [CMS Collaboration], Phys. Rev. D **91**no. 9092005 (2015)

48. **"Search for the associated production of the Higgs boson with a top-quark pair"**, V. Khachatryan *et al.* [CMS Collaboration], JHEP **1409**087 (2014)[JHEP **1410**106 (2014)]

49. **"Search for pair production of third-generation scalar leptoquarks and top squarks in proton-proton collisions at sqrt(s) = 8 TeV"**, V. Khachatryan *et al.* [CMS Collaboration], Phys. Lett. B **739**229 (2014)

50. **"Measurement of the $t\bar{t}$ production cross section in pp collisions at $\sqrt{s} = 8$ TeV in dilepton final states containing one τ lepton"**, V. Khachatryan *et al.* [CMS Collaboration], Phys. Lett. B **739**23 (2014)

51. **"Search for heavy neutrinos and W bosons with right-handed couplings in proton-proton collisions at $\sqrt{s} = 8$ TeV"**, V. Khachatryan *et al.* [CMS Collaboration], Eur. Phys. J. C **74**no. 113149 (2014)

52. **"Search for new resonances decaying via WZ to leptons in proton-proton collisions at $\sqrt{s} = 8$ TeV"**, V. Khachatryan *et al.* [CMS Collaboration], Phys. Lett. B **740**83 (2015)

53. **"Study of hadronic event-shape variables in multijet final states in pp collisions at sqrt(s) = 7 TeV"**, V. Khachatryan *et al.* [CMS Collaboration], JHEP **1410**87 (2014)

54. **"Observation of the diphoton decay of the Higgs boson and measurement of its properties"**, V. Khachatryan *et al.* [CMS Collaboration], Eur. Phys. J. C **74**no. 103076 (2014)

55. **"Measurement of top quark-antiquark pair production in association with a W or Z boson in pp collisions at $\sqrt{s} = 8$ TeV"**, V. Khachatryan *et al.* [CMS Collaboration], Eur. Phys. J. C **74**no. 93060 (2014)

56. **"Differential cross section measurements for the production of a W boson in association with jets in proton–proton collisions at $\sqrt{s} = 7$ TeV"**, V. Khachatryan *et al.* [CMS Collaboration], Phys. Lett. B **741**12 (2015)

57. **"Search for excited quarks in the γ+jet final state in proton–proton collisions at $\sqrt{s} = 8$ TeV"**, V. Khachatryan *et al.* [CMS Collaboration], Phys. Lett. B **738**274 (2014)

58. **"Measurement of jet fragmentation in PbPb and pp collisions at $\sqrt{s_{NN}} =$ 2.76 TeV"**, S. Chatrchyan *et al.* [CMS Collaboration], Phys. Rev. C **90**no. 2024908 (2014)

59. **"Measurement of prompt J/ψ pair production in pp collisions at $\sqrt{s} = 7$ Tev"**, V. Khachatryan *et al.* [CMS Collaboration], JHEP **1409**094 (2014)

60. **"Measurement of the ratio of inclusive jet cross sections using the anti-k_T algorithm with radius parameters R=0.5 and 0.7 in pp collisions at $\sqrt{s}$ = 7 TeV"**, S. Chatrchyan *et al.* [CMS Collaboration], Phys. Rev. D **90**no. 7072006 (2014)
61. **"Measurement of the $pp \rightarrow ZZ$ production cross section and constraints on anomalous triple gauge couplings in four-lepton final states at $\sqrt{s}$ =8 TeV"**, V. Khachatryan *et al.* [CMS Collaboration], Phys. Lett. B **740**250 (2015)
62. **"Search for jet extinction in the inclusive jet-p_t spectrum from proton-proton collisions at $\sqrt{s}$ = 8 TeV"**, V. Khachatryan *et al.* [CMS Collaboration], Phys. Rev. D **90**no. 3032005 (2014)
63. **"Searches for electroweak production of charginos, neutralinos and sleptons decaying to leptons and WZ and Higgs bosons in pp collisions at 8 TeV"**, V. Khachatryan *et al.* [CMS Collaboration], Eur. Phys. J. C **74**no. 93036 (2014)
64. **"Measurement of differential cross sections for the production of a pair of isolated photons in pp collisions at $\sqrt{s} = 7$ TeV"**, S. Chatrchyan *et al.* [CMS Collaboration], Eur. Phys. J. C **74**no. 113129 (2014)
65. **"Description and performance of track and primary-vertex reconstruction with the CMS tracker"**, S. Chatrchyan *et al.* [CMS Collaboration], JINST **9**no. 10P10009 (2014)
66. **"Search for supersymmetry with razor variables in pp collisions at $\sqrt{s}$=7 TeV"**, S. Chatrchyan *et al.* [CMS Collaboration], Phys. Rev. D **90**no. 11112001 (2014)
67. **"Search for top-squark pairs decaying into Higgs or Z bosons in pp collisions at $\sqrt{s}$=8 TeV"**, V. Khachatryan *et al.* [CMS Collaboration], Phys. Lett. B **736**371 (2014)
68. **"Constraints on the Higgs boson width from off-shell production and decay to Z-boson pairs"**, V. Khachatryan *et al.* [CMS Collaboration], Phys. Lett. B **736**64 (2014)
69. **"Search for massive resonances decaying into pairs of boosted bosons in semi-leptonic final states at $\sqrt{s}$ = 8 TeV"**, V. Khachatryan *et al.* [CMS Collaboration], JHEP **1408**174 (2014)
70. **"Search for massive resonances in dijet systems containing jets tagged as W or Z boson decays in pp collisions at $\sqrt{s}$ = 8 TeV"**, V. Khachatryan *et al.* [CMS Collaboration], JHEP **1408**173 (2014)
71. **"Measurement of pseudorapidity distributions of charged particles in proton-proton collisions at $\sqrt{s}$ = 8 TeV by the CMS and TOTEM experiments"**, S. Chatrchyan *et al.* [CMS and TOTEM Collaborations], Eur. Phys. J. C **74**no. 103053 (2014)

72. **"Search for anomalous production of events with three or more leptons in *pp* collisions at $\sqrt(s) = 8$ TeV"**, S. Chatrchyan *et al.* [CMS Collaboration], Phys. Rev. D **90**032006 (2014)

73. **"Search for $WW\gamma$ and $WZ\gamma$ production and constraints on anomalous quartic gauge couplings in *pp* collisions at $\sqrt{s} = 8$ TeV"**, S. Chatrchyan *et al.* [CMS Collaboration], Phys. Rev. D **90**no. 3032008 (2014)

74. **"Measurement of jet multiplicity distributions in $\mathrm{t\bar{t}}$ production in pp collisions at $\sqrt{s} = 7$ TeV"**, S. Chatrchyan *et al.* [CMS Collaboration], Eur. Phys. J. C **74**3014 (2015)[Eur. Phys. J. C **75**no. 5216 (2015)]

75. **"Measurement of the ratio $B(t \to Wb)/B(t \to Wq)$ in pp collisions at $\sqrt{s} =$ 8 TeV"**, V. Khachatryan *et al.* [CMS Collaboration], Phys. Lett. B **736**33 (2014)

76. **"Search for invisible decays of Higgs bosons in the vector boson fusion and associated ZH production modes"**, S. Chatrchyan *et al.* [CMS Collaboration], Eur. Phys. J. C **74**2980 (2014)

77. **"Measurement of the t-channel single-top-quark production cross section and of the $\mid V_{tb} \mid$ CKM matrix element in pp collisions at $\sqrt{s}$= 8 TeV"**, V. Khachatryan *et al.* [CMS Collaboration], JHEP **1406**090 (2014)

78. **"Measurement of WZ and ZZ production in pp collisions at $\sqrt{s} = 8$ TeV in final states with b-tagged jets"**, S. Chatrchyan *et al.* [CMS Collaboration], Eur. Phys. J. C **74**no. 82973 (2014)

79. **"Alignment of the CMS tracker with LHC and cosmic ray data"**, S. Chatrchyan *et al.* [CMS Collaboration], JINST **9**P06009 (2014)

80. **"Search for new physics in the multijet and missing transverse momentum final state in proton-proton collisions at $\sqrt{s}$= 8 TeV"**, S. Chatrchyan *et al.* [CMS Collaboration], JHEP **1406**055 (2014)

81. **"Measurements of the $t\bar{t}$ charge asymmetry using the dilepton decay channel in pp collisions at $\sqrt{s} = 7$ TeV"**, S. Chatrchyan *et al.* [CMS Collaboration], JHEP **1404**191 (2014)

82. **"Search for W' $\to$ tb decays in the lepton + jets final state in pp collisions at $\sqrt{s} = 8$ TeV"**, S. Chatrchyan *et al.* [CMS Collaboration], JHEP **1405**108 (2014)

83. **"Measurement of the production cross sections for a Z boson and one or more b jets in pp collisions at sqrt(s) = 7 TeV"**, S. Chatrchyan *et al.* [CMS Collaboration], JHEP **1406**120 (2014)

84. **"Measurement of inclusive W and Z boson production cross sections in pp collisions at $\sqrt{s} = 8$ TeV"**, S. Chatrchyan *et al.* [CMS Collaboration], Phys. Rev. Lett. **112**191802 (2014)

85. **"Evidence for the direct decay of the 125 GeV Higgs boson to fermions"**, S. Chatrchyan *et al.* [CMS Collaboration], Nature Phys. **10**557 (2014)

86. **"Evidence for the 125 GeV Higgs boson decaying to a pair of τ leptons"**, S. Chatrchyan *et al.* [CMS Collaboration], JHEP **1405**104 (2014)

87. **"Studies of dijet transverse momentum balance and pseudorapidity distributions in pPb collisions at $\sqrt{s_{\mathrm{NN}}} = 5.02$ TeV"**, S. Chatrchyan *et al.* [CMS Collaboration], Eur. Phys. J. C **74**no. 72951 (2014)

88. **"Observation of the associated production of a single top quark and a W boson in pp collisions at $\sqrt{s}$ =8 TeV"**, S. Chatrchyan *et al.* [CMS Collaboration], Phys. Rev. Lett. **112**no. 23231802 (2014)

89. **"Measurement of the $t\bar{t}$ production cross section in the dilepton channel in pp collisions at $\sqrt{s}$ = 8 TeV"**, S. Chatrchyan *et al.* [CMS Collaboration], JHEP **1402**024 (2014)[JHEP **1402**102 (2014)]

90. **"Measurement of the production cross section for a W boson and two b jets in pp collisions at $\sqrt{s}$=7 TeV"**, S. Chatrchyan *et al.* [CMS Collaboration], Phys. Lett. B **735**204 (2014)

91. **"Measurement of four-jet production in proton-proton collisions at $\sqrt{s} = 7$ TeV"**, S. Chatrchyan *et al.* [CMS Collaboration], Phys. Rev. D **89**no. 9092010 (2014)

92. **"Event activity dependence of Y(nS) production in $\sqrt{s_{NN}}$=5.02 TeV pPb and $\sqrt{s}$=2.76 TeV pp collisions"**, S. Chatrchyan *et al.* [CMS Collaboration], JHEP **1404**103 (2014)

93. **"Measurement of the muon charge asymmetry in inclusive $pp \to W + X$ production at $\sqrt{s}$ = 7 TeV and an improved determination of light parton distribution functions"**, S. Chatrchyan *et al.* [CMS Collaboration], Phys. Rev. D **90**no. 3032004 (2014)

94. **"Study of double parton scattering using W + 2-jet events in proton-proton collisions at $\sqrt{s}$ = 7 TeV"**, S. Chatrchyan *et al.* [CMS Collaboration], JHEP **1403**032 (2014)

95. **"Measurement of the properties of a Higgs boson in the four-lepton final state"**, S. Chatrchyan *et al.* [CMS Collaboration], Phys. Rev. D **89**no. 9092007 (2014)

96. **"Evidence of b-Jet Quenching in PbPb Collisions at $\sqrt{s_{NN}} = 2.76$ TeV"**, S. Chatrchyan *et al.* [CMS Collaboration], Phys. Rev. Lett. **113**no. 13132301 (2014)

97. **"Search for Flavor-Changing Neutral Currents in Top-Quark Decays $t \to Zq$ in pp Collisions at $\sqrt{s} = 8$ TeV"**, S. Chatrchyan *et al.* [CMS Collaboration], Phys. Rev. Lett. **112**no. 17171802 (2014)

98. **"Search for top squark and higgsino production using diphoton Higgs boson decays"**, S. Chatrchyan *et al.* [CMS Collaboration], Phys. Rev. Lett. **112**161802 (2014)
99. **"Search for top-quark partners with charge 5/3 in the same-sign dilepton final state"**, S. Chatrchyan *et al.* [CMS Collaboration], Phys. Rev. Lett. **112**no. 17171801 (2014)
100. **"Studies of azimuthal dihadron correlations in ultra-central PbPb collisions at $\sqrt{s_{NN}}$ = 2.76 TeV"**, S. Chatrchyan *et al.* [CMS Collaboration], JHEP **1402**088 (2014)
101. **"Measurement of Higgs boson production and properties in the WW decay channel with leptonic final states"**, S. Chatrchyan *et al.* [CMS Collaboration], JHEP **1401**096 (2014)
102. **"Inclusive search for a vector-like T quark with charge $\frac{2}{3}$ in pp collisions at $\sqrt{s}$ = 8 TeV"**, S. Chatrchyan *et al.* [CMS Collaboration], Phys. Lett. B **729**149 (2014)
103. **"Search for new physics in events with same-sign dileptons and jets in pp collisions at $\sqrt{s}$ = 8 TeV"**, S. Chatrchyan *et al.* [CMS Collaboration], JHEP **1401**163 (2014)[JHEP **1501**014 (2015)]
104. **"Measurement of the triple-differential cross section for photon+jets production in proton-proton collisions at $\sqrt{s}$=7 TeV"**, S. Chatrchyan *et al.* [CMS Collaboration], JHEP **1406**009 (2014)
105. **"Probing color coherence effects in pp collisions at $\sqrt{s} = 7$ TeV"**, S. Chatrchyan *et al.* [CMS Collaboration], Eur. Phys. J. C **74**no. 62901 (2014)
106. **"Search for pair production of excited top quarks in the lepton + jets final state"**, S. Chatrchyan *et al.* [CMS Collaboration], JHEP **1406**125 (2014)
107. **"Search for supersymmetry in pp collisions at $\sqrt{s}$=8 TeV in events with a single leptonlarge jet multiplicityand multiple b jets"**, S. Chatrchyan *et al.* [CMS Collaboration], Phys. Lett. B **733**328 (2014)
108. **"Measurements of $t\bar{t}$ spin correlations and top-quark polarization using dilepton final states in pp collisions at $\sqrt{s}$ = 7 TeV"**, S. Chatrchyan *et al.* [CMS Collaboration], Phys. Rev. Lett. **112**no. 18182001 (2014)
109. **"Searches for light- and heavy-flavour three-jet resonances in pp collisions at $\sqrt{s} = 8$ TeV"**, S. Chatrchyan *et al.* [CMS Collaboration], Phys. Lett. B **730**193 (2014)
110. **"Measurement of higher-order harmonic azimuthal anisotropy in PbPb collisions at $\sqrt{s_{NN}}$ = 2.76 TeV"**, S. Chatrchyan *et al.* [CMS Collaboration], Phys. Rev. C **89**no. 4044906 (2014)

111. **"Measurement of the differential and double-differential Drell-Yan cross sections in proton-proton collisions at $\sqrt{s} = 7$ TeV"**, S. Chatrchyan *et al.* [CMS Collaboration], JHEP **1312**030 (2013)

112. **"Jet and underlying event properties as a function of charged-particle multiplicity in proton–proton collisions at $\sqrt{s} = 7$ TeV"**, S. Chatrchyan *et al.* [CMS Collaboration], Eur. Phys. J. C **73**no. 122674 (2013)

113. **"Search for the standard model Higgs boson produced in association with a W or a Z boson and decaying to bottom quarks"**, S. Chatrchyan *et al.* [CMS Collaboration], Phys. Rev. D **89**no. 1012003 (2014)

114. **"Rapidity distributions in exclusive Z + jet and γ + jet events in pp collisions at $\sqrt{s} = 7$ TeV"**, S. Chatrchyan *et al.* [CMS Collaboration], Phys. Rev. D **88**no. 11112009 (2013)

115. **"Search for baryon number violation in top-quark decays"**, S. Chatrchyan *et al.* [CMS Collaboration], Phys. Lett. B **731**173 (2014)

116. **"Measurement of the cross section and angular correlations for associated production of a Z boson with b hadrons in pp collisions at $\sqrt{s} = 7$ TeV"**, S. Chatrchyan *et al.* [CMS Collaboration], JHEP **1312**039 (2013)

117. **"Measurement of associated W + charm production in pp collisions at $\sqrt{s} = 7$ TeV"**, S. Chatrchyan *et al.* [CMS Collaboration], JHEP **1402**013 (2014)

118. **"Modification of jet shapes in PbPb collisions at $\sqrt{s_{NN}} = 2.76$ TeV"**, S. Chatrchyan *et al.* [CMS Collaboration], Phys. Lett. B **730**243 (2014)

119. **"Observation of a peaking structure in the $J/\psi\phi$ mass spectrum from $B^{\pm} \to J/\psi\phi K^{\pm}$ decays"**, S. Chatrchyan *et al.* [CMS Collaboration], Phys. Lett. B **734**261 (2014)

120. **"Searches for new physics using the $t\bar{t}$ invariant mass distribution in pp collisions at $\sqrt{s}$=8 TeV"**, S. Chatrchyan *et al.* [CMS Collaboration], Phys. Rev. Lett. **111**no. 21211804 (2013)[Phys. Rev. Lett. **112**no. 11119903 (2014)]

121. **"Measurement of the production cross section for $Z\gamma \to \nu\bar{\nu}\gamma$ in pp collisions at $\sqrt{s} = 7$ TeV and limits on $ZZ\gamma$ and $Z\gamma\gamma$ triple gauge boson couplings"**, S. Chatrchyan *et al.* [CMS Collaboration], JHEP **1310**164 (2013)

122. **"Search for a new bottomonium state decaying to $\Upsilon(1S)\pi^+\pi^-$ in pp collisions at $\sqrt{s} = 8$ TeV"**, S. Chatrchyan *et al.* [CMS Collaboration], Phys. Lett. B **727**57 (2013)

123. **"Measurement of the $W\gamma$ and $Z\gamma$ inclusive cross sections in pp collisions at $\sqrt{s} = 7$ TeV and limits on anomalous triple gauge boson couplings"**, S. Chatrchyan *et al.* [CMS Collaboration], Phys. Rev. D **89**no. 9092005 (2014)

124. **"Measurement of the W-boson helicity in top-quark decays from $t\bar{t}$ production in lepton+jets events in pp collisions at $\sqrt{s} = 7$ TeV"**, S. Chatrchyan *et al.* [CMS Collaboration], JHEP **1310**167 (2013)

125. **"Angular analysis and branching fraction measurement of the decay $B^0 \to K^{*0}\mu^+\mu^-$"**, S. Chatrchyan *et al.* [CMS Collaboration], Phys. Lett. B **727**77 (2013)

126. **"Search for top-squark pair production in the single-lepton final state in pp collisions at $\sqrt{s} = 8$ TeV"**, S. Chatrchyan *et al.* [CMS Collaboration], Eur. Phys. J. C **73**no. 122677 (2013)

127. **"Measurement of the prompt J/ψ and ψ(2S) polarizations in pp collisions at $\sqrt{s} = 7$ TeV"**, S. Chatrchyan *et al.* [CMS Collaboration], Phys. Lett. B **727**381 (2013)

128. **"Search for a Higgs boson decaying into a Z and a photon in pp collisions at $\sqrt{s} = 7$ and 8 TeV"**, S. Chatrchyan *et al.* [CMS Collaboration], Phys. Lett. B **726**587 (2013)

129. **"Measurement of the B(s) to mu+ mu- branching fraction and search for B0 to mu+ mu- with the CMS Experiment"**, S. Chatrchyan *et al.* [CMS Collaboration], Phys. Rev. Lett. **111**101804 (2013)

130. **"Measurement of the top-quark mass in all-jets $t\bar{t}$ events in pp collisions at $\sqrt{s}$=7 TeV"**, S. Chatrchyan *et al.* [CMS Collaboration], Eur. Phys. J. C **74**no. 42758 (2014)

131. **"Study of the production of charged pions, kaons and protons in pPb collisions at $\sqrt{s_{NN}} =$ 5.02 TeV"**, S. Chatrchyan *et al.* [CMS Collaboration], Eur. Phys. J. C **74**no. 62847 (2014)

132. **"Determination of the top-quark pole mass and strong coupling constant from the t t-bar production cross section in pp collisions at $\sqrt{s} = 7$ TeV"**, S. Chatrchyan *et al.* [CMS Collaboration], Phys. Lett. B **728**496 (2014)[Phys. Lett. B **728**526 (2014)]

133. **"The performance of the CMS muon detector in proton-proton collisions at sqrt(s) = 7 TeV at the LHC"**, S. Chatrchyan *et al.* [CMS Collaboration], JINST **8**P11002 (2013)

134. **"Search for top squarks in R-parity-violating supersymmetry using three or more leptons and b-tagged jets"**, S. Chatrchyan *et al.* [CMS Collaboration], Phys. Rev. Lett. **111**no. 22221801 (2013)

135. **"Energy Calibration and Resolution of the CMS Electromagnetic Calorimeter in pp Collisions at $\sqrt{s} = 7$ TeV"**, S. Chatrchyan *et al.* [CMS Collaboration], JINST **8**P09009 (2013)

136. **"Measurement of the W^+W^- Cross section in pp Collisions at $\sqrt{s} = 7$ TeV and Limits on Anomalous $WW\gamma$ and WWZ couplings"**, S. Chatrchyan *et al.* [CMS Collaboration], Eur. Phys. J. C **73**no. 102610 (2013)

137. **"Measurement of the hadronic activity in events with a Z and two jets and extraction of the cross section for the electroweak production of a Z with two jets in pp collisions at $\sqrt{s}$ = 7 TeV"**, S. Chatrchyan *et al.* [CMS Collaboration], JHEP **1310**062 (2013)

138. **"Measurement of neutral strange particle production in the underlying event in proton-proton collisions at sqrt(s) = 7 TeV"**, S. Chatrchyan *et al.* [CMS Collaboration], Phys. Rev. D **88**052001 (2013)

139. **"Study of exclusive two-photon production of W^+W^- in pp collisions at $\sqrt{s} = 7$ TeV and constraints on anomalous quartic gauge couplings"**, S. Chatrchyan *et al.* [CMS Collaboration], JHEP **1307**116 (2013)

140. **"Search for gluino mediated bottom- and top-squark production in multijet final states in pp collisions at 8 TeV"**, S. Chatrchyan *et al.* [CMS Collaboration], Phys. Lett. B **725**243 (2013)

141. **"Multiplicity and transverse momentum dependence of two- and four-particle correlations in pPb and PbPb collisions"**, S. Chatrchyan *et al.* [CMS Collaboration], Phys. Lett. B **724**213 (2013)

142. **"Searches for long-lived charged particles in pp collisions at $\sqrt{s}$=7 and 8 TeV"**, S. Chatrchyan *et al.* [CMS Collaboration], JHEP **1307**122 (2013)

143. **"Measurement of the ratio of the inclusive 3-jet cross section to the inclusive 2-jet cross section in pp collisions at $\sqrt{s}$ = 7 TeV and first determination of the strong coupling constant in the TeV range"**, S. Chatrchyan *et al.* [CMS Collaboration], Eur. Phys. J. C **73**no. 102604 (2013)

144. **"Measurement of the Λ_b^0 lifetime in pp collisions at $\sqrt{s} = 7$ TeV"**, S. Chatrchyan *et al.* [CMS Collaboration], JHEP **1307**163 (2013)

145. **"Measurement of masses in the $t\bar{t}$ system by kinematic endpoints in pp collisions at $\sqrt{s}$ = 7 TeV"**, S. Chatrchyan *et al.* [CMS Collaboration], Eur. Phys. J. C **73**2494 (2013)

146. **"Search for a standard-model-like Higgs boson with a mass in the range 145 to 1000 GeV at the LHC"**, S. Chatrchyan *et al.* [CMS Collaboration], Eur. Phys. J. C **73**2469 (2013)

147. **"Measurement of the $\Upsilon(1S)\Upsilon(2S)$and $\Upsilon(3S)$ cross sections in pp collisions at $\sqrt{s}$ = 7 TeV"**, S. Chatrchyan *et al.* [CMS Collaboration], Phys. Lett. B **727**101 (2013)

148. **“Search for microscopic black holes in pp collisions at sqrt(s) = 8 TeV”**, S. Chatrchyan *et al.* [CMS Collaboration], JHEP **1307**178 (2013)

149. **“Studies of jet mass in dijet and W/Z + jet events”**, S. Chatrchyan *et al.* [CMS Collaboration], JHEP **1305**090 (2013)

150. **“Observation of a new boson with mass near 125 GeV in pp collisions at $\sqrt{s}$ = 7 and 8 TeV”**, S. Chatrchyan *et al.* [CMS Collaboration], JHEP **1306**081 (2013)

151. **“A New Boson with a Mass of 125 GeV Observed with the CMS Experiment at the Large Hadron Collider”**, S. Chatrchyan *et al.* [CMS Collaboration], Science **338**1569 (2012).

152. **“Measurement of associated production of vector bosons and top quark-antiquark pairs at sqrt(s) = 7 TeV”**, S. Chatrchyan *et al.* [CMS Collaboration], Phys. Rev. Lett. **110**172002 (2013)

153. **“Search for supersymmetry in hadronic final states with missing transverse energy using the variables α_T and b-quark multiplicity in pp collisions at $\sqrt{s} = 8$ TeV”**, S. Chatrchyan *et al.* [CMS Collaboration], Eur. Phys. J. C **73**no. 92568 (2013)

154. **“Search for the standard model Higgs boson produced in association with a top-quark pair in pp collisions at the LHC”**, S. Chatrchyan *et al.* [CMS Collaboration], JHEP **1305**145 (2013)

155. **“Search for narrow resonances using the dijet mass spectrum in pp collisions at $\sqrt{s}$=8 TeV”**, S. Chatrchyan *et al.* [CMS Collaboration], Phys. Rev. D **87**no. 11114015 (2013)

156. **“Measurement of the X(3872) production cross section via decays to J/psi pi pi in pp collisions at sqrt(s) = 7 TeV”**, S. Chatrchyan *et al.* [CMS Collaboration], JHEP **1304**154 (2013)

157. **“Search for a Higgs boson decaying into a b-quark pair and produced in association with b quarks in proton-proton collisions at 7 TeV”**, S. Chatrchyan *et al.* [CMS Collaboration], Phys. Lett. B **722**207 (2013)

158. **“Search for new physics in final states with a lepton and missing transverse energy in pp collisions at the LHC”**, S. Chatrchyan *et al.* [CMS Collaboration], Phys. Rev. D **87**no. 7072005 (2013)

159. **“Study of the underlying event at forward rapidity in pp collisions at $\sqrt{s}$ = 0.9, 2.76 and 7 TeV”**, S. Chatrchyan *et al.* [CMS Collaboration], JHEP **1304**072 (2013)

160. **“Searches for Higgs bosons in pp collisions at sqrt(s) = 7 and 8 TeV in the context of four-generation and fermiophobic models”**, S. Chatrchyan *et al.* [CMS Collaboration], Phys. Lett. B **725**36 (2013)

161. **“Search for pair-produced dijet resonances in four-jet final states in pp collisions at $\sqrt{s}$=7 TeV”**, S. Chatrchyan *et al.* [CMS Collaboration], Phys. Rev. Lett. **110**no. 14141802 (2013)

162. **“Measurement of the $t\bar{t}$ production cross section in the all-jet final state in pp collisions at $\sqrt{s}$ = 7 TeV”**, S. Chatrchyan *et al.* [CMS Collaboration], JHEP **1305**065 (2013)

163. **“Measurement of the top-antitop production cross section in the tau+jets channel in pp collisions at sqrt(s) = 7 TeV”**, S. Chatrchyan *et al.* [CMS Collaboration], Eur. Phys. J. C **73**no. 42386 (2013)

164. **“Search for contact interactions using the inclusive jet p_T spectrum in pp collisions at $\sqrt{s} = 7$ TeV”**, S. Chatrchyan *et al.* [CMS Collaboration], Phys. Rev. D **87**no. 5052017 (2013)

165. **“Measurement of W+W- and ZZ production cross sections in pp collisions at sqrt(s) = 8 TeV”**, S. Chatrchyan *et al.* [CMS Collaboration], Phys. Lett. B **721**190 (2013)

166. **“Search for physics beyond the standard model in events with τ leptonsjetsand large transverse momentum imbalance in pp collisions at $\sqrt{s}$ = 7 TeV”**, S. Chatrchyan *et al.* [CMS Collaboration], Eur. Phys. J. C **73**2493 (2013)

167. **“Interpretation of Searches for Supersymmetry with simplified Models”**, S. Chatrchyan *et al.* [CMS Collaboration], Phys. Rev. D **88**no. 5052017 (2013)

168. **“Event shapes and azimuthal correlations in Z + jets events in pp collisions at $\sqrt{s} = 7$ TeV”**, S. Chatrchyan *et al.* [CMS Collaboration], Phys. Lett. B **722**238 (2013)

169. **“Search for supersymmetry in events with opposite-sign dileptons and missing transverse energy using an artificial neural network”**, S. Chatrchyan *et al.* [CMS Collaboration], Phys. Rev. D **87**no. 7072001 (2013)

170. **“Search for supersymmetry in pp collisions at $\sqrt{s} = 7$ TeV in events with a single leptonjetsand missing transverse momentum”**, S. Chatrchyan *et al.* [CMS Collaboration], Eur. Phys. J. C **73**2404 (2013)

171. **“Study of the Mass and Spin-Parity of the Higgs Boson Candidate Via Its Decays to Z Boson Pairs”**, S. Chatrchyan *et al.* [CMS Collaboration], Phys. Rev. Lett. **110**no. 8081803 (2013)

172. **“Measurements of differential jet cross sections in proton-proton collisions at $\sqrt{s} = 7$ TeV with the CMS detector”**, S. Chatrchyan *et al.* [CMS Collaboration], Phys. Rev. D **87**no. 11112002 (2013)[Phys. Rev. D **87**no. 11119902 (2013)]

173. **“Measurement of the $t\bar{t}$ production cross section in pp collisions at $\sqrt{s} = 7$ TeV with lepton + jets final states”**, S. Chatrchyan *et al.* [CMS Collaboration], Phys. Lett. B **720**83 (2013)

174. **“Inclusive search for supersymmetry using the razor variables in pp collisions at $\sqrt{s} = 7$ TeV”**, S. Chatrchyan *et al.* [CMS Collaboration], Phys. Rev. Lett. **111**no. 8081802 (2013)

175. **“Search for new physics in events with same-sign dileptons and b jets in pp collisions at $\sqrt{s} = 8$ TeV”**, S. Chatrchyan *et al.* [CMS Collaboration], JHEP **1303**037 (2013)[JHEP **1307**041 (2013)]

176. **“Search for heavy narrow dilepton resonances in pp collisions at $\sqrt{s} = 7$ TeV and $\sqrt{s} = 8$ TeV”**, S. Chatrchyan *et al.* [CMS Collaboration], Phys. Lett. B **720**63 (2013)

177. **“Search for contact interactions in $\mu^+\mu^-$ events in pp collisions at $\sqrt{s} = 7$ TeV”**, S. Chatrchyan *et al.* [CMS Collaboration], Phys. Rev. D **87**no. 3032001 (2013)

178. **“Search for heavy resonances in the W/Z-tagged dijet mass spectrum in pp collisions at 7 TeV”**, S. Chatrchyan *et al.* [CMS Collaboration], Phys. Lett. B **723**280 (2013)

179. **“Search for long-lived particles decaying to photons and missing energy in proton-proton collisions at $\sqrt{s} = 7$ TeV”**, S. Chatrchyan *et al.* [CMS Collaboration], Phys. Lett. B **722**273 (2013)

180. **“Search for exotic resonances decaying into WZ/ZZ in pp collisions at $\sqrt{s} = 7$ TeV”**, S. Chatrchyan *et al.* [CMS Collaboration], JHEP **1302**036 (2013)

181. **“Measurement of the ZZ production cross section and search for anomalous couplings in 2 l2l ’ final states in pp collisions at $\sqrt{s} = 7$ TeV”**, S. Chatrchyan *et al.* [CMS Collaboration], JHEP **1301**063 (2013)

182. **“Search for new physics in events with photonsjetsand missing transverse energy in pp collisions at $\sqrt{s} = 7$ TeV”**, S. Chatrchyan *et al.* [CMS Collaboration], JHEP **1303**111 (2013)

183. **“Identification of b-quark jets with the CMS experiment”**, S. Chatrchyan *et al.* [CMS Collaboration], JINST **8**P04013 (2013)

184. **"Search for Z ' resonances decaying to $t\bar{t}$ in dilepton+jets final states in pp collisions at $\sqrt{s} = 7$ TeV"**, S. Chatrchyan *et al.* [CMS Collaboration], Phys. Rev. D **87**no. 7072002 (2013)

185. **"Search for supersymmetry in final states with a single lepton$b$-quark jetsand missing transverse energy in proton-proton collisions at $\sqrt{s} = 7$ TeV"**, S. Chatrchyan *et al.* [CMS Collaboration], Phys. Rev. D **87**no. 5052006 (2013)

186. **"Search in leptonic channels for heavy resonances decaying to long-lived neutral particles"**, S. Chatrchyan *et al.* [CMS Collaboration], JHEP **1302**085 (2013)

187. **"Measurement of differential top-quark pair production cross sections in pp colisions at $\sqrt{s} = 7$ TeV"**, S. Chatrchyan *et al.* [CMS Collaboration], Eur. Phys. J. C **73**no. 32339 (2013)

188. **"Search for supersymmetry in final states with missing transverse energy and 012or at least 3 b-quark jets in 7 TeV pp collisions using the variable alphaT"**, S. Chatrchyan *et al.* [CMS Collaboration], JHEP **1301**077 (2013)

189. **"Search for a non-standard-model Higgs boson decaying to a pair of new light bosons in four-muon final states"**, S. Chatrchyan *et al.* [CMS Collaboration], Phys. Lett. B **726**564 (2013)

190. **"Measurement of the sum of WW and WZ production with W+dijet events in pp collisions at $\sqrt{s} = 7$ TeV"**, S. Chatrchyan *et al.* [CMS Collaboration], Eur. Phys. J. C **73**no. 22283 (2013)

191. **"Search for heavy quarks decaying into a top quark and a W or Z boson using lepton + jets events in pp collisions at $\sqrt{s} = 7$ TeV"**, S. Chatrchyan *et al.* [CMS Collaboration], JHEP **1301**154 (2013)

192. **"Measurement of the inelastic proton-proton cross section at $\sqrt{s} = 7$ TeV"**, S. Chatrchyan *et al.* [CMS Collaboration], Phys. Lett. B **722**5 (2013)

193. **"Search for pair production of third-generation leptoquarks and top squarks in pp collisions at $\sqrt{s} = 7$ TeV"**, S. Chatrchyan *et al.* [CMS Collaboration], Phys. Rev. Lett. **110**no. 8081801 (2013)

194. **"Search for third-generation leptoquarks and scalar bottom quarks in pp collisions at $\sqrt{s} = 7$ TeV"**, S. Chatrchyan *et al.* [CMS Collaboration], JHEP **1212**055 (2012)

195. **"Observation of long-range near-side angular correlations in proton-lead collisions at the LHC"**, S. Chatrchyan *et al.* [CMS Collaboration], Phys. Lett. B **718**795 (2013)

196. **“Observation of Z decays to four leptons with the CMS detector at the LHC”**, S. Chatrchyan *et al.* [CMS Collaboration], JHEP **1212**034 (2012)

197. **“Search for excited leptons in pp collisions at $\sqrt{s} = 7$ TeV”**, S. Chatrchyan *et al.* [CMS Collaboration], Phys. Lett. B **720**309 (2013)

198. **“Search for heavy neutrinos and W[R] bosons with right-handed couplings in a left-right symmetric model in pp collisions at sqrt(s) = 7 TeV”**, S. Chatrchyan *et al.* [CMS Collaboration], Phys. Rev. Lett. **109**261802 (2012)

199. **“Search for narrow resonances and quantum black holes in inclusive and b-tagged dijet mass spectra from pp collisions at $\sqrt{s} = 7$ TeV”**, S. Chatrchyan *et al.* [CMS Collaboration], JHEP **1301**013 (2013)

200. **“Search for fractionally charged particles in pp collisions at $\sqrt{s} = 7$ TeV”**, S. Chatrchyan *et al.* [CMS Collaboration], Phys. Rev. D **87**no. 9092008 (2013)

201. **“Search for supersymmetry in events with photons and low missing transverse energy in pp collisions at $\sqrt{s} = 7$ TeV”**, S. Chatrchyan *et al.* [CMS Collaboration], Phys. Lett. B **719**42 (2013)

202. **“Search for heavy lepton partners of neutrinos in proton-proton collisions in the context of the type III seesaw mechanism”**, S. Chatrchyan *et al.* [CMS Collaboration], Phys. Lett. B **718**348 (2012)

203. **“Measurement of the relative prompt production rate of chi(c2) and chi(c1) in pp collisions at $\sqrt{s} = 7$ TeV”**, S. Chatrchyan *et al.* [CMS Collaboration], Eur. Phys. J. C **72**2251 (2012)

204. **“Search for anomalous production of highly boosted Z bosons decaying to dimuons in pp collisions at $\sqrt{s} = 7$ TeV”**, S. Chatrchyan *et al.* [CMS Collaboration], Phys. Lett. B **722**28 (2013)

205. **“Search for electroweak production of charginos and neutralinos using leptonic final states in pp collisions at $\sqrt{s} = 7$ TeV”**, S. Chatrchyan *et al.* [CMS Collaboration], JHEP **1211**147 (2012)

206. **“Measurement of the single-top-quark t-channel cross section in pp collisions at $\sqrt{s} = 7$ TeV”**, S. Chatrchyan *et al.* [CMS Collaboration], JHEP **1212**035 (2012)

207. **“Search for resonant $t\bar{t}$ production in lepton+jets events in pp collisions at $\sqrt{s} = 7$ TeV”**, S. Chatrchyan *et al.* [CMS Collaboration], JHEP **1212**015 (2012)

208. **“Search for the standard model Higgs boson produced in association with W and Z bosons in pp collisions at $\sqrt{s} = 7$ TeV”**, S. Chatrchyan *et al.* [CMS Collaboration], JHEP **1211**088 (2012)

209. **"Search for a narrow spin-2 resonance decaying to a pair of Z vector bosons in the semileptonic final state"**, S. Chatrchyan *et al.* [CMS Collaboration], Phys. Lett. B **718**1208 (2013)

210. **"Evidence for associated production of a single top quark and W boson in pp collisions at $\sqrt{s}$ = 7 TeV"**, S. Chatrchyan *et al.* [CMS Collaboration], Phys. Rev. Lett. **110**022003 (2013)

211. **"Measurement of the $Y(1S)Y(2S)$ and $Y(3S)$ polarizations in pp collisions at $\sqrt{s}$ = 7 TeV"**, S. Chatrchyan *et al.* [CMS Collaboration], Phys. Rev. Lett. **110**no. 8081802 (2013)

212. **"Measurement of the top-quark mass in $t\bar{t}$ events with dilepton final states in pp collisions at $\sqrt{s} = 7$ TeV"**, S. Chatrchyan *et al.* [CMS Collaboration], Eur. Phys. J. C **72**2202 (2012)

213. **"Measurement of the top-quark mass in $t\bar{t}$ events with lepton+jets final states in pp collisions at $\sqrt{s} = 7$ TeV"**, S. Chatrchyan *et al.* [CMS Collaboration], JHEP **1212**105 (2012)

214. **"Observation of a diffractive contribution to dijet production in proton-proton collisions at $\sqrt{s} = 7$ TeV"**, S. Chatrchyan *et al.* [CMS Collaboration], Phys. Rev. D **87**no. 1012006 (2013)

215. **"Search for exclusive or semi-exclusive photon pair production and observation of exclusive and semi-exclusive electron pair production in pp collisions at $\sqrt{s} = 7$ TeV"**, S. Chatrchyan *et al.* [CMS Collaboration], JHEP **1211**080 (2012)

216. **"Combined search for the quarks of a sequential fourth generation"**, S. Chatrchyan *et al.* [CMS Collaboration], Phys. Rev. D **86**112003 (2012)

217. **"Search for pair produced fourth-generation up-type quarks in pp collisions at $\sqrt{s} = 7$ TeV with a lepton in the final state"**, S. Chatrchyan *et al.* [CMS Collaboration], Phys. Lett. B **718**307 (2012)

218. **"Search for supersymmetry in events with b-quark jets and missing transverse energy in pp collisions at 7 TeV"**, S. Chatrchyan *et al.* [CMS Collaboration], Phys. Rev. D **86**072010 (2012)

219. **"Study of the dijet mass spectrum in $pp \to W+$ jets events at $\sqrt{s} = 7$ TeV"**, S. Chatrchyan *et al.* [CMS Collaboration], Phys. Rev. Lett. **109**251801 (2012)

220. **"Search for three-jet resonances in pp collisions at $\sqrt{s} = 7$ TeV"**, S. Chatrchyan *et al.* [CMS Collaboration], Phys. Lett. B **718**329 (2012)

221. **"Observation of sequential Upsilon suppression in PbPb collisions"**, S. Chatrchyan *et al.* [CMS Collaboration], Phys. Rev. Lett. **109**222301 (2012)

222. **"Measurement of the $t\bar{t}$ production cross section in the dilepton channel in pp collisions at $\sqrt{s}$ = 7 TeV"**, S. Chatrchyan *et al.* [CMS Collaboration], JHEP **1211**067 (2012)

223. **"Measurement of the azimuthal anisotropy of neutral pions in PbPb collisions at $\sqrt{s_{NN}}$ = 2.76 TeV"**, S. Chatrchyan *et al.* [CMS Collaboration], Phys. Rev. Lett. **110**no. 4042301 (2013)

224. **"Search for flavor changing neutral currents in top quark decays in pp collisions at 7 TeV"**, S. Chatrchyan *et al.* [CMS Collaboration], Phys. Lett. B **718**1252 (2013)

225. **"Search for a W ' boson decaying to a bottom quark and a top quark in pp collisions at $\sqrt{s} = 7$ TeV"**, S. Chatrchyan *et al.* [CMS Collaboration], Phys. Lett. B **718**1229 (2013)

226. **"Observation of a new boson at a mass of 125 GeV with the CMS experiment at the LHC"**, S. Chatrchyan *et al.* [CMS Collaboration], Phys. Lett. B **716**30 (2012)

227. **"Search for heavy Majorana neutrinos in $\mu^+\mu^+[\mu^-\mu^-]$ and $e^+e^+[e^-e^-]$ events in pp collisions at $\sqrt{s} = 7$ TeV"**, S. Chatrchyan *et al.* [CMS Collaboration], Phys. Lett. B **717**109 (2012)

228. **"Search for pair production of first- and second-generation scalar leptoquarks in pp collisions at $\sqrt{s} = 7$ TeV"**, S. Chatrchyan *et al.* [CMS Collaboration], Phys. Rev. D **86**052013 (2012)

229. **"Study of the inclusive production of charged pionskaonsand protons in pp collisions at $\sqrt{s} = 0.9$2.76and 7 TeV"**, S. Chatrchyan *et al.* [CMS Collaboration], Eur. Phys. J. C **72**2164 (2012)

230. **"Forward-backward asymmetry of Drell-Yan lepton pairs in pp collisions at $\sqrt{s} = 7$ TeV"**, S. Chatrchyan *et al.* [CMS Collaboration], Phys. Lett. B **718**752 (2013)

231. **"A search for a doubly-charged Higgs boson in pp collisions at $\sqrt{s}$ = 7 TeV"**, S. Chatrchyan *et al.* [CMS Collaboration], Eur. Phys. J. C **72**2189 (2012)

232. **"Measurement of the underlying event activity in pp collisions at $\sqrt{s} = 0.9$ and 7 TeV with the novel jet-area/median approach"**, S. Chatrchyan *et al.* [CMS Collaboration], JHEP **1208**130 (2012)

233. **"Search for new physics in the multijet and missing transverse momentum final state in proton-proton collisions at $\sqrt{s} = 7$ TeV"**, S. Chatrchyan *et al.* [CMS Collaboration], Phys. Rev. Lett. **109**171803 (2012)

234. **"Search for supersymmetry in hadronic final states using MT2 in** pp **collisions at** $\sqrt{s} = 7$ **TeV"**, S. Chatrchyan *et al.* [CMS Collaboration], JHEP **1210**018 (2012)

235. **"Search for a fermiophobic Higgs boson in** pp **collisions at** $\sqrt{s} = 7$ **TeV"**, S. Chatrchyan *et al.* [CMS Collaboration], JHEP **1209**111 (2012)

236. **"Search for new physics with long-lived particles decaying to photons and missing energy in** pp **collisions at** $\sqrt{s} = 7$ **TeV"**, S. Chatrchyan *et al.* [CMS Collaboration], JHEP **1211**172 (2012)

237. **"Search for stopped long-lived particles produced in** pp **collisions at** $\sqrt{s} = 7$ **TeV"**, S. Chatrchyan *et al.* [CMS Collaboration], JHEP **1208**026 (2012)

238. **"Inclusive and differential measurements of the** $t\bar{t}$ **charge asymmetry in proton-proton collisions at 7 TeV"**, S. Chatrchyan *et al.* [CMS Collaboration], Phys. Lett. B **717**129 (2012)

239. **"Search for a light pseudoscalar Higgs boson in the dimuon decay channel in** pp **collisions at** $\sqrt{s} = 7$ **TeV"**, S. Chatrchyan *et al.* [CMS Collaboration], Phys. Rev. Lett. **109**121801 (2012)

240. **"Search for dark matter and large extra dimensions in monojet events in** pp **collisions at** $\sqrt{s} = 7$ **TeV"**, S. Chatrchyan *et al.* [CMS Collaboration], JHEP **1209**094 (2012)

241. **"Performance of CMS muon reconstruction in** pp **collision events at** $\sqrt{s} = 7$ **TeV"**, S. Chatrchyan *et al.* [CMS Collaboration], JINST **7**P10002 (2012)

242. **"Search for new physics in events with opposite-sign leptonsjetsand missing transverse energy in** pp **collisions at** $\sqrt{s} = 7$ **TeV"**, S. Chatrchyan *et al.* [CMS Collaboration], Phys. Lett. B **718**815 (2013)

243. **"Search for charge-asymmetric production of** W **' bosons in top pair + jet events from** pp **collisions at** $\sqrt{s} = 7$ **TeV"**, S. Chatrchyan *et al.* [CMS Collaboration], Phys. Lett. B **717**351 (2012)

244. **"Measurement of the electron charge asymmetry in inclusive** W **production in** pp **collisions at** $\sqrt{s} = 7$ **TeV"**, S. Chatrchyan *et al.* [CMS Collaboration], Phys. Rev. Lett. **109**111806 (2012)

245. **"Search for narrow resonances in dilepton mass spectra in** pp **collisions at** $\sqrt{s} = 7$ **TeV"**, S. Chatrchyan *et al.* [CMS Collaboration], Phys. Lett. B **714**158 (2012)

246. **"Search for high mass resonances decaying into** τ^- **lepton pairs in** pp **collisions at** $\sqrt{s} = 7$ **TeV"**, S. Chatrchyan *et al.* [CMS Collaboration], Phys. Lett. B **716**82 (2012)

247. **“Search for a W' or Techni-ρ Decaying into WZ in pp Collisions at $\sqrt{s} = 7$ TeV”**, S. Chatrchyan *et al.* [CMS Collaboration], Phys. Rev. Lett. **109**141801 (2012)

248. **“Search for new physics with same-sign isolated dilepton events with jets and missing transverse energy”**, S. Chatrchyan *et al.* [CMS Collaboration], Phys. Rev. Lett. **109**071803 (2012)

249. **“Study of W boson production in PbPb and pp collisions at $\sqrt{s_{NN}} = 2.76$ TeV”**, S. Chatrchyan *et al.* [CMS Collaboration], Phys. Lett. B **715**66 (2012)

250. **“Measurement of jet fragmentation into charged particles in pp and PbPb collisions at $\sqrt{s_{NN}} = 2.76$ TeV”**, S. Chatrchyan *et al.* [CMS Collaboration], JHEP **1210**087 (2012)

251. **“Search for a light charged Higgs boson in top quark decays in pp collisions at $\sqrt{s} = 7$ TeV”**, S. Chatrchyan *et al.* [CMS Collaboration], JHEP **1207**143 (2012)

252. **“Search for new physics in events with same-sign dileptons and b-tagged jets in pp collisions at $\sqrt{s} = 7$ TeV”**, S. Chatrchyan *et al.* [CMS Collaboration], JHEP **1208**110 (2012)

253. **“Measurement of the pseudorapidity and centrality dependence of the transverse energy density in PbPb collisions at $\sqrt{s_{NN}} = 2.76$ TeV”**, S. Chatrchyan *et al.* [CMS Collaboration], Phys. Rev. Lett. **109**152303 (2012)

254. **“Measurement of the $Lambda_b$ cross section and the $\bar{\Lambda}(\ b^)$ to $Lambda_b$ ratio with $Lambda_b$ to J/Psi Λ decays in pp collisions at $\sqrt{s} = 7$ TeV”**, S. Chatrchyan *et al.* [CMS Collaboration], Phys. Lett. B **714**136 (2012)

255. **“Search for heavy long-lived charged particles in pp collisions at $\sqrt{s} = 7$ TeV”**, S. Chatrchyan *et al.* [CMS Collaboration], Phys. Lett. B **713**408 (2012)

256. **“Studies of jet quenching using isolated-photon+jet correlations in PbPb and pp collisions at $\sqrt{s_{NN}} = 2.76$ TeV”**, S. Chatrchyan *et al.* [CMS Collaboration], Phys. Lett. B **718**773 (2013)

257. **“Observation of a new Xi(b) baryon”**, S. Chatrchyan *et al.* [CMS Collaboration], Phys. Rev. Lett. **108**252002 (2012)

258. **“Search for anomalous production of multilepton events in pp collisions at $\sqrt{s} = 7$ TeV”**, S. Chatrchyan *et al.* [CMS Collaboration], JHEP **1206**169 (2012)

259. **“Search for leptonic decays of W ’ bosons in pp collisions at $\sqrt{s} = 7$ TeV”**, S. Chatrchyan *et al.* [CMS Collaboration], JHEP **1208**023 (2012)

260. **“Search for physics beyond the standard model in events with a Z bosonjetsand missing transverse energy in pp collisions at $\sqrt{s} = 7$ TeV”**, S. Chatrchyan *et al.* [CMS Collaboration], Phys. Lett. B **716**260 (2012)

261. **"ShapeTransverse Sizeand Charged Hadron Multiplicity of Jets in pp Collisions at 7 TeV"**, S. Chatrchyan *et al.* [CMS Collaboration], JHEP **1206**160 (2012)

262. **"Measurement of the mass difference between top and antitop quarks"**, S. Chatrchyan *et al.* [CMS Collaboration], JHEP **1206**109 (2012)

263. **"Search for Anomalous $t\bar{t}$ Production in the Highly-Boosted All-Hadronic Final State"**, S. Chatrchyan *et al.* [CMS Collaboration], JHEP **1209**029 (2012)[JHEP **1403**132 (2014)]

264. **"Azimuthal anisotropy of charged particles at high transverse momenta in PbPb collisions at $\sqrt{s_{NN}} = 2.76$ TeV"**, S. Chatrchyan *et al.* [CMS Collaboration], Phys. Rev. Lett. **109**022301 (2012)

265. **"Measurement of the Z/γ*+b-jet cross section in pp collisions at $\sqrt{s} = 7$ TeV"**, S. Chatrchyan *et al.* [CMS Collaboration], JHEP **1206**126 (2012)

266. **"Measurement of the elliptic anisotropy of charged particles produced in PbPb collisions at $\sqrt{s}_{NN}$=2.76 TeV"**, S. Chatrchyan *et al.* [CMS Collaboration], Phys. Rev. C **87**no. 1014902 (2013)

267. **"Measurement of the underlying event in the Drell-Yan process in proton-proton collisions at $\sqrt{s} = 7$ TeV"**, S. Chatrchyan *et al.* [CMS Collaboration], Eur. Phys. J. C **72**2080 (2012)

268. **"Search for heavy bottom-like quarks in 4.9 inverse femtobarns of *pp* collisions at $\sqrt{s} = 7$ TeV"**, S. Chatrchyan *et al.* [CMS Collaboration], JHEP **1205**123 (2012)

269. **"Search for Dark Matter and Large Extra Dimensions in pp Collisions Yielding a Photon and Missing Transverse Energy"**, S. Chatrchyan *et al.* [CMS Collaboration], Phys. Rev. Lett. **108**261803 (2012)

270. **"Ratios of dijet production cross sections as a function of the absolute difference in rapidity between jets in proton-proton collisions at $\sqrt{s} = 7$ TeV"**, S. Chatrchyan *et al.* [CMS Collaboration], Eur. Phys. J. C **72**2216 (2012)

271. **"Measurement of the top quark pair production cross section in *pp* collisions at $\sqrt{s} = 7$ TeV in dilepton final states containing a τ"**, S. Chatrchyan *et al.* [CMS Collaboration], Phys. Rev. D **85**112007 (2012)

272. **"Search for heavytop-like quark pair production in the dilepton final state in *pp* collisions at $\sqrt{s} = 7$ TeV"**, S. Chatrchyan *et al.* [CMS Collaboration], Phys. Lett. B **716**103 (2012)

273. **"Search for $B^0_s \to \mu^+\mu^-$ and $B^0 \to \mu^+\mu^-$ decays"**, S. Chatrchyan *et al.* [CMS Collaboration], JHEP **1204**033 (2012)

274. **"Measurement of the cross section for production of bb^{-} bar Xdecaying to muons in pp collisions at $\sqrt{s} = 7$ TeV"**, S. Chatrchyan *et al.* [CMS Collaboration], JHEP **1206**110 (2012)

275. **"Search for microscopic black holes in pp collisions at $\sqrt{s} = 7$ TeV"**, S. Chatrchyan *et al.* [CMS Collaboration], JHEP **1204**061 (2012)

276. **"Search for quark compositeness in dijet angular distributions from pp collisions at $\sqrt{s} = 7$ TeV"**, S. Chatrchyan *et al.* [CMS Collaboration], JHEP **1205**055 (2012)

277. **"Jet momentum dependence of jet quenching in PbPb collisions at $\sqrt{s_{NN}} = 2.76$ TeV"**, S. Chatrchyan *et al.* [CMS Collaboration], Phys. Lett. B **712**176 (2012)

278. **"Inclusive b-jet production in pp collisions at $\sqrt{s} = 7$ TeV"**, S. Chatrchyan *et al.* [CMS Collaboration], JHEP **1204**084 (2012)

279. **"Search for the standard model Higgs boson decaying to bottom quarks in pp collisions at $\sqrt{s} = 7$ TeV"**, S. Chatrchyan *et al.* [CMS Collaboration], Phys. Lett. B **710**284 (2012)

280. **"Search for neutral Higgs bosons decaying to τ pairs in pp collisions at $\sqrt{s} = 7$ TeV"**, S. Chatrchyan *et al.* [CMS Collaboration], Phys. Lett. B **713**68 (2012)

281. **"Search for large extra dimensions in dimuon and dielectron events in pp collisions at $\sqrt{s} = 7$ TeV"**, S. Chatrchyan *et al.* [CMS Collaboration], Phys. Lett. B **711**15 (2012)

282. **"Search for the standard model Higgs boson in the H to ZZ to 2 $\ell 2\nu$ channel in pp collisions at $\sqrt{s} = 7$ TeV"**, S. Chatrchyan *et al.* [CMS Collaboration], JHEP **1203**040 (2012)

283. **"Search for the standard model Higgs boson in the H to ZZ to $\ell\ell\tau\tau$ decay channel in pp collisions at $\sqrt{s} = 7$ TeV"**, S. Chatrchyan *et al.* [CMS Collaboration], JHEP **1203**081 (2012)

284. **"Study of high-pT charged particle suppression in PbPb compared to pp collisions at $\sqrt{s_{NN}} = 2.76$ TeV"**, S. Chatrchyan *et al.* [CMS Collaboration], Eur. Phys. J. C **72**1945 (2012)

285. **"Search for the standard model Higgs boson in the decay channel H to ZZ to 4 leptons in pp collisions at $\sqrt{s} = 7$ TeV"**, S. Chatrchyan *et al.* [CMS Collaboration], Phys. Rev. Lett. **108**111804 (2012)

286. **"Search for the standard model Higgs boson decaying to a W pair in the fully leptonic final state in pp collisions at $\sqrt{s} = 7$ TeV"**, S. Chatrchyan *et al.* [CMS Collaboration], Phys. Lett. B **710**91 (2012)

287. **"Combined results of searches for the standard model Higgs boson in** pp **collisions at** $\sqrt{s} = 7$ **TeV"**, S. Chatrchyan *et al.* [CMS Collaboration], Phys. Lett. B **710**26 (2012)

288. **"Search for the standard model Higgs boson decaying into two photons in** pp **collisions at** $\sqrt{s} = 7$ **TeV"**, S. Chatrchyan *et al.* [CMS Collaboration], Phys. Lett. B **710**403 (2012)

289. **"Search for a Higgs boson in the decay channel** H **to ZZ(*) to** q **qbar** ℓ^- **l+ in** pp **collisions at** $\sqrt{s} = 7$ **TeV"**, S. Chatrchyan *et al.* [CMS Collaboration], JHEP **1204**036 (2012)

290. **"Measurement of the inclusive production cross sections for forward jets and for dijet events with one forward and one central jet in** pp **collisions at** $\sqrt{s} = 7$ **TeV"**, S. Chatrchyan *et al.* [CMS Collaboration], JHEP **1206**036 (2012)

291. **"Suppression of non-prompt** J/ψ**prompt** J/ψ**and Y(1S) in PbPb collisions at** $\sqrt{s_{NN}} = 2.76$ **TeV"**, S. Chatrchyan *et al.* [CMS Collaboration], JHEP **1205**063 (2012)

292. **"Centrality dependence of dihadron correlations and azimuthal anisotropy harmonics in PbPb collisions at** $\sqrt{s_{NN}} = 2.76$ **TeV"**, S. Chatrchyan *et al.* [CMS Collaboration], Eur. Phys. J. C **72**2012 (2012)

293. **"Measurement of isolated photon production in** pp **and PbPb collisions at** $\sqrt{s_{NN}} = 2.76$ **TeV"**, S. Chatrchyan *et al.* [CMS Collaboration], Phys. Lett. B **710**256 (2012)

294. **"Measurement of the charge asymmetry in top-quark pair production in proton-proton collisions at** $\sqrt{s} = 7$ **TeV"**, S. Chatrchyan *et al.* [CMS Collaboration], Phys. Lett. B **709**28 (2012)

295. **"Search for signatures of extra dimensions in the diphoton mass spectrum at the Large Hadron Collider"**, S. Chatrchyan *et al.* [CMS Collaboration], Phys. Rev. Lett. **108**111801 (2012)

296. **"Exclusive photon-photon production of muon pairs in proton-proton collisions at** $\sqrt{s} = 7$ **TeV"**, S. Chatrchyan *et al.* [CMS Collaboration], JHEP **1201**052 (2012)

297. **"**J/ψ **and** ψ_{2S} **production in** pp **collisions at** $\sqrt{s} = 7$ **TeV"**, S. Chatrchyan *et al.* [CMS Collaboration], JHEP **1202**011 (2012)

298. **"Measurement of the Production Cross Section for Pairs of Isolated Photons in** pp **collisions at** $\sqrt{s} = 7$ **TeV"**, S. Chatrchyan *et al.* [CMS Collaboration], JHEP **1201**133 (2012)

299. **“Measurement of the Rapidity and Transverse Momentum Distributions of Z Bosons in pp Collisions at $\sqrt{s} = 7$ TeV”**, S. Chatrchyan *et al.* [CMS Collaboration], Phys. Rev. D **85**032002 (2012)

300. **“Jet Production Rates in Association with W and Z Bosons in pp Collisions at $\sqrt{s} = 7$ TeV”**, S. Chatrchyan *et al.* [CMS Collaboration], JHEP **1201**010 (2012)

301. **“Measurement of the weak mixing angle with the Drell-Yan process in proton-proton collisions at the LHC”**, S. Chatrchyan *et al.* [CMS Collaboration], Phys. Rev. D **84**112002 (2011)

302. **“Forward Energy FlowCentral Charged-Particle Multiplicitiesand Pseudorapidity Gaps in W and Z Boson Events from pp Collisions at $\sqrt{s} = 7$ TeV”**, S. Chatrchyan *et al.* [CMS Collaboration], Eur. Phys. J. C **72**1839 (2012)

303. **“Performance of tau-lepton reconstruction and identification in CMS”**, S. Chatrchyan *et al.* [CMS Collaboration], JINST **7**P01001 (2012)

304. **“Search for a Vector-like Quark with Charge 2/3 in $t + Z$ Events from pp Collisions at $\sqrt{s} = 7$ TeV”**, S. Chatrchyan *et al.* [CMS Collaboration], Phys. Rev. Lett. **107**271802 (2011)

305. **“Search for Supersymmetry at the LHC in Events with Jets and Missing Transverse Energy”**, S. Chatrchyan *et al.* [CMS Collaboration], Phys. Rev. Lett. **107**221804 (2011)

306. **“Measurement of the Differential Cross Section for Isolated Prompt Photon Production in pp Collisions at 7 TeV”**, S. Chatrchyan *et al.* [CMS Collaboration], Phys. Rev. D **84**052011 (2011)

307. **“Measurement of the Drell-Yan Cross Section in pp Collisions at $\sqrt{s} = 7$ TeV”**, S. Chatrchyan *et al.* [CMS Collaboration], JHEP **1110**007 (2011)

308. **“Search for B(s) and B to dimuon decays in pp collisions at 7 TeV”**, S. Chatrchyan *et al.* [CMS Collaboration], Phys. Rev. Lett. **107**191802 (2011)

309. **“Search for Resonances in the Dijet Mass Spectrum from 7 TeV pp Collisions at CMS”**, S. Chatrchyan *et al.* [CMS Collaboration], Phys. Lett. B **704**123 (2011)

310. **“Dependence on pseudorapidity and centrality of charged hadron production in PbPb collisions at a nucleon-nucleon centre-of-mass energy of 2.76 TeV”**, S. Chatrchyan *et al.* [CMS Collaboration], JHEP **1108**141 (2011)

311. **“Determination of Jet Energy Calibration and Transverse Momentum Resolution in CMS”**, S. Chatrchyan *et al.* [CMS Collaboration], JINST **6**P11002 (2011)